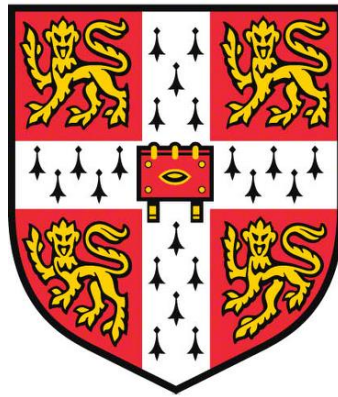


**Solution-Processed ZnO Nanoparticles for Optically
Addressed Spatial Light Modulators and Other
Applications**



*This thesis is submitted for the degree of
Doctor of Philosophy
at the University of Cambridge*

Xin Chang
Girton College
Department of Engineering
23 Sep 2019

Declaration

This dissertation is the result of my own work and includes nothing which is the outcome of work done in collaboration except as declared in the Preface and specified in the text. It is not substantially the same as any that I have submitted, or, is being concurrently submitted for a degree or diploma or other qualification at the University of Cambridge or any other University or similar institution except as declared in the Preface and specified in the text. I further state that no substantial part of my dissertation has already been submitted, or, is being concurrently submitted for any such degree, diploma or other qualification at the University of Cambridge or any other University or similar institution except as declared in the Preface and specified in the text.

This dissertation, including appendices, bibliography, tables and equations, does not exceed the prescribed word limit of 65,000 and figure limit of 150.

Xin Chang

September 2019

Author name: Xin Chang

Title: Solution-Processed ZnO Nanoparticles for Optically Addressed Spatial Light Modulators and Other Applications

Abstract:

Solution-processable materials are becoming increasingly attractive due to their use in low cost, high throughput and relatively easy fabrications. In addition, the possibility of high-resolution patterning makes solution-based materials particularly suitable for integrated applications. The material that was investigated in this work is zinc oxide nanoparticles (ZnO NPs) dispersion, motivated by the highest resolution on record of optically addressed spatial light modulators (OASLMs) using solution-based ZnO NP as photoactive material. ZnO is a popular type of semiconductor compound from II-VI group and ZnO NPs are the nanocrystalline form of ZnO, which exhibit many unique and superior properties such as direct and wide bandgap, large surface-to-volume ratio, antibacterial and eco-friendly nature. Therefore, the investigation of ZnO NPs in terms of their physical properties, post processing effect, patterning techniques, and applications are of great significance.

In this work, thin films made from ZnO NP dispersion in ethanol was characterized in detail including their structural, electrical, dielectric and optical properties. The post-processing effect such as thermal annealing and oxygen plasma treatment was also investigated. Then ZnO NP-based OASLM was researched by simulation and device characterization regarding electrical and optical properties. More importantly, the optimization of ZnO NP-based OASLMs was conducted in terms of diffraction efficiency and response speed, which are two key factors limiting the development of ZnO NP-based OASLMs. The diffraction efficiency was improved by pinpointing the optimum parameters of the driving signal such as waveform, amplitude and frequency. And the response time was reduced by several methods such as thermal annealing, introducing an interfacial layer and replacing the photoconductive ZnO NP layer with ZnO NP-based photodiode structure. The sensing of oxygen partial pressure in air by ZnO NP thin film was also observed and studied. Moreover, device miniaturization was achieved by the mould-guided drying technique, indicating a promising future for integrated applications. This patterning technique was also used for another type of solution-based material: PEDOT:PSS. And PEDOT:PSS-based organic electrochemical transistors (OECTs) with nanoscale channel length and channel width were realized by including a lift-off process, which demonstrated a great high-frequency response.

Acknowledgements

I would love to express my sincere gratitude to my supervisor Prof. Daping Chu, who has always been a knowledgeable, visionary, generous and kind man and has provided me with great support. Prof. Chu can always give me valuable advices on academic questions and uncertainties over career whenever I was in doubt. He is also diligent and meticulous, which is truly inspiring to me and to all the members in the CPDS group. Moreover, Prof. Chu is also supportive to my non-academic life and helps me to steer on a right track.

I also want to thank all the members within CPDS group, who have always been friendly and helpful. In particular, I want to give special thanks to Dr Shunpu Li and Dr Jin Li, who have provided great suggestions for my research and shared numerous research experience with me. In addition, I would like to thank Dr Pawan Shrestha and Dr Kasia Surowiecka for their help in practical and experimental difficulties. I would also like to appreciate Ms Denisa Demko, who has been very helpful in administrative issues.

Special thanks should be given to my parents, who have been loving me and supporting me in every aspect. Moreover, I want to thank my friends in Cambridge, who have accompanied me all the way through my PhD life.

Table of Contents

Declaration.....	1
Abstract.....	2
Acknowledgements.....	3
Table of Contents	4
List of Figures.....	7
List of Publications.....	12
Chapter 1 Introduction.....	13
1.1 Fundamentals of ZnO and ZnO Nanoparticles	13
1.1.1 Basic properties of ZnO.....	14
1.1.2 Basic properties of ZnO NPs	15
1.2 Solution-Based Fabrication Processes for Thin Films and Features	17
1.2.1 Spin coating	17
1.2.2 Photopatterning.....	18
1.2.3 Printing	18
1.2.4 Mould-guided drying.....	19
1.3 Introduction to Optically Addressed Spatial Light Modulators (OASLMs)	20
1.3.1 Working principles	21
1.3.2 Fundamentals of liquid crystals	22
1.3.3 Challenges	28
1.3.4 Current progress	30
1.4 Sensor for Oxygen Partial Pressure in Air.....	30
1.4.1 Semiconductor-based oxygen partial pressure sensor	30
1.4.2 ZnO-based oxygen partial pressure sensor	31
Chapter 2 Preparation and Characterization of Solution-Processed ZnO NP Thin Films	32
2.1 Sample Preparation.....	32
2.2 Characterization of ZnO NP Thin Films	34
2.2.1 Particle size.....	34
2.2.2 Composition	36
2.2.3 Lattice structure	38
2.2.4 Electrical conduction mechanism.....	38

2.2.5 Field effect mobility	40
2.2.6 Trap activation energy.....	42
2.2.7 Dielectric properties	44
2.2.8 Optical absorption	47
2.2.9 UV response	49
2.3 Annealing Effect on ZnO NP Thin Films	50
2.3.1 Lattice structure.....	50
2.3.2 Electrical properties.....	51
2.3.3 Dielectric properties	52
2.3.4 Optical properties	54
2.4 Oxygen Plasma Effect on ZnO NP Thin Films	56
Chapter 3 The Characterization and Optimization of ZnO NPs-based OASLMs	58
3.1 Simulations of LCs in OASLMs	58
3.1.1 Electric fringing field in LCs.....	59
3.1.2 Effect of driving voltage and thickness	62
3.1.3 Effect of elastic constants and dielectric constants	64
3.2.4 Other effects	67
3.2 Simulations of ZnO NP Thin Films in OASLMs.....	69
3.3 Fabrication Process of OASLMs.....	70
3.4 Characterization of OASLMs.....	72
3.4.1 Dielectric properties LCs	72
3.4.2 Dielectric properties of OASLMs	75
3.4.3 Optical properties of OASLMs	76
3.5 The Optimization of ZnO NPs-Based OASLMs.....	78
3.5.1 Improving the diffraction efficiency	78
3.5.2 Improving the response time	84
3.5.3 Heterojunction Photodiode in OASLMs	86
Chapter 4 ZnO NPs-based Sensor for Oxygen Partial Pressure in Air	94
4.1 Oxygen Partial Pressure Effect	94
4.2 Sensor Fabrication and Characterization.....	95
4.3 Miniaturized Oxygen Sensor.....	97
Chapter 5 High-Resolution Patterning of PEDOT:PSS and PEDOT:PSS-based Organic Electrochemical Transistors (OECTs).....	102
5.1 Electrical Properties of PEDOT:PSS Thin Film	103
5.2 The Patterning of PEDOT:PSS Lines	105
5.2.1 The patterning process	105

5.2.2 Optical and electrical anisotropy of the patterned PEDOT:PSS lines	108
5.3 Organic Electrochemical Transistors (OECTs) Based on the Patterned PEDOT:PSS Lines...	109
5.4 Sub-Micron OECTs.....	111
5.4.1 Transistor characteristics	112
5.4.2 Frequency response	113
5.4.3. Effect of electrode area.....	115
Chapter 6 Conclusions and Future Work.....	117
6.1 Conclusions	117
6.2 Future Work.....	118
References	120

List of Figures

1. Figure 1.1 Lattice structure of wurtzite ZnO.
2. Figure 1.2 Illustration of mould-guided drying technique.
3. Figure 1.3 Structure of (a) LCOS. and (b) OASLM.
4. Figure 1.4 Working principles of OASLMs.
5. Figure 1.5 Molecular arrangement of (a) nematic LCs. (b) cholesteric LCs. (c) smectic A LCs. (d) smectic C LCs and (e) smectic B LCs.
6. Figure 1.6 The orientation of nematic LCs molecules.
7. Figure 1.7 Three types of deformation of LCs: (a) splay, (b) twist, and (c) bend.
8. Figure 1.8 Anisotropy of LCs when wave vector (\vec{k}) and director (\vec{n}) are (a) aligned and (b) not aligned.
9. Figure 1.9 Molecular orientation of LCs (a) without electric field and (b) under DC voltage.
10. Figure 2.1 Surface of ZnO NPs thin films prepared by different ZnO NPs concentrations (a) 4.5mg/ml. (b) 125mg/ml. (c) 250mg/ml. (d) 1150mg/ml. (e) The histogram and distribution of film height. (f) Comparison of height distribution between films of 4.5mg/ml and 1150mg/ml. (g) Film thickness measured by surface profiler. (h) Film thicknesses of different ZnO NPs concentrations.
11. Figure 2.2 (a) SEM image of ZnO NPs. (b) Size distribution of ZnO NPs by DLS. (c) Surface profile measured by AFM. (d) 3D contour of ZnO NPs surface, generated by AFM measurement.
12. Figure 2.3 (a) EDX spectrum of ZnO NPs. (b) Atomic ratio of composing elements
13. Figure 2.4 (a) I-V characteristics of ZnO NPs with and without oxygen plasma treatment. (b) The conductance of ZnO NPs tracked after plasma treatment.
14. Figure 2.5 XRD pattern of ZnO NPs
15. Figure 2.6 (a) Schematic structure of ZnO NPs sample. (b) The I-V characteristics of ZnO NPs. (c) The I-V characteristics of ZnO NPs at high DC voltage. (d) The slope of $\text{Log}(I) \sim V$ at different temperature.
16. Figure 2.7 (a) The image of ZnO NPs transistor under optical microscope. (b) The transfer characteristics of ZnO NPs transistor. (c) The field effect mobility under different measuring temperatures.
17. Figure 2.8 (a) The I-V characteristics of ZnO NPs under different measuring temperatures. (b) The Arrhenius plot and trap activation energy. The (c) I-V characteristics and (d) Arrhenius plot of ZnO NPs annealed for 5h.
18. Figure 2.9 (a) The grain-boundary model and double-well potential model of ZnO NPs. The (b) Bode plot. (c) Nyquist plot. of ZnO NPs. (d) Phase under different DC bias voltages from 1V

- to 5V. (e) RC time constants of grain and boundary under different DC bias voltages. (f) Boundary resistance and capacitance under different DC bias voltages.
19. Figure 2.10 Electrical hysteresis of ZnO NPs.
 20. Figure 2.11 (a) UV-Vis spectroscopy of ZnO NPs. (b) The Tauc plot and energy bandgap.
 21. Figure 2.12 (a) UV response of ZnO NPs. (b) External quantum efficiency (EQE) of ZnO NPs.
 22. Figure 2.13 XRD pattern of ZnO NPs annealed at 200°C and 500°C.
 23. Figure 2.14 Arrhenius plot of ZnO NPs annealed at different temperatures for (a) 3h and (b) 5h in air. Annealing effect on (d) Transfer function and (e) Charge carrier mobility.
 24. Figure 2.15 (a) RC time constant and (b) Boundary resistance of ZnO NPs annealed at different temperatures. (c) Electrical hysteresis for ZnO NPs. (d) Hysteresis ratio (A_2/A_1) against different temperatures.
 25. Figure 2.16 The (a) On and off current, (b) On/off current ratio, (c) Fall time, (d) Energy bandgap, (e) Photocurrent against UV power density and (f) External quantum efficiency of ZnO NPs annealed at different temperatures.
 26. Figure 2.17 The (a) I-V characteristics and (b) Trap activation energy of ZnO NPs annealed at 600°C with and without oxygen plasma treatment. UV response of ZnO NPs annealed at (c) 400°C and (d) 600°C.
 27. Figure 3.1 The typical structure of OASLMs.
 28. Figure 3.2 The simulated results for (a) Director (nail) and phase retardation profile (red line), (b) Electric force (arrow) and electric potential (colormap) of the cross-section. (c) Force analysis for LCs in the middle.
 29. Figure 3.3 (a) Model of LCs cell. (b) 3D model in LCD Master.
 30. Figure 3.4 The (a) magnitude and (b) angle of electric force in LCs.
 31. Figure 3.5 Electric potential distribution in LCs.
 32. Figure 3.6 (a) The phase retardation profile under different driving voltages. (b) The distortion at the axis of symmetry under different voltages.
 33. Figure 3.7 (a) Phase retardation profile of various LCs thickness. (b) The modulation depth and phase width at different LCs thickness.
 34. Figure 3.8 (a) Phase retardation profile for different k_1 values. (b) The phase width (resolution) for different k_1 values.
 35. Figure 3.9 (a) Phase retardation profile for different k_3 values. (b) Phase width for different k_3 values.
 36. Figure 3.10 The torque of LCs under electric field.
 37. Figure 3.11 Phase retardation profile of different (a) $\epsilon_{//}$ and (b) ϵ_{\perp} values. Phase width (resolution) of different (c) $\epsilon_{//}$ and (d) ϵ_{\perp} values.
 38. Figure 3.12 (a) The phase retardation profile for different bottom electrodes. (b) The phase width at different electrode lengths.

39. Figure 3.13 (a) The potential distribution and electric force in LCs with two ZnO NPs layers. (b) The comparison in phase retardation profile for single and double ZnO NPs layers.
40. Figure 3.14 (a) Simulated electric field in ZnO NPs layer. (b) Comparison of electric field in X direction at the bottom for different light intensity profiles.
41. Figure 3.15 (a) Dispense the glue on two sides. (b) Offset for cabling.
42. Figure 3.16 The (a) Bode plot and (b) Nyquist plot of the LCs cell. The simulated (c) Resistance and (d) Capacitance of LCs and alignment. The (e) RC time constants of LCs and alignment under different DC voltages. (f) The overall impedance of the cell under different DC voltages.
43. Figure 3.17 (a) RC time constants for E7 LCs. (b) Comparison between E7 and 8CB LCs under different DC voltages.
44. Figure 3.18 The (a) Bode plot and (b) RC time constants of OASLM. The (c) Bode plot and (d) overall resistance / capacitance of OASLM under UV. (e) The RC time constant of OASLM under UV.
45. Figure 3.19 The optical setup for OASLM characterization.
46. Figure 3.20 (a) Recorded signal from photodetector. (b) The decrease of signal intensity after the write light was turned off.
47. Figure 3.21 First-order diffraction signal when the driving voltage has an amplitude of (a) $V_P=2V$ and (b) $V_P=1.2V$. (c) The relationship between diffraction efficiency and phase retardation. (d) The intensity of V_{peak} and V_{side} at different voltage amplitudes.
48. Figure 3.22 First-order diffraction signal when the driving voltage has an amplitude of (a) $V_P=2V$ and (b) $V_{PP}=1.4V$. (c) The intensity of V_{peak} and V_{side} at different voltage amplitudes. (d) Comparison of first-order diffraction signal between sinusoidal and triangular driving signal under the same driving frequency (0.5Hz).
49. Figure 3.23 (a) The first-order diffraction signal driven by a square signal. (b) The height of the diffracted signal at different voltage amplitudes. (c) The imaginary impedance of an OASLM cell measured with positive and negative DC bias voltages. (d) The effect of driving frequency on diffraction efficiency.
50. Figure 3.24 The first-order diffraction pattern generated by a sinusoidal wave with (a) $V_{peak}=1.6V$, $f=0.5Hz$ and (b) $V_{peak}=2.0V$, $f=0.5Hz$. (c) The height of the diffracted signal at different voltage amplitudes. (d) The imaginary impedance of OASLM with and without SiO_2 layer.
51. Figure 3.25 The signal falling after write light is off. (a) ZnO NPs were annealed in air at $400^\circ C$ for 3h. (b) A layer of SiO_2 was introduced between ZnO NPs and LCs.
52. Figure 3.26 The annealing effect on glass substrate.
53. Figure 3.27 The molecular structure of PEDOT and PSS ionomer.
54. Figure 3.28 The structure of ZnO NPs-PEDOT:PSS heterojunction and the energy band diagram.

55. Figure 3.29 (a) The I-V characteristics of ZnO NPs and PEDOT:PSS heterojunction. (b) The comparison in I-V characteristics between heterojunction and ZnO NPs.
56. The imaginary impedance (black) and $1/C2$ (red) at different reversed bias voltages.
57. Figure 3.31 The real and imaginary impedance of heterojunction at $-1V \sim 1V$.
58. Figure 3.32 The (a) Bode plot and (b) Nyquist plot of the heterojunction under forward and reversed bias. The Nyquist plot under several (c) Forward bias and (d) Reversed bias voltages. (e) The intersection frequency under increasing forward bias voltages. (f) Pseudo-inductive behaviour.
59. Figure 3.33 (a) The photo response of ZnO NPs and ZnO NPs - PEDOT:PSS heterojunction. (b) The photo conductance of ZnO NPs - PEDOT:PSS heterojunction at different bias conditions and light intensities. (c) The signal intensity of heterojunction-based OASLM. (d) The falling time of heterojunction-based OASLM after write light was off.
60. Figure 4.1 Oxygen adsorption and desorption on ZnO NPs.
61. Figure 4.2 (a) I-V characteristics of ZnO NPs in vacuum. (b) Field effect of ZnO NPs under different measuring conditions.
62. Figure 4.3 The structure of ZnO NPs-based oxygen sensor.
63. Figure 4.4 (a) The conductance of ZnO NPs under different air pressure. (b) The electrical response to the erasing heat.
64. Figure 4.5 The ZnO NPs lines fabricated by photolithography, observed by (a) Optical microscope and (b) SEM.
65. Figure 4.6 (a) ZnO NPs lines by direct stamping. (b) The fabrication of ZnO NPs lines by PS 'spacer'. (c) Patterning PS lines on top of ZnO NPs film. (d) SEM image of ZnO NPs lines. (e) The oxygen sensing performance of ZnO NPs lines. (f) The minimal line width achieved.
66. Figure 4.7 (a) In_2O_3 lines under optical microscope. The (b) Transfer function and (c) Output function of In_2O_3 lines transistor.
67. Figure 5.1 (a) The planar structure of Al-PEDOT:PSS-Al sample. (b) I-V characteristics of PEDOT:PSS. (c) Low-temperature conductance of PEDOT:PSS.
68. Figure 5.2 The (a) Bode plot and (b) Nyquist plot of PEDOT:PSS.
69. Figure 5.3 (a) The PEDOT:PSS thin film formed on the SiO_2 substrate. (b) A gap between PEDOT:PSS and Al was created by photolithography.
70. Figure 5.4 The (a) Cross-section profile and (b) SEM image of a single PEDOT:PSS line. (c) PEDOT:PSS lines and (d) SEM image. (e) PEDOT:PSS grid and (f) SEM image.
71. Figure 5.5 (a) Optical anisotropy. (b) Electrical conductivity of PEDOT:PSS thin film and lines.
72. Figure 5.6 Structure of OECT.
73. Figure 5.7 The (a) Transfer function and (b) Output function of the OECT based on the patterned PEDOT:PSS lines.

74. Figure 5.8 (a) The fabrication process of nanostructured OEECTs. (b) The nanoscale channel width and channel length by SEM.
75. Figure 5.9 The (a) Transfer function and (b) Output function of the nanostructured OEECT.
76. Figure 5.10 The frequency response of (a) Single square signal, $f=1\text{kHz}$. (b) Two sine signals, $f_1=500\text{Hz}$ (600mv), $f_2=100\text{Hz}$ (300mv). (c) Two sine signals, $f_1=500\text{Hz}$ (600mv), $f_2=100\text{Hz}$ (200mv). (d) Two sine signals, $f_1=500\text{Hz}$ (600mv), $f_2=100\text{Hz}$ (100mv). (e) A small phase change ($<0.01 \pi$)
77. Figure 5.11 (a) The transfer function of OEECT with different electrode area. (b) and (c) The influence of electrode area and gate voltages.

List of Publications

1. Chang, X., Li, S. and Chu, D. (2020). 'Sensing of Oxygen Partial Pressure in Air with ZnO Nanoparticles'. *Sensors*, 20(2), 562; <https://doi.org/10.3390/s20020562>.
2. Chang, X., Shrestha, P. and Chu, D. (2020). 'Reduction of Switching Time in ZnO Nanoparticle-based Reflective OASLM for Holographic Displays', *Proceedings of SPIE*. (under review)
3. Shrestha, P.K.*, Chang, X.*, Pryne, M., Li, J., Rughoobur, G., Li, K., Surowiecka, K. and Chu, D. 'A large-size updatable optically addressed spatial light modulator (OASLM) based on ZnO nanoparticles for large-area holographic 3D displays', *OSA Continuum*. (*co-first author, under review)
4. Li, J.*, Chang, X.*, Li, S., Shrestha, P.K., Tan, E., and Chu, D. 'High-resolution electro-chemical transistors defined by mould-guided drying of PEDOT:PSS liquid suspension', *ACS Applied Materials & Interfaces*. (*co-first author, under review)
5. Zhang, C., Tian, B., Cheng, T., Ding, B., Fan, L., Chang, X., and Hochgreb, S. 'Floating catalyst carbon nanotube synthesis assisted by premixed hydrogen/air flames', *CARBON*. (under review)
6. Chang, X., Li, J., Shrestha, P. and Chu, D. 'Fast-switching optically addressed spatial light modulator (OASLM) based on ZnO Nanoparticle / PEDOT:PSS heterojunction'. (in submission)

Chapter 1 Introduction

Solution-processable materials have been attracting more and more attention in recent years due to their advantages in low cost, large-scale production, tailorable properties, applicability for various post-processing techniques, compatibility with flexible substrates and low fabrication requirements [1], [2]. Furthermore, solution-based materials can also provide superior performance such as the highest resolution of OASLM on record (825 lp/mm) using colloidal ZnO NP dispersion [3], so they have become regarded as the next generation materials for a wide range of applications. In addition, the demand for transparent semiconductor materials with a wide bandgap is growing dramatically since applications such as wearable electronics, transparent displays, artificial organs and radio-frequency identification (RFID) are becoming unprecedentedly significant during the last decade [4], [5].

Solution-processed zinc oxide nanoparticles (ZnO NPs) in ethanol is one of the main research topics in this work. ZnO is a popular semiconductive material with a direct and wide bandgap, high thermal conductivity, optical transparency, high electron mobility and tuned conductivity [6]. Recently, an increasing amount of research has been conducted into ZnO NPs since ZnO NPs have a large surface-to-volume ratio and are defect-rich, behaving differently from other forms of ZnO.

In this chapter, fundamental properties of ZnO and ZnO NPs are discussed, followed by the introduction to the fabrication and patterning techniques for solution-processable materials. Furthermore, applications of ZnO NPs such as optically addressed spatial light modulators (OASLMs) and oxygen partial pressure sensors are introduced.

1.1 Fundamentals of ZnO and ZnO Nanoparticles

ZnO has been widely investigated over the past several years due to its semiconductive nature, low toxicity and availability in large bulk single crystals [6]. A broad range of potential applications of ZnO have been widely used. For instance, ZnO is a promising semiconductor material for electronic and photonic applications (UV sensors [7], LEDs [8], solar cells [9], photocatalyst [10] and lasers [11]) due to its wide bandgap (3.37eV) and high exciton binding energy (60meV) at room temperature [12].

ZnO NPs normally have a particle diameter between 1nm~100nm, and they generally have a large surface-to-volume ratio, enhanced surface reactivity [13] and other size-dependent

features. Similar to ZnO, NPs of ZnO are also used in miscellaneous products such as ceramics and plastics etc [14]. In addition, the antibacterial properties of ZnO NPs make them particularly appealing in pharmaceutical and food industries [13], [15]. Although ZnO NPs exhibit antimicrobial and antibacterial activities, they are reported to be non-toxic to human cells [16], so they are also suitable for cosmetic products such as sunscreens and dental fillings.

1.1.1 Basic properties of ZnO

ZnO is a group II-VI compound with a natural n-type conductivity due to its intrinsic defects such as oxygen vacancies and zinc interstitials. There are normally three types of lattice structures for ZnO: wurtzite, zinc blende and rock-salt. Wurtzite structure is the most stable structure at room temperature because of the ionic behaviour of Zn-O bond [17], which comes from the large difference in electronegativity between Zn and O. In contrast, ZnO of zinc blende structure is more covalent in Zn-O bond. Wurtzite ZnO has a hexagonal lattice, indicating that every Zn atom is surrounded by 4 O atoms and vice versa, as is shown in figure 1.1 below. The lattice parameter a and c of wurtzite ZnO are about 3.24 Å and 5.20 Å respectively, having a ratio (c/a) of 1.633 [18].

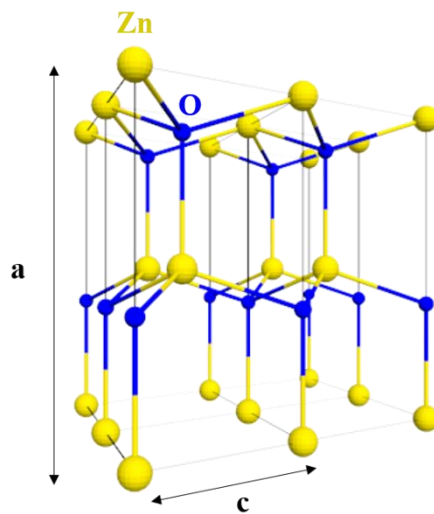


Figure 1.1 Lattice structure of wurtzite ZnO.

In general, ZnO crystal has a wide and direct bandgap of 3.37eV, which could be varied by adding Mg (increased bandgap) or Cd element (decreased bandgap) [6]. The electron mobility of bulk crystal ZnO has been reported to be between 205 and 298 $\text{cm}^2\text{v}^{-1}\text{s}^{-1}$ at low electric field [19]. In contrast, thin-film ZnO has a relatively lower electron mobility from 120 to 155 $\text{cm}^2\text{v}^{-1}\text{s}^{-1}$ in a low electric field [20], [21]. Charge scattering is the dominant factor limiting electrical

mobility in a low electric field and the scattering results from the ionized impurities and lattice defects.

Similar to most semiconductor materials, the properties of ZnO are strongly dependent on trap states and defects. For instance, the n-type conductivity of ZnO was attributed to oxygen vacancies (V_O) [22], [23] before this theory was overturned by the existence of hydrogen species because V_O is a deep donor (1eV below conduction band) and cannot affect the density of equilibrium charge [24], [25]. The optical absorption is also influenced by V_O . It has been reported that the absorption range broadens as the concentration of V_O increases [26]. It was also found that the absorption edge shifts towards a longer wavelength as the concentration of V_O increases, which implies that the band gap decreases (from 3.2eV to 2.5eV for ZnO and $ZnO_{0.952}$) [22]. In terms of photoluminescence (PL), two emission peaks are normally observed in ZnO. Near-UV peak (3.3eV) is generally considered to be associated with band-to-band recombination of electron-hole pairs from conduction band to valence band. The other peak (2.2eV) lies in the visible range (green) and the reason is still controversial. Some researchers claimed that it is due to the electrons trapped in deep V_O states (1eV below conduction band) [27], [28], [29]. However, this is challenged by many researchers. Other mechanisms for green emission were also proposed such as zinc interstitials, Cu impurities, donor-acceptor transition and surface defects [30], [31].

ZnO also has other interesting features such as the large piezoelectric constant, which enable ZnO-based transducers and actuators. High thermal conductivity of ZnO also makes it valuable as an additive for heat dissipation [6]. Moreover, the radiation hardness of ZnO was reported to be high, which makes it suitable for aerospace applicants [32].

1.1.2 Basic properties of ZnO NPs

ZnO NPs are the nanocrystalline form of ZnO and they tend to show increasingly dominant quantum effect and surface effect as the size decreases, such as enlarged bandgap and enhanced chemical reactivity [15]. The surface reactivity of ZnO NPs has received considerable research interest from pharmaceutical and biological industries. In addition, ZnO NPs are rich in defects and the surface defects have a strong influence on their properties due to the larger surface-to-volume ratio of ZnO NPs compared to bulk ZnO. Many types of defects exist in ZnO NPs such as oxygen vacancies (V_O), zinc vacancies (V_{Zn}), zinc interstitials (Zn_i), and dangling bonds. V_O and Zn_i are the most common defects. Although enormous efforts have been put into investigating the properties ZnO NPs, there are still several unresolved challenges such as the

origin of green emission (typically around 520nm) in photoluminescence (PL) and p-type doping [33], [34]. Among all the interesting features of ZnO NPs, two properties are of particular interest to this work: UV sensitivity and oxygen sensitivity.

- **UV sensitivity**

ZnO NPs are suitable for UV photodetectors due to the high UV absorption and high responsivity to UV light, while ZnO NPs have little sensitivity for visible light. UV illumination results in an increase in electrical conductivity, which is generally attributed to the desorption of oxygen molecules on ZnO NPs [7], [35]. Oxygen molecules tend to be adsorbed on the surface of ZnO NPs by capturing free electrons. As a result, ZnO NPs are surrounded by highly resistive depletion layers (oxygen ions). Free electron-hole pairs are generated upon UV radiation, releasing electrons from oxygen ions and increasing the electrical conductivity.

On the other side, the large surface-to-volume ratio of ZnO NPs enhances this process compared to bulk ZnO and makes ZnO NPs particularly suitable for UV detectors. It has been reported that UV photodetectors, that were based on the solution-processed ZnO NPs, exhibited high dark resistance ($>1\text{T}\Omega$) and fast response speed (characteristic rise time and fall time of $<0.1\text{s}$ and $\sim 1\text{s}$ respectively) [7]. Other researchers also achieved a current on/off ratio of 10^6 using ZnO NPs dispersions [35].

- **Oxygen sensitivity**

Similar to UV absorption, the oxygen sensing capability of ZnO NPs is generally ascribed to the adsorption and desorption of oxygen molecules on ZnO NPs by capturing or releasing electrons. Large surface-to-volume ratio increases the exposed area in the air and enhances the sensing performance such as sensitivity and stability compared to polycrystalline ZnO [36].

Researchers have been carrying out investigations of the oxygen sensing behaviour of ZnO NPs. For instance, electrochemically deposited ZnO NPs were used to fabricate oxygen sensors, which showed a reversible response to oxygen [36]. However, the response speed was slow (the fall time is about 16.5min). Other researchers also noticed the thermal stability of the ZnO NPs-based oxygen sensor and they demonstrated that the oxygen sensitivity of ZnO NPs remains until 350°C , which indicated a wide range of operation temperature for ZnO NPs-based oxygen sensors [37].

It has also been reported that ZnO NPs are sensitive to the existence of other gas species. For example, ethanol sensitivity was observed and the researchers ascribed the sensing mechanism

to V_O -dependent concentration of free charge carriers [28]. Other mechanisms were also reported in NO_2 sensing, which was claimed to be a result of direct binding between NO_2 molecules and V_O on the surface of ZnO NPs [38].

A broad range of applications have incorporated ZnO NPs such as light emitting diodes (LEDs) with high brightness, UV lasers with extremely low thresholds, solar cells with efficient charge transport and UV detectors with high internal gain [22], [33], [34], [39]. ZnO NPs are also used in chemical and biological industries due to their antibacterial properties. Several antibacterial mechanisms have been reported such as the abrasive surface of ZnO NPs (edges and corners), the release of Zn^{2+} ions and the formation of reactive oxygen species (ROS) [13], [15]. However, the exact mechanism of antibacterial activity is still controversial.

1.2 Solution-Based Fabrication Processes for Thin Films and Features

Solution-based processes have several advantages over other fabrication techniques such as simple process, effective cost, high-yielding production and it is relatively easy to control their composition. Recently, low-temperature and solution-processed metal oxide semiconductor materials have been the centre of attention and researchers have attempted to fabricate transistors using InZnO, InGaZnO and ZnSnO from their solutions [40], [41]. Meanwhile, a wide range of applications have been reported using solution-processed metal oxide materials, such as UV photodetectors, biosensors and memory devices. [42]

However, it was reported that solution-processed semiconductor materials generally have worse electrical performance than vacuum-processed materials due to the low charge carrier mobility and poor film uniformity [42]. In order to improve the device's performance while maintaining a low processing temperature, attempts have been made such as using dual active layers, precursor optimization and high-pressure annealing.

Various techniques have been developed to process solution-based materials during the past decade such as spin coating, inkjet printing and spray pyrolysis. Spin coating is the most popular method, though it is also limited by the choice of pattern. In this section, different techniques for solution-based fabrication processes are introduced.

1.2.1 Spin coating

Spin coating is the most popular fabrication technique for thin films. Liquid precursor thins itself during the spinning in order to balance the centrifugal force and viscous force. Spinning parameters such as rotation speed, time and acceleration all play a significant role in film

thickness and uniformity. As a general rule, the film thickness is inversely proportional to $\sqrt{\omega}$, where ω is the angular speed of rotation.

The spin coating has several advantages such as low cost and fast operation. More importantly, it is able to provide a great film uniformity and the film thickness tend to remain itself during the process [43], [44]. On the other side, spin coating has a requirement for substrate size as it is difficult to rotate large-size substrate at high speed. In addition, the material usage is very low (<5%) [43] and the cost rises due to material disposal.

It has been reported that high-mobility transistors ($5.25 \text{ cm}^2/\text{Vs}$) based on ZnO precursor using spin coating was achieved [45]. The devices also showed a good stability over time. Highly reproducible transistors by spin-coating ZnO precursor were also realized and the transistors had a mobility of $6 \text{ cm}^2/\text{Vs}$ and current on/off ratio of around 10^6 [46].

1.2.2 Photopatterning

Traditional photolithography is possible for solution-processed thin films. However, this might bring about issues such as contamination and chemical reactions with photoresists or developers. Direct photopatterning was proposed by adding acetylacetone or benzoylacetone (BzAc) into metal oxide solutions [42]. UV illumination results in the decomposition of BzAc into oxides or hydroxide, which makes BzAc insoluble in the solvent (such as 2-methoxyethanol) [47]. It has been reported that InZnO-based transistors fabricated with direct photopatterning had a mobility of $7.8 \text{ cm}^2/\text{Vs}$ and a current on/off ratio of more than 10^8 [48]. InGaZnO transistors fabricated with the same method were also reported [49]. Moreover, femtosecond laser is also a potential technique for direct photopatterning and it was noticed that laser annealing enhanced the charge carrier mobility [50].

1.2.3 Printing

Printing is also a direct patterning technique with little material waste and high reproducibility. It can be further classified into contact printing, inkjet printing and nanoimprint lithography etc.

Contact printing has been widely used in the roll-to-roll process due to its high fabrication efficiency and capability in large-scale production. However, it is also limited by the pattern resolution and layer homogeneity. Moreover, contact printing requires high-viscosity inks. The most common type of contact printing is gravure printing, providing large throughput, low cost and large area. Researchers have used gravure printing to fabricate InGaZnO transistors with a field-effect mobility of $0.81 \text{ cm}^2/\text{Vs}$ and current on/off ratio of 1.36×10^6 [51].

Inkjet printing is the most promising technique to prevail in the real world. It is a direct and noncontact patterning method with a computer-controlled nozzle. The nozzle movement is pre-designed and controlled by computer, and the ink in the nozzle is ejected on a drop-on-demand basis. High-mobility transistor has been reported with a field-effect mobility of $16 \text{ cm}^2/\text{Vs}$ [41]. Likewise, InGaZnO-based transistor array was reported with a spacing of $50 \mu\text{m}$ [52]. Fully-aqueous ink was reported to fabricate indium oxide transistors and the transistor showed a great electrical performance with field-effect mobility of $19 \text{ cm}^2/\text{Vs}$ and current on/off ratio of 10^7 [53]. However, inkjet printing has notable disadvantages such as nonuniformity and coffee ring effect [42].

1.2.4 Mould-guided drying

Deposition by liquid drying was recently reported by Shunpu Li et al. in 2018 [54]. A PDMS template with proper line patterns was formatted using pouring commercial silicone elastomer (Sylgard ®184, Dow Corning). The commercial silicone elastomer consisted of a two-part liquid component kit (a 10:1 mix ratio). The commercial silicone elastomer was poured onto a master defined by optical or e-beam lithography. Then the PDMS was annealed at $70 \text{ }^\circ\text{C}$ for 1h. The solution was dispensed between PDMS template and substrate, followed by gentle pressure between them. The pressured contact was achieved through a self-developed stainless-steel clamping platform, which enabled the proper alignment of the substrates and PDMS template, and the easy adjustment of the pressure between them, as is shown in figure 1.2 below.

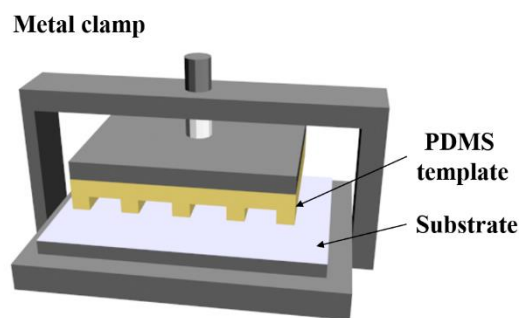


Figure 1.2 Illustration of mould-guided drying technique.

1.3 Introduction to Optically Addressed Spatial Light Modulators (OASLMs)

Spatial light modulator (SLM) is a type of liquid crystal (LC)-based device that is able to modulate amplitude, phase and polarization of light. It has been extensively used in a variety of applications such as pulse shaping [1], holographic displays [56], optical tweezers [57] and laser processing [58] etc. In particular, optically addressed SLM (OASLM) is attractive to holographic displays, which is very promising for true 3-dimensional displays. OASLMs based on ZnO NPs have been reported to be capable of high-resolution imaging (825 line pairs per millimetre) due to the trap states in ZnO NPs [3]. However, real-time 3D holographic displays based on OASLMs are still under development because of the stringent requirement for large spatial (size and diffraction angle) and temporal (refresh rate) bandwidth. Moreover, the requirement for diffraction efficiency and aperture size is also challenging [59].

SLMs can be classified into two types: electrically addressed SLMs (EASLMs) and optically addressed SLMs (OASLMs). The modulation of EASLMs is achieved by pixel matrix (CMOS circuitry) while OASLMs are controlled by the write light. A common type of EASLM is Liquid Crystal on Silicon (LCoS), with a layer of LCs sandwiched between integrated pixel circuit and ITO. On the contrary, there is no complex integrated circuit in OASLM, but it requires a layer of photoactive material so that the resistivity can be modulated by the write light. The structures of LCoS and OASLM are illustrated in figure 1.3 below.

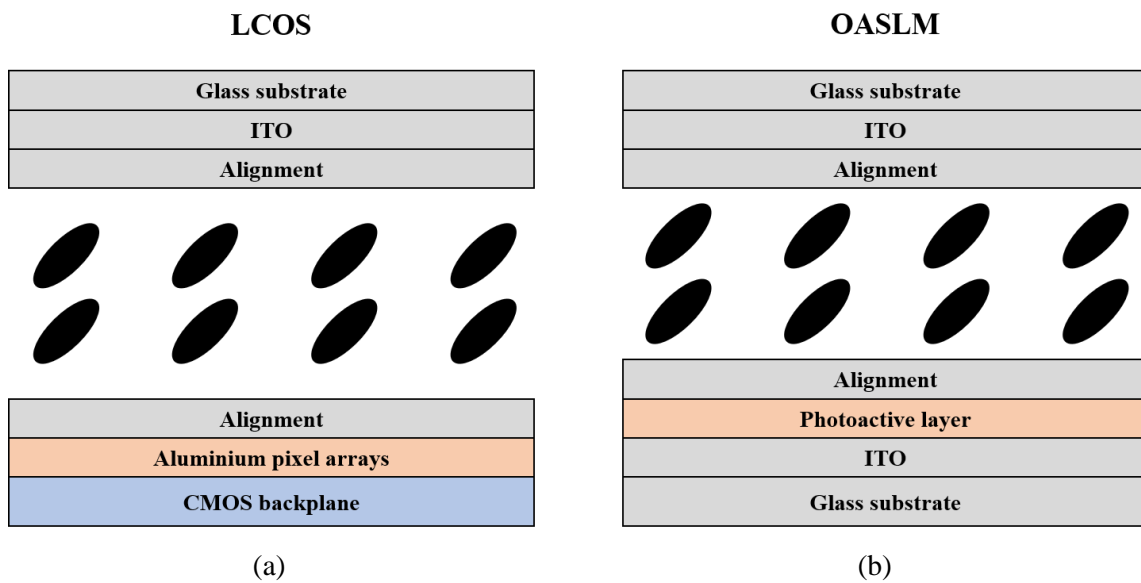


Figure 1.3 Structure of (a) LCoS. and (b) OASLM.

Phase-only LCOS is based on electrically controlled birefringence (ECB) effect of LCs, without any polarizers or light-absorbing material. Not only has it been used in real-time holography [60], it has also attracted attentions from wavelength selective switch (WSS) [61] and optical correlators [62] etc. However LCOS devices are still challenged by the large pixel size, small pixel fill factor and dead-space diffraction etc [63].

In contrast, OASLMs are able to provide higher resolution without complicated pixel and addressing circuitry. This is particularly important for holographic displays as wider viewing angle can be realized by smaller pixel pitch. In addition, the absence of pixel also eliminates the dead space between pixels, which creates undesired diffraction pattern in the reconstructed image. Thirdly, large-area OASLMs are possible while LCOS devices are always limited by the panel size (a few inches in diagonal). More importantly, OASLMs are low-cost and easy-fabrication devices because they have no pixel and CMOS backplanes.

1.3.1 Working principles

The light modulation in OASLMs is achieved by the photoactive material or structure (photodiode). The photoactive material is generally photoconductive, and its electrical conductivity increases dramatically once it is illuminated by the write light. As a result, the voltage drop across LCs increases and electrically controlled birefringence (ECB) occurs, as is shown in figure 1.4 below.

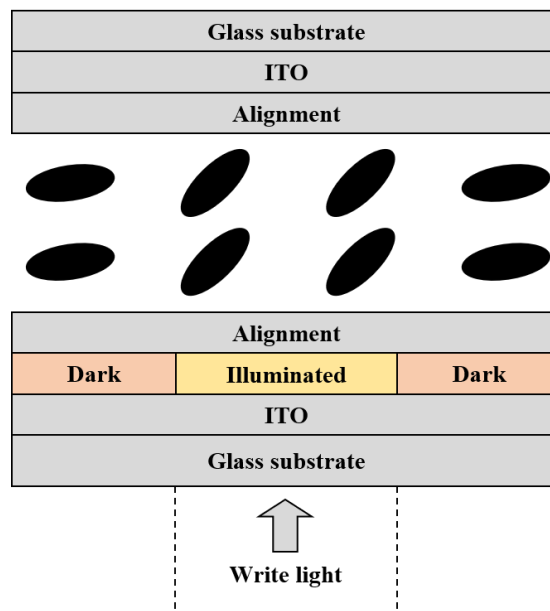


Figure 1.4 Working principles of OASLMs.

LCs rotate vertically when they are illuminated by the write light while LCs without write light illumination remain parallel to the alignment layer. Therefore, the read light propagating

through LCs is modulated by the write light. Transmissive and reflective architectures are both available in OASLMs.

1.3.2 Fundamentals of liquid crystals

Liquid crystals are a type of liquid-like crystalline mesogen, exhibiting liquid properties such as fluidity, and they also behave like crystals such as their optical, electrical, magnetic and mechanical anisotropies. Since the discovery in the late 19th century by Friedrich Reinitzer [64], liquid crystals have been developed into one of the most widely-used materials in the modern world. Particularly, LCs revolutionized the society in display applications (LCDs), which has been dominant in smartphones, tablets and laptops etc. In addition, LCs are still playing a key role in applications such as thin-film thermometers [65], organic field effects transistors (OFETs) [66] and organic solar cells [64] etc. Attempts have never been stopped by researchers to find out more applications such as templating nano-structured materials in material science [67], elastic actuators [68] and drug delivery in pharmaceutical industry [69].

- **Classifications of LCs**

Based on the molecular arrangement, LCs can be classified into several mesophases: nematic LCs, cholesteric LCs and smectic LCs, as is shown in figure 1.5 (a) ~ (e). Nematic LCs have uniaxially symmetric molecules with elliptical shapes. The most significant feature of nematic LCs is that the molecules (molecular long axes) tend to be parallel to each other in order to have the minimum free energy and the preferred direction is described by the director (\vec{n}). Accordingly, the molecular long axis has long-range orientational order. However, the molecules have no positional order of their mass centre, which results in their fluidity. Cholesteric LCs are similar to nematic LCs as cholesteric LCs also have orientational order and no positional order in a certain plane, while the director of each plane changes continuously between adjacent planes. As a result, cholesteric LCs have a twisting and rotating director perpendicular to the director planes. Periodic rotation of cholesteric LCs is defined by pitch, which is twice the periodicity. Nematic LCs can be considered as a specific kind of cholesteric LCs with infinite pitch.

Smectic LCs have a stratified molecular arrangement and sliding movement exists between layers. Smectic LCs are further categorised into smectic A, B and C mesophases based on their molecular orientation and position within each layer. Molecules of smectic A LCs are perpendicular to the layers and that of smectic C LCs are tilted to the layers. Besides the layered structure, Smectic B LCs also have positional order within each layer.

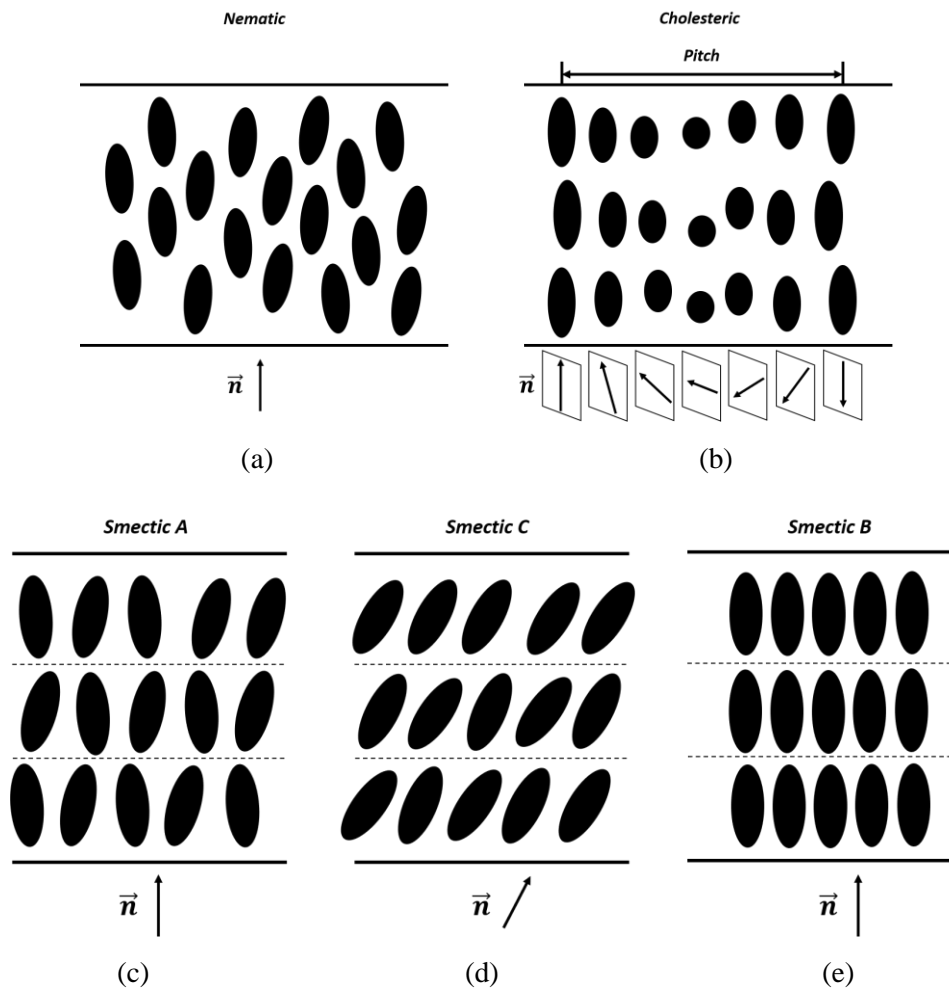


Figure 1.5 Molecular arrangement of (a) nematic LCs. (b) cholesteric LCs. (c) smectic A LCs. (d) smectic C LCs and (e) smectic B LCs.

LCs of a certain mesophase can be transformed into another. For instance, nematic LCs can be transformed into cholesteric LCs by adding chiral dopant. Temperature also influences the phase transition and lower temperature generally corresponds to a higher crystalline or positional order. Therefore, different mesophases of LCs occur in the order of smectic B, smectic C and smectic A as the temperature increases. Nematic LCs has the lowest crystalline order so they normally emerge at the highest temperature. Aforementioned LCs are also called thermotropic LCs, which indicates the temperature dependency of phase transitions. Other types of LCs such as lyotropic LCs are not discussed in this dissertation.

In this work, nematic LCs were studied and used to fabricate OASLMs devices so nematic LCs will be discussed in detail in the following sections.

- **Scalar order parameter**

In order to simplify the model, nematic LCs are regarded as elongated and rigid molecules (like rods) with uniaxial and central point symmetry, as is shown in figure 1.6. Macroscopic (still small volume) orientation order of LCs are described by second rank tensor, while microscopic orientation order is represented by scalar order parameter S . In the case of nematic LCs, molecular arrangement can be characterised by scalar order parameter (S) and director (\vec{n}). Although molecules of nematic LCs have a preferred and averaged direction (director), the orientation between each molecule is not exactly the same. Moreover, the orientation of each molecule also changes with time due to thermal motion and intermolecular force. Therefore, the molecule positioned in a certain angle (θ) to the director (\vec{n}) is probabilistic and this probability is represented by orientation distribution function $f(\theta)$. S is equal to 0 when LCs are in isotropic phase. Nematic LCs have a S less or equal to 1, where 1 represents ideal alignment of LCs.

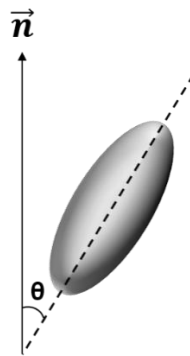


Figure 1.6 The orientation of nematic LCs molecules.

- **Elastic properties**

The distribution of nematic LCs under electric field is quantitatively explained by elastic continuum theory, which states that LCs always orient themselves in a way that the total free energy is the minimum. Deformation is generated under external electric field and elastic force arises to resist the deformation and brings the LCs back to the equilibrium position. The most common deformation inside nematic LCs are splay, twist and bend, as is shown in figure 1.7.

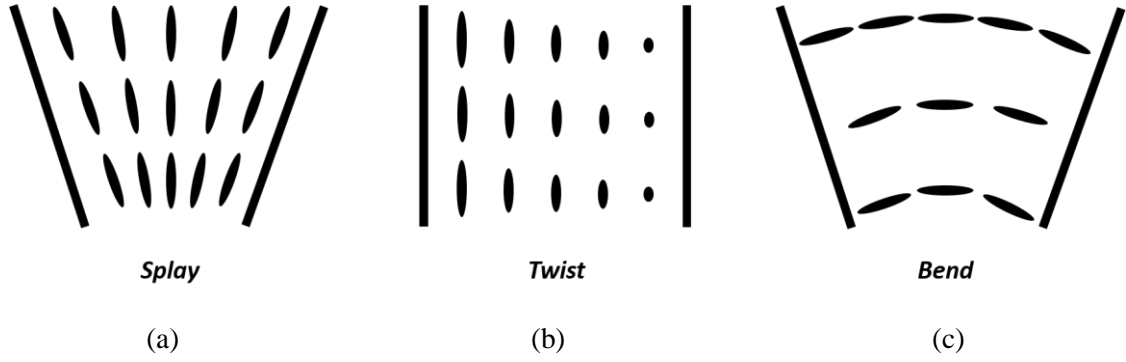


Figure 1.7 Three types of deformation of LCs: (a) splay, (b) twist, and (c) bend.

Similar to Hooke's law, the elastic stress or torque is proportional to the displacement of director and the proportionality is defined by elastic constant k , firstly developed by Frank [70]. The elastic constants for splay, twist and bend deformation are referred to as k_1 , k_2 and k_3 respectively.

The elastic free energy density (f) is also a function of elastic constants and it is expressed as:

$$\begin{aligned}
 f_{splay} &= \frac{1}{2} K_1 (\nabla \cdot \mathbf{n})^2 \\
 f_{twist} &= \frac{1}{2} K_2 (\mathbf{n} \cdot \nabla \times \mathbf{n})^2 \\
 f_{bend} &= \frac{1}{2} K_3 (\mathbf{n} \times \nabla \times \mathbf{n})^2
 \end{aligned} \tag{1.1}$$

The total elastic free energy is determined by adding three types of elastic energy together. Generally, elastic constants are different in magnitude and k_3 is the largest compared to k_1 and k_2 in nematic LCs.

- **Dielectric and optical anisotropy**

Dielectric anisotropy is the most important property of LCs, which is also the origin of optical anisotropy. Dielectric constant (ϵ) is to describe the response of dielectric materials to electric field (E), and it is defined as:

$$\mathbf{D} = \epsilon \mathbf{E} \tag{1.2}$$

where D is the electric displacement field. The lowest possible dielectric constant is in vacuum, which is called absolute dielectric constant or vacuum dielectric constant (ϵ_0). Relative dielectric constant (ϵ_r) is the ratio of ϵ and ϵ_0 .

Relative dielectric constant (ϵ_r) is related to electric susceptibility (χ) by:

$$\boldsymbol{\varepsilon}_r = \boldsymbol{\chi} + \mathbf{1} \quad (1.3)$$

Electric susceptibility (χ) is a measure of polarization of the dielectric material in an electric field. Therefore, electric displacement (D) can also be written as:

$$\mathbf{D} = \varepsilon_0 \boldsymbol{\varepsilon}_r \mathbf{E} = \varepsilon_0 (\boldsymbol{\chi} + \mathbf{1}) \mathbf{E} = \varepsilon_0 \mathbf{E} + \mathbf{P} \quad (1.4)$$

where P is the dielectric polarization density, and it represents the strength of polarizations within the dielectric material. Dielectric constant is also called permittivity, which is a scalar in isotropic medium and second rank tensor in anisotropic medium (LCs).

For the purpose of simplification, LC molecules are generally assumed to be uniaxial and have the rotational symmetry, as is shown in figure 1.8. Refractive index (n) reflects the dielectric properties at light frequencies and the refractive index is related to the dielectric constant by:

$$\mathbf{n} = \sqrt{\boldsymbol{\varepsilon}} \quad (1.5)$$

Like dielectric anisotropy, refractive index is also anisotropic. The most important property of nematic LCs is the birefringence (Δn). Birefringence can be defined as:

$$\Delta n = n_e - n_o \quad (1.6)$$

where n_e is the extraordinary refractive index and n_o is the ordinary refractive index. Extraordinary refractive index (n_e) is parallel to the director and ordinary refractive index (n_o) is perpendicular to the director. Nematic LCs have a typical ε_e of 2.89 and ε_o of 2.25 (corresponding refractive indexes are 1.7 and 1.5) [70]. Most nematic LCs have a positive birefringence (Δn) and it is generally in the range of 0.05~0.45 [63].

The discussion above assumes that the propagation direction of incident light (\vec{k}) is along the director, as is shown in figure 1.8 (a). In the case of tilted incident light as shown in figure 1.8 (b), ordinary refractive remains consistent due to rotational symmetry. Based on the elliptic function of index ellipsoid, equivalent extraordinary refractive index (n'_e) can be re-written as:

$$\mathbf{n}'_e = \frac{1}{\frac{\cos^2 \theta}{n_o^2} + \frac{\sin^2 \theta}{n_e^2}} \quad (1.7)$$

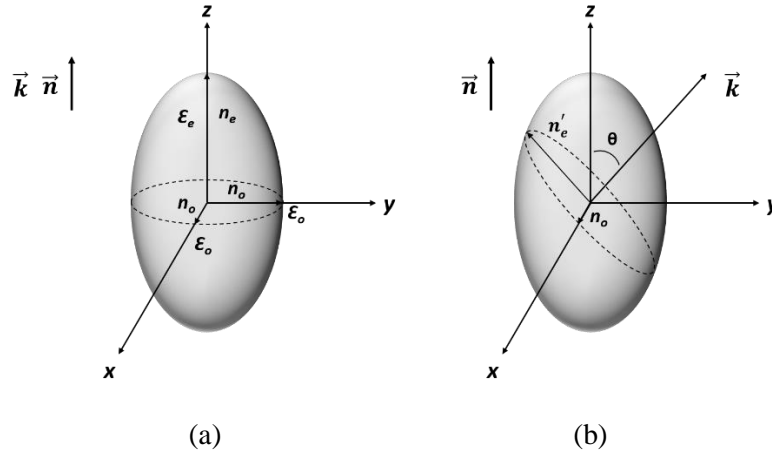


Figure 1.8 Anisotropy of LCs when wave vector (\vec{k}) and director (\vec{n}) are (a) aligned and (b) not aligned.

- **Electro-optical effect**

The most important property of LCs is the response to electric field. Because of the uniaxial and elongated geometry of nematic LCs, they have dielectric anisotropy. In the presence of electric field (E), the free energy increases. Nematic LCs molecules ($\Delta n > 0$) will reorient to reach the minimum free energy and as a result align with the direction of electric field, as is shown in figure 1.9. Dielectric response means little current is associated during operation, which makes LCs consume very little power and generate trivial amount of heat. However, impurities exist in practice, which enhances the conductivity of LCs, so AC voltage is used to prevent LCs degrading in this case.

A simple model is shown below:

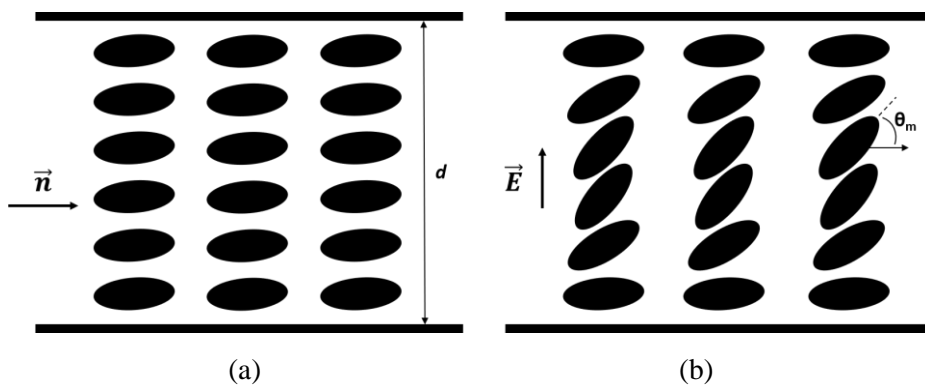


Figure 1.9 Molecular orientation of LCs (a) without electric field and (b) under DC voltage.

If the incident light propagates vertically through the LCs (electric polarization direction of the light is parallel to the director of LCs), the phase retardation (ϕ) due to electrically controlled birefringence (ECB) is defined as:

$$\varphi = \frac{2\pi\Delta nd}{\lambda} \sin^2 \theta \quad (1.8)$$

Assuming LCs molecules are parallel to each other along the propagation path. However, in real cases, orientation angle is position-dependent due to surface anchoring effect and elastic forces between molecules etc.

Nematic LCs are often anchored at the substrates by micro-grooves (alignment layer), posing a small pre-tilt angle to the substrate. Once an electric field is applied, the LCs tend to align with the direction of electric field ($\Delta n > 0$). The rotation of LCs is opposed by the anchoring effect near the substrates and the elastic force between molecules. As a result of competition, LCs start to rotate when the electric field reaches a certain threshold intensity (E_{th}), which is also called Freedericksz's transition voltage. The anchoring effect is least significant in the middle of the cell so LCs molecules in the middle have the maximum rotation angle (θ_m).

The phase shift in real cases is much more complicated and it requires a full rotation angle profile along the propagation direction to derive the overall phase shift. Therefore, this is carried out in simulations in the later part.

1.3.3 Challenges

OASLMs are also facing several challenges such as resolution and response time. Although OASLMs have no pixels, their resolution is limited by the electrical fringing field in the LCs layer and lateral diffusion of photo-excited charge carriers in the photosensitive layer. Moreover, electric field in the photosensitive layer also results in spatially varying distribution of charge carriers, which further degrades the resolution.

The electrical fringing field in LCs is strongly affected by the thickness of LCs layer so thinner LCs layer is preferred. On the other side, the phase modulation depth is compromised as the thickness decreases. In the meanwhile, the electrical fringing field also exists in the photoactive layer, though it is less serious than that in the LCs layer because the photoactive layer is much thinner than LCs layer. There is also a compromise between the electrical fringing field and photo sensitivity since thinner photoactive layer helps to ease the fringing effect but also worsens the sensitivity such that the voltage drop across LCs is not large enough to switch LCs.

The lateral diffusion of charge carriers is inevitable due to the concentration gradient. The diffusion length (L) is a function of mobility (μ) and charge carrier lifetime (τ), as is shown below in equation 1.9:

$$L = \sqrt{\tau \frac{k_B T}{q} \mu} \quad (1.9)$$

where k_B is the Boltzmann constant and T is temperature. Charge carrier lifetime can be decreased by introducing charge traps or defects (recombination centres). On the other hand, photogenerated charge carriers drift in the photoactive layer along the electric field from one side to the other and are accumulated at the interface. So, the carrier transit time is also important. The transit time can be minimized by thinning the thickness of photoactive layer and increasing the applied voltage.

Another limit on resolution comes from the charge spreading at the interface between the photoactive layer and LCs layer [71], [72]. The charge spreading at the interface is a result of gradient diffusion and lateral drift by electric fringing field. The charge accumulates after the write light is on. More importantly, the trap states at the interface also determines the resolution. The existence of trap states stops charge carriers from lateral diffusion, however, they also introduce other issues such as residual image and long turn-off time.

The response time of OASLM is also challenging. It is jointly determined by LCs and the photoactive layer. The response time of LCs under electric field is dependent on the electric field intensity, elastic constant and viscosity of LCs. Stronger E-field results in larger dipole moments and torque, while smaller elastic constant and less viscosity weaken the rotating resistance.

Different types of LCs have various response time. Ferroelectric LC (FLC) is a kind of fast-switching LC and it responds to both the magnitude and polarity of electric field. In addition, FLC can be made bi-stable such that molecular orientation maintains itself without consuming electric power. Nematic LCs can generally provide a refresh rate up to 120Hz while ferroelectric LCs can be operated at a maximum rate of 1015Hz [63]. However, FLC can only provide binary phase modulation compared to continuous and multilevel phase modulation by nematic LCs. Moreover, FLC is limited by the low diffraction efficiency (light diffracted into zero order and conjugate image) and large quantization noise [63].

Photoactive material is also a limiting factor since the photogenerated charge carriers are trapped at the interface with LCs, maintaining the voltage across the LCs ('on' state) and causing residual image. The charge trapping time can be much longer than the rise time (switching on and off time are typically $\sim 100\mu\text{s}$ and $\sim 20\text{ms}$ respectively for nematic LCs) [73].

Crystalline or amorphous photosensitive material are often used because of less trap states. Photodiode is also an alternative to photoactive layer for high-speed OASLMs.

1.3.4 Current progress

The development of high-performance OASLMs has been progressive since the last century. The early version of OASLM was built up using a-Si:H p-i-n photodiode and Ferroelectric LC, providing a response time of 155 μ s and resolution of 40 lp/mm [74], [75]. Higher resolution (175 lp/mm) was then achieved by using a thinner photoactive layer [76]. By doping a-Si:H with carbon, the resolution was further enhanced to 370 lp/mm [77].

Other photoactive materials were also attempted such as ZnO [78], BSO [79], AsSe [80], and a-As₂S₃ [81]. Using infrared (IR) light as the write light was reported for night vision applications using lead chalcogenides (PbS) [82]. Polymer photoconductive material was used to provide a resolution of 527 lp/mm [83]. The highest resolution of 825 lp/mm was reported using ZnO NPs due to the trap states in ZnO NPs.

1.4 Sensor for Oxygen Partial Pressure in Air

Oxygen sensors are playing an increasingly significant role in the 21st century since oxygen is one of the most crucial indicators in a wide range of applications such as air-fuel mixture controller in the combustion engine, exhaust emission monitor of industrial boiler and waste management industries [84]–[86]. Various oxygen sensing technologies have been invented such as potentiometric equilibrium sensors, limiting current amperometric sensor and semiconductor-based sensor etc. [87] Oxygen partial pressure sensors are evaluated by three criteria: sensitivity, selectivity and response time. Besides these, stability, reversibility and power consumption are also important factors to be considered.

1.4.1 Semiconductor-based oxygen partial pressure sensor

Semiconductor-based oxygen sensor is generally related to the defect states in the material. These oxygen sensitive materials are generally n-type metal oxide, whose physical properties (typically electrical conductivity) are strongly dependent on the oxygen vacancies [87]. Oxygen in air tends to be adsorbed onto the surface of these metal oxide by capturing free electrons. The electrical conductivity (σ) is normally related to the oxygen partial pressure in air (P_{O_2}) by the following equation [87]:

$$\sigma = A \exp\left(-\frac{E_A}{kT}\right) P_{O_2} \quad (1.10)$$

where A is a constant, E_A is the activation energy and T is the temperature.

Researchers have used different types of semiconductor materials such as CeO_2 [88], Nb_2O_5 [89], SrTiO_3 [90] and TiO_2 [91] etc. for oxygen sensing. It has been reported that TiO_2 -based oxygen sensor was capable of measuring the oxygen concentration from 10^{-23} Bar to 1 Bar [91]. Nb_2O_5 was also used to measure oxygen partial pressure under high temperature from 400°C to 800°C and the minimum measurable oxygen pressure is 10^{-5} Bar [89]. Even higher measurement temperature of 1400°C was reported by using SrTiO_3 and the lowest measurable oxygen pressure is 10^{-2} Bar [90]. Fast response time for oxygen pressure sensor was reported by using CeO_2 nanoparticles and it was also found out that the response time decreased with smaller particle size (10 times faster for CeO_2 nanoparticles with 200nm in diameter than that of $2\mu\text{m}$ in diameter).

1.4.2 ZnO-based oxygen partial pressure sensor

ZnO is also sensitive to the presence of oxygen in air. In the meanwhile, ZnO is particularly captivating because it is thermally stable and robust, able to provide a relatively fast response and a possibility for miniaturized size [92]. The oxygen sensing mechanism of ZnO has been investigated across the world. It has been widely accepted that oxygen in air is chemisorbed on the surface of ZnO, which depletes the electrons from conduction band and decreases the electrical conductivity. Depending on the measuring temperature, different oxygen species were identified in ZnO. Some researchers found that O_2^- , O^- and O^{2-} were formed at temperatures below 100°C , between 100°C and 300°C , and above 300°C respectively [92].

Polycrystal ZnO by sputtering has been reported to detect oxygen pressure with a slow response time of about 1h [92]. They also noticed that glass substrate was better than silicon substrate in terms of sensitivity due to the amorphous nature of glass surface. ZnO nanowire field-effect transistor was also reported as an oxygen sensor, with a minimal sensing limit for oxygen pressure of 1.3×10^{-5} Bar. Suspension of ZnO nanoparticles, along with graphite electrode were reported to be capable of detecting the minimal oxygen concentration of $27.6\text{g}/\text{cm}^3$ [93]. In addition, various methods have been attempted to improve the oxygen sensing performance. For instance, metal catalysts (such as Pt and Pd) was used to increase the sensitivity and to decrease the working temperature of ZnO-based oxygen sensor [94]. The use of compound oxide semiconductors and ZnO/CuO heterojunction was also reported to improve the selectivity [95].

Chapter 2 Preparation and Characterization of

Solution-Processed ZnO NP Thin Films

The unique and outstanding properties of solution-based ZnO NPs such as wide and direct bandgap, optical transparency in the visible range, rich and tuneable defect states, low-cost and large-scale production etc. have made ZnO NPs particularly promising for a wide range of future applications. Therefore, the fundamental physics of solution-processed ZnO NPs and the working principles of ZnO NPs-based devices are particularly significant. The purpose of this chapter is to investigate the fundamental properties of ZnO NPs and the effect of post-processing on ZnO NPs. Sample preparation is discussed at the beginning of this chapter, and properties of ZnO NPs such as electrical conduction mechanisms, dielectric response and optoelectronic behaviours are then characterized. The effect of thermal annealing and oxygen plasma is discussed at the end of this chapter.

2.1 Sample Preparation

The raw material of ZnO NPs was purchased from Sigma-Aldrich, in the form of colloidal dispersion in ethanol (product number: 721085, LOT number: MKBK0418V). The weight percentage of ZnO NPs dispersion is 41% and the density is 1.25g/ml. In addition, the average particle size of ZnO NPs is 89nm, measured by dynamic light scattering (DLS). These data are provided by the supplier (on the Certificate of Analysis).

Thin-film ZnO NPs were prepared by spin-coating. The substrate is composed by an n-type silicon (Si) layer at the bottom and a 300nm-thick silicon dioxide (SiO₂) layer at the top (insulating layer). Firstly, the substrate was cleaned by DI water, acetone and isopropyl alcohol (IPA) consecutively for 10min each in an ultrasonic bath, prior to oxygen plasma treatment (300s). The oxygen plasma was used to remove organic contaminations from the surface and to make the surface hydrophilic, which is very crucial to form a uniform thin film of ZnO NPs. The ZnO NPs dispersion was then spin-coated on the substrate with a rotation speed of 4000RPM for 30s. The acceleration speed was 500RPM/s, which was proved experimentally to provide the best film quality. The sample was further baked on a hotplate at 100°C in air for 10min to evaporate the solvent (the boiling point of ethanol is 78.37°C at atmospheric pressure). Finally, the sample was annealed in a furnace at 400°C in air for 3h to thoroughly remove the organic contaminations and to make ZnO NPs thin film better in crystallinity.

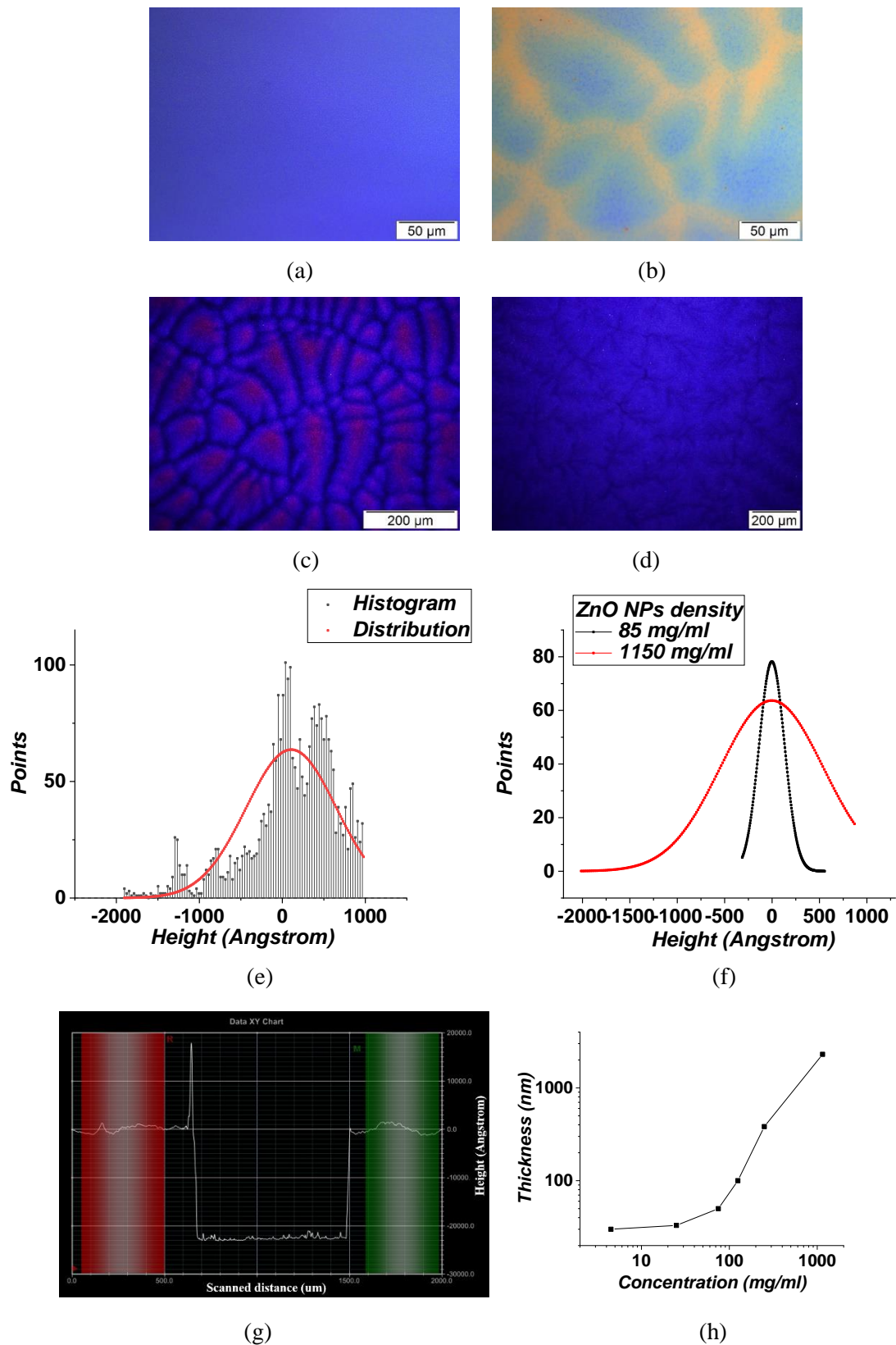


Figure 2.1 Surface of ZnO NPs thin films prepared by different ZnO NPs concentrations (a) 4.5mg/ml. (b) 125mg/ml. (c) 250mg/ml. (d) 1150mg/ml. (e) The histogram and distribution of film height. (f) Comparison of height distribution between films of 4.5mg/ml and 1150mg/ml. (g) Film thickness measured by surface profiler. (h) Film thicknesses of different ZnO NPs concentrations.

Dilution of ZnO NPs dispersion is necessary in order to form high-quality ZnO NPs thin films. Better uniformity in film thickness can be achieved through diluted dispersion due to less viscosity. ZnO NPs thin films prepared from different concentrations (4.5mg/ml, 25mg/ml, 85mg/ml, 125mg/ml, 250mg/ml and 1150mg/ml) were inspected under optical microscope (these films were prepared with the same fabrication parameters), as is shown in figure 2.1 (a) to (d). It is evident that ZnO NPs dispersion of 4.5mg/ml could form a uniform ZnO NPs film (figure 2.1 (a)) while the film uniformity degraded at higher concentrations above 125mg/ml (figure 2.1 (b) to (d)). Patterns were generated during spin-coating and they became more prominent at higher concentrations as a result of higher viscosity. Dark-field microscopy was used in figure 2.1 (c) and (d) to provide a better contrast of the pattern.

The film surface was also investigated by Dektak surface profiler. The histogram of film height and its distribution are shown in figure 2.1 (e). This is a good method to visually observe the height variation. The height distribution is compared between ZnO NPs films of 85mg/ml and 1150mg/ml in figure 2.1 (f). It is evident that 85mg/ml film has a narrower height distribution while 1150mg/ml film has a wider spread over the height spectrum, signifying a larger height variation. The mode of height distribution is zeroed. In addition, the film thickness was also investigated for different concentrations of ZnO NPs, as is shown in figure 2.1 (g) and (h). A trench was drawn mechanically on the sample surface by a plastic sharp. The peak in figure 2.1 (g) results from the debris at the edge. It can be concluded from figure 2.1 (h) that higher concentration results in a greater film thickness.

By comparing the film quality of different ZnO NPs densities, 85mg/ml ZnO NPs dispersion was used to prepare samples for material characterization in the following section. The rest fabrication parameters were kept identical, as was described above.

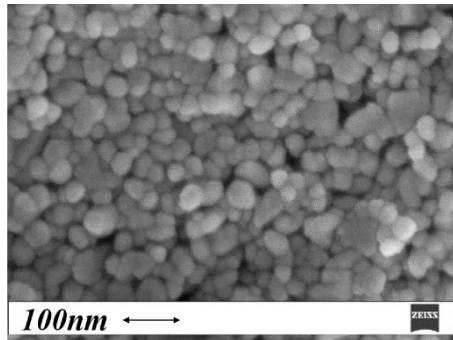
2.2 Characterization of ZnO NP Thin Films

ZnO NPs were characterized in terms of physical, electrical, dielectric and optical properties. This part of work is significant to understand ZnO NPs and to customize ZnO NPs-based devices.

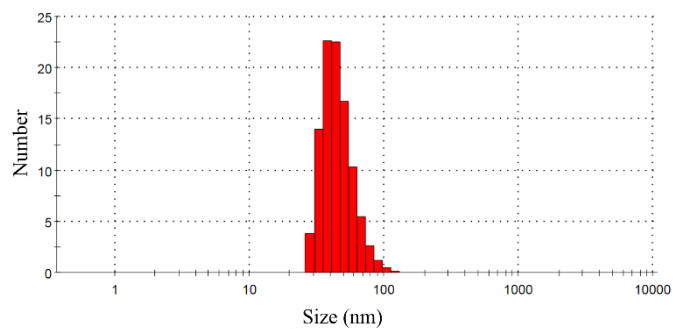
2.2.1 Particle size

The size of ZnO NPs was firstly investigated by scanning electron microscope (SEM). SEM is capable of providing high-resolution (in nanometre scale) images of the target by detecting the secondary electrons from the surface. Secondary electrons from the surface (5nm~10nm) have

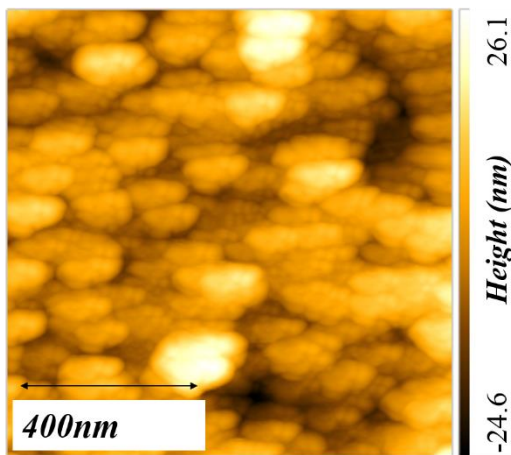
relatively low energy ($<50\text{eV}$) and they are extremely sensitive to the surface structures. In order to have high-resolution images of ZnO NPs, the sample was coated with Au and Pd beforehand so that the electrons do not accumulate on the surface (ZnO NPs are semiconductive with low conductivity). Charge accumulation on the target surface could result in dark images. Zeiss LEO Variable Pressure SEM was used to observe the nanoparticles and the result is shown in figure 2.2 (a). It is clear that the film is composed by nanoparticles with $\sim 30\text{nm}$ in diameter and gaps exist among nanoparticles.



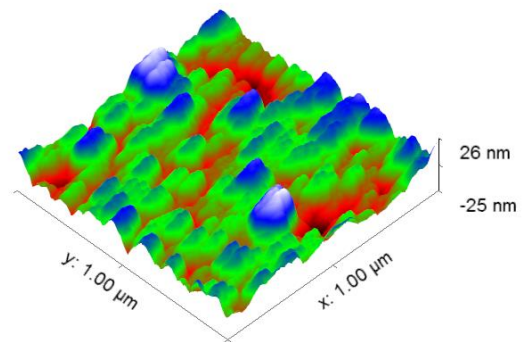
(a)



(b)



(c)



(d)

Figure 2.2 (a) SEM image of ZnO NPs. (b) Size distribution of ZnO NPs by DLS. (c) Surface profile measured by AFM. (d) 3D contour of ZnO NPs surface, generated by AFM measurement.

Dynamic light scattering (DLS) was also performed on ZnO NPs dispersion (25mg/ml in ethanol, required by the equipment) using Malvern Zetasizer in order to determine the size variation and distribution. DLS is a technique that measures the Brownian motion of colloidal ZnO NPs by detecting the intensity of light scattered by ZnO NPs. The particle size is determined by the Stokes-Einstein relationship. The result is shown in figure 2.2 (b) and the average diameter of ZnO NPs is measured to be 73.2nm, which is slightly smaller than the data

from the supplier. In addition, the DLS analysis confirms that the particle size is ranging from 25nm to 100nm, with a mode (the majority) of about 30nm. This is consistent with SEM images. The surface of ZnO NPs thin film was inspected by DI3100 Atomic Force Microscopy (AFM). Figure 2.2 (c) shows the surface profile in the tapping mode of AFM. The tip taps the sample surface and scans line by line throughout the $1\mu\text{m}\times 1\mu\text{m}$ area. The 3D height map is also shown in figure 2.2 (d). It is evident that the sample surface is not perfectly uniform, and the maximum variation in height is about 60nm, which is around twice the average particle diameter (30nm). In addition, the mean surface roughness is 5.8nm.

2.2.2 Composition

The composition of the sample was investigated by energy-dispersive X-ray spectroscopy (EDX). Similar to SEM, a beam of electrons with a high energy impact on the sample and excite its electrons from a low energy state (inner shell) to high energy state (outer shell), leaving holes at the inner shell. These holes are then filled by electrons from the high energy state (outer shell), which releases energy in the form of X-ray. The characteristic X-ray is unique for different elements with different atomic numbers and it is often used to identify compositional elements.

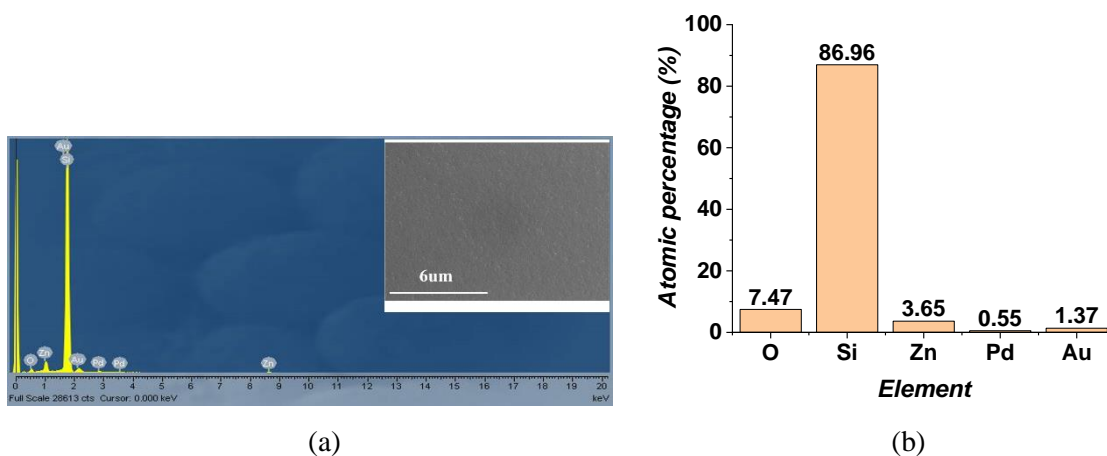


Figure 2.3 (a) EDX spectrum of ZnO NPs. (b) Atomic ratio of composing elements

The EDX results are shown in figure 2.3 (a) and an area of about $15\mu\text{m}\times 15\mu\text{m}$ was investigated (inset on the top right). The EDX spectrum shows the compositional elements of Zn, O, Si, Au and Pd. The Y axis indicates the relative content of each element. The spectrum confirms the sample purity since there are no other elemental peaks. One thing to be noted is that there are two peaks for “Zinc” in the spectrum because electrons from different energy levels (1 keV and

8.6 keV corresponds to L line and $K\alpha$ line respectively) are recombined with holes at the inner shell. The SiO_2 substrate was also detected.

The elemental percentage is further calculated by taking the atomic weight into account and the atomic ratio of these elements are shown in figure 2.3 (b). The atomic ratio of oxygen and zinc is 2.05, which implies that the sample is oxygen-rich. On one hand, the oxygen content comes from the adsorbed oxygen onto ZnO NPs. On the other hand, it might come from the organic surfactant of ZnO NPs dispersion. Surfactant is generally used to form liquid suspension with well separated nanoparticles.

Oxygen plasma was used to verify the existence of organic surfactant. It is generally accepted that oxygen plasma treatment results in a decrease in conductivity because the dopant density (hydrogen and hydroxyl group) was reduced after oxygen plasma treatment [96]. Two identical ZnO NPs samples were fabricated and one ZnO NPs sample was treated with oxygen plasma (5% for 5min). The I-V characteristics were measured after a week and the results in figure 2.4 (a) clearly show that oxygen plasma treatment results in a reduction in conductivity in the ohmic region.

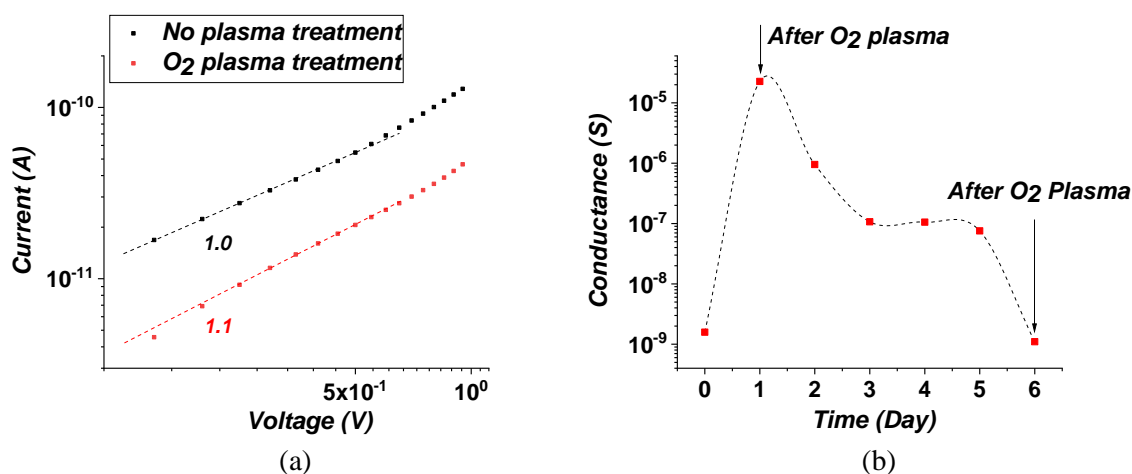


Figure 2.4 (a) I-V characteristics of ZnO NPs with and without oxygen plasma treatment. (b) The conductance of ZnO NPs tracked after plasma treatment.

The conduction of ZnO NPs after plasma treatment was tracked day by day, as is shown in figure 2.4 (b). Oxygen plasma treatment was conducted on day 1 and the conductance was measurement immediately. It is clearly shown that the electrical conductance increased dramatically by an order of 10^4 (opposite to the previous result). This is due to the elimination of organic surfactant since it forms a highly resistive shell around nanoparticles. Then the sample was left in the air and the conductance was measured daily. The conductance decreased

as the oxygen in the air was gradually adsorbed, forming a depleted boundary (shell) by capturing free electrons from ZnO NPs. The conductance reached a stabilized value after day 3. Oxygen plasma treatment was performed again on day 6 and a decrease in conductance was noticed due to the annihilation of oxygen vacancies. This was also confirmed by EDX. The atomic ratio of O/Zn is 2.27 for plasma-treated ZnO NPs, compared to 2.05 for untreated ZnO NPs. Therefore, the organic surfactant contributes to the oxygen content in ZnO NPs sample.

2.2.3 Lattice structure

ZnO NPs can be regarded as a massive number of nano-sized ZnO crystallites, so ZnO NPs also possess lattice property. The lattice structure was investigated by X-ray diffraction (XRD). XRD is based on the Bragg's law, from which the lattice parameters can be determined by the diffraction pattern. The result is shown in figure 2.5 below.

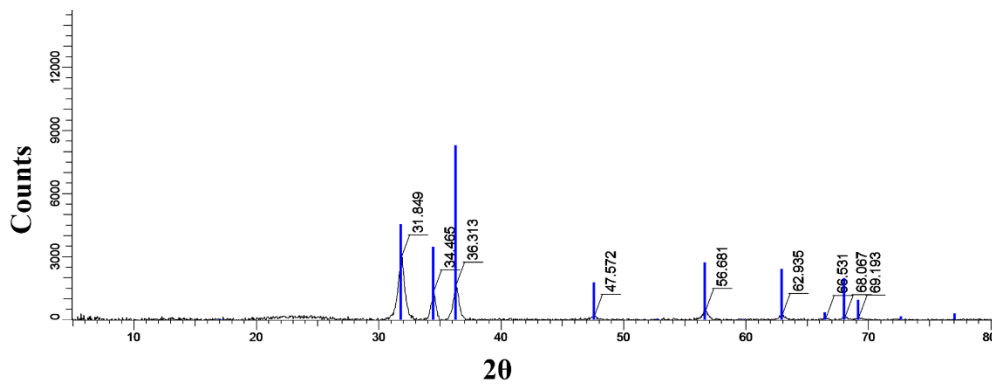


Figure 2.5 XRD pattern of ZnO NPs

The diffraction pattern in figure 2.5 confirms the crystalline nature of ZnO NPs and the pattern also shows a good consistency with hexagonal oxygen-rich ZnO ($Zn_{0.98}O$, PDF 01-082-2975). In addition, the average size of ZnO crystallite (τ) can be determined by the wavelength (λ) of X-ray, full width at half maximum (FWHM) of the diffraction pattern (β) and the Bragg angle (θ), according to Scherrer equation:

$$\tau = \frac{K\lambda}{\beta \cos\theta} \quad (2.1)$$

where K is the shape constant with a typical value of 0.9 [97], [98]. The average size of the crystalline domain is calculated to be 4.14nm, which is consistent with typical crystalline size.

2.2.4 Electrical conduction mechanism

Electrical conduction mechanism of ZnO NPs was investigated by I-V measurement. Agilent 4156 (Yokogawa-Hewlett-Packard Ltd, Tokyo, Japan) semiconductor analyser was used to

measure the I-V characteristics. ZnO NPs sample was fabricated in a planar structure, as is shown in figure 2.6 (a). Only the source and drain electrodes were used in this case. ZnO NPs dispersion was spin-coated on the substrate (same as before) and Al electrodes (50nm in thickness) were deposited by thermal evaporation as electrodes (with a gap of 80 μ m). Al was selected as the electrode material because the Al-ZnO NPs contact is Ohmic [7] so that the I-V characteristics reflect the bulk properties of ZnO NPs.

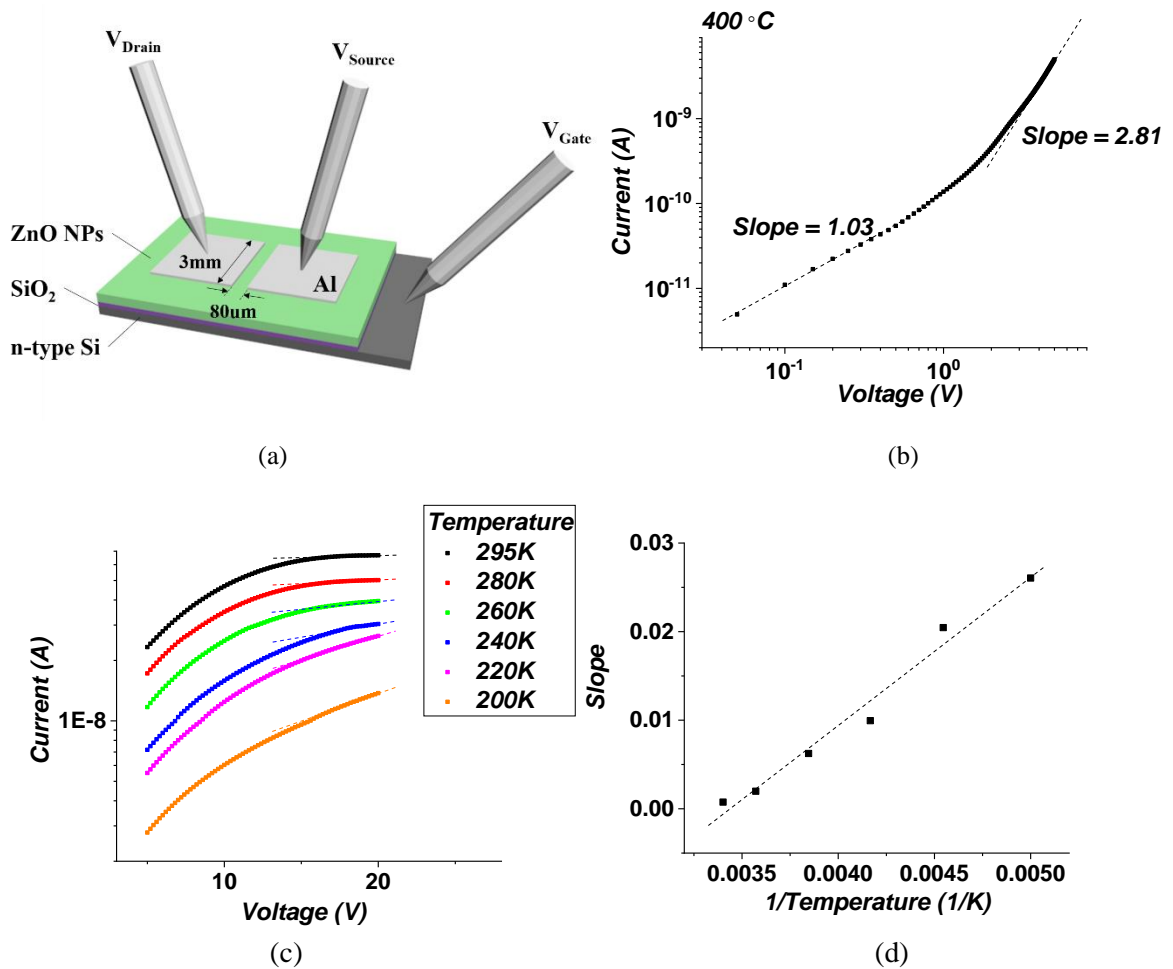


Figure 2.6 (a) Schematic structure of ZnO NPs sample. (b) The I-V characteristics of ZnO NPs. (c) The I-V characteristics of ZnO NPs at high DC voltage. (d) The slope of Log (I)~V at different temperature.

The I-V characteristics of ZnO NPs is illustrated in figure 2.6 (b) and it exhibits a linear slope (1.03) at low voltage (<0.5V), indicating that low-voltage conduction is Ohmic (slope of 1). Ohmic conduction is due to the movement of free electrons in the conduction band or holes in the valence band. The I-V relationship is always linear for Ohmic conduction and it is normally observed in the low-voltage region. As the voltage surpasses 1V, the slope reaches 2.81.

The conduction mechanism of ZnO NPs in air at room temperature is complicated since there are multiple factors in ZnO NPs such as traps, defects, impurities and adsorbed oxygen species etc. It has been reported that the electrical conduction in ZnO NPs is due to hopping [3]. Hopping conduction is a result of tunnelling effect from one trap site to another [99]. The current density (J) can be represented by the following equation:

$$J = A \exp\left(\frac{qdE}{kT} - \frac{E_a}{kT}\right) \quad (2.2)$$

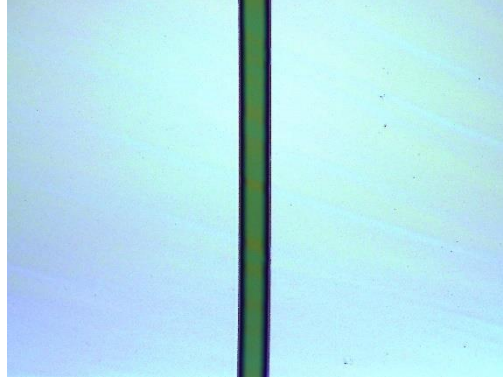
where d is the mean hopping distance, and A is a constant, which is dependent on the density of free electrons and the thermal vibration frequency of electrons at trap sites. E_a is the trap activation energy. The Log(I)~V relationship is plotted in figure 2.6 (c) and it shows a linear relationship at high voltages (>15V). This is consistent with the hopping conduction mechanism. It can be further confirmed by plotting the slope of Log(I)~V at different measuring temperatures, as is shown in figure 2.6 (d). According to equation 2.2, the slope of Log(I)~V is defined by $\frac{qd}{kT}$, which is proportional to 1/temperature. The plot in figure 2.6 (d) fits well to a linear relationship (dashed line) so it is consistent with the definition of hopping conduction. The slope in figure 2.6 (d) can be used to determine the mean hopping distance, which is calculated to be 0.144nm.

It can be concluded from this section that the electrical conduction mechanism of ZnO NPs at low DC voltage is Ohmic and it becomes hopping conduction at high voltage.

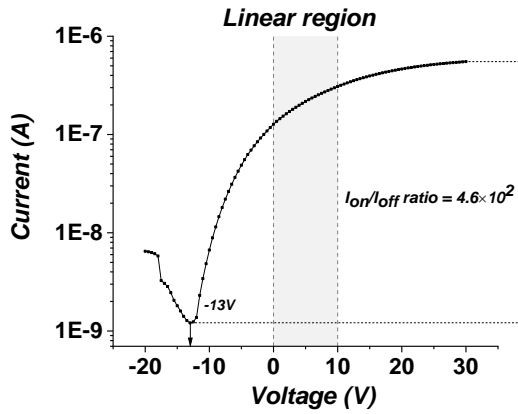
2.2.5 Field effect mobility

The charge carrier mobility is also an important indicator of electrical conduction as it determines the drift velocity of charge carriers under electric field and influences the electrical conductivity of ZnO NPs. Mobility is strongly affected by scattering such as ionized impurities (Coulomb's force) and lattice vibration (phonon exchange). Mobility can be determined by many techniques such as Hall effect measurement (Hall mobility) and field effect measurement (field effect mobility). The Hall mobility is accurate for pure materials like single crystals, so the field effect mobility was measured in this case.

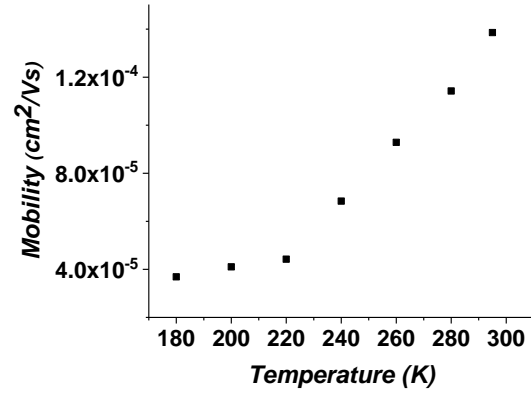
ZnO NPs-based field effect transistors (FET) were fabricated and the structure is depicted in figure 2.6 (a). The image of ZnO NPs-based FET is shown in figure 2.7 (a), taken under optical microscope.



(a)



(b)



(c)

Figure 2.7 (a) The image of ZnO NPs transistor under optical microscope. (b) The transfer characteristics of ZnO NPs transistor. (c) The field effect mobility under different measuring temperatures.

Figure 2.7 (b) shows the transfer function of ZnO NPs-based FET. It is clear that the threshold voltage is -13V and the on/off current ratio is about 460. The field effect mobility is calculated in the linear region (grey area), where I_{DS} and V_G have a linear relationship. The field effect mobility (μ) is determined by drain current (I_{DS}), drain voltage (V_{DS}), gate voltage (V_G), threshold voltage (V_{TH}), channel width (W) and length (L) by the following equation:

$$I_{DS} = \mu C_i \frac{W}{L} [(V_G - V_{TH})V_{DS} - \frac{V_{DS}^2}{2}] \quad (2.3)$$

where C_i is the capacitance per unit area of SiO_2 and it is calculated to be $1.16 \times 10^{-4} \text{ F/m}^2$. By choosing a point in the linear region, the charge carrier mobility is calculated as $2.95 \times 10^{-3} \text{ cm}^2/\text{Vs}$.

The temperature dependence of field effect mobility was also investigated by low-temperature I-V measurement. The measurement temperature was cooled down by liquid nitrogen. The result is shown in figure 2.7 (c) and it is clear that mobility increases as temperature rises. This indicates that the dominant scattering mechanism is ionized impurities or defects in the ZnO

NPs as electrons at higher temperature have larger thermal energy (speed) and their movement is less affected by the Coulomb scattering of ionized species.

2.2.6 Trap activation energy

ZnO NPs are rich in traps due to the existence of impurities, lattice defects and surface states etc. Trap states are extremely important to the electrical and optical properties of ZnO NPs since the density of free charge carriers and their lifetime are strongly affected by the trap states. This is particularly important for electro-optical applications because trap density and depth could heavily influence the responsivity and response time. For instance, the trap for majority carriers weakens the responsivity and lengthens the response time, while the trap for minority carriers enhances the responsivity.

The trap activation energy (E_a) is a measure of trap energy level in the bandgap. It can be extracted by the slope of Arrhenius plot ($1/T$, $\text{Log}(\sigma)$), according to equation (4) below:

$$\sigma = \sigma_0 \left(\exp\left(\frac{E_a}{kT}\right) \right) \quad (2.4)$$

where σ_0 is assumed to be constant and it is a function of charge carrier mobility and charge carrier density. Conductivity has an exponential relationship to the ratio of trap activation energy and measuring temperature (T) (k is the Boltzmann constant). The low-temperature measurement was conducted by Lake Shore cryogenic probe station with liquid nitrogen cooling. The minimum measurement temperature was 80K (slightly above the boiling point of liquid nitrogen at 78K).

The sample in figure 2.6 (a) was measured and the results are shown in figure 2.8 (a) and (b). The ohmic range was used to calculate the conductivity to avoid the contact effect. The I-V characteristics of ZnO NPs under different measuring temperatures (from 180K to 295K) is shown in figure 2.8 (a) and it is obvious that the current decreases as temperature drops because of decreased charge carrier mobility and charge carrier density. The conductivity at 1V was calculated based on the geometry of the sample. The Arrhenius plot is shown in figure 2.8 (b) and the trap activation energy is extracted by the slope. By converting the unit from Joule to eV, the trap activation energy is calculated to be 88meV.

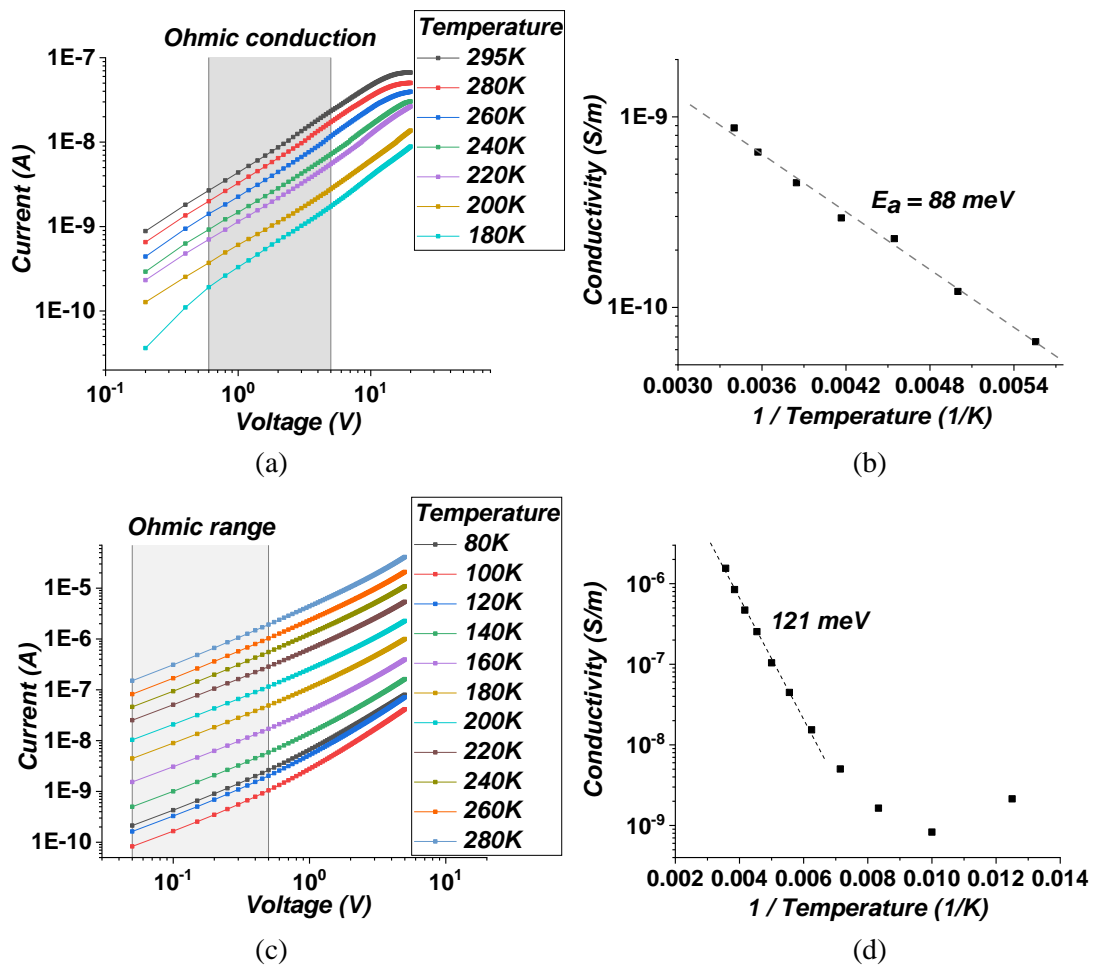


Figure 2.8 (a) The I-V characteristics of ZnO NPs under different measuring temperatures. (b) The Arrhenius plot and trap activation energy. The (c) I-V characteristics and (d) Arrhenius plot of ZnO NPs annealed for 5h.

A second ZnO NPs sample that was annealed in air for 5h was measured and the result is shown in figure 2.2.6 (c) and (d). The trap activation energy was calculated to be 121meV, which is larger than ZnO NPs annealed for 3h. This might be the result of defects created during the thermal annealing process.

One thing to be noted is that the I-V characteristics at even lower temperatures (down to 80K) was also measured in this case. The conductivity has an opposite trend at very low temperatures (below 120K). This is probably due to the enhanced electron conduction in the band formed by surface states. ZnO NPs have a much larger surface-to-volume ratio compared to other forms of ZnO, which introduces a large number of defects at the surface such as dangling bonds and recombined bonds. These surface states could form a conductive band within the bandgap, which becomes dominant at very low temperatures. As the temperature continues to decrease, the conductivity increases because lower temperature weakens the lattice vibration and the

scattering to electrons, thus strengthening the electrical conductivity. Another possible reason is that the Fermi level drops as the temperature decreases, which makes the band of surface states partially filled by electrons and results in a stronger conductivity. More research needs to be carried out to pinpoint the cause of enhanced electrical conductivity at lower measuring temperatures.

2.2.7 Dielectric properties

ZnO NPs are highly resistive and they exhibit dielectric behaviours under electric field. Bound charges in ZnO NPs are displaced from equilibrium positions by electric force and dipole moments are therefore formed. As a result, external electric energy is transferred to ZnO NPs by electrical polarization and the energy transfer process can be quantitatively described by the dielectric constant (ϵ). Dielectric constant is often used as a measure of material polarization under electric field and is the most important parameter for dielectric materials. The dielectric constant has a complex form:

$$\epsilon = \epsilon' - j\epsilon'' \quad (2.5)$$

The real part of dielectric constant (ϵ') represents the energy storing capability while the imaginary dielectric constant (ϵ'') indicates the energy dissipation due to energy-consuming processes such as relaxation and electrical conductivity.

There are several types of polarization mechanisms such as atomic polarization, ionic polarization, dipolar polarization and interface polarization etc. The dielectric behaviour is generally a combined effect of different polarization mechanisms, and different polarization mechanisms are effective at different frequency ranges because it takes a certain time to establish the polarization and they cannot respond to electric field at high frequencies. Therefore, dielectric constant is frequency-dependent, and it generally decreases at higher frequencies.

There are typically two types of polarization mechanisms in n-type semiconductor nanomaterials: ionic polarization due to positive oxygen vacancies and negative oxygen ions, and interface polarization due to interface defects such as dangling bonds and vacancy clusters [100]. Two polarization mechanisms are related to ZnO grain and nanoparticle boundary respectively. ZnO NPs are often represented by grain-boundary model as is illustrated in figure 2.9 (a), with ZnO grain surrounded by highly-resistive boundary [3], which is a result of adsorbed oxygen ions, surface defects and organic surfactants etc.

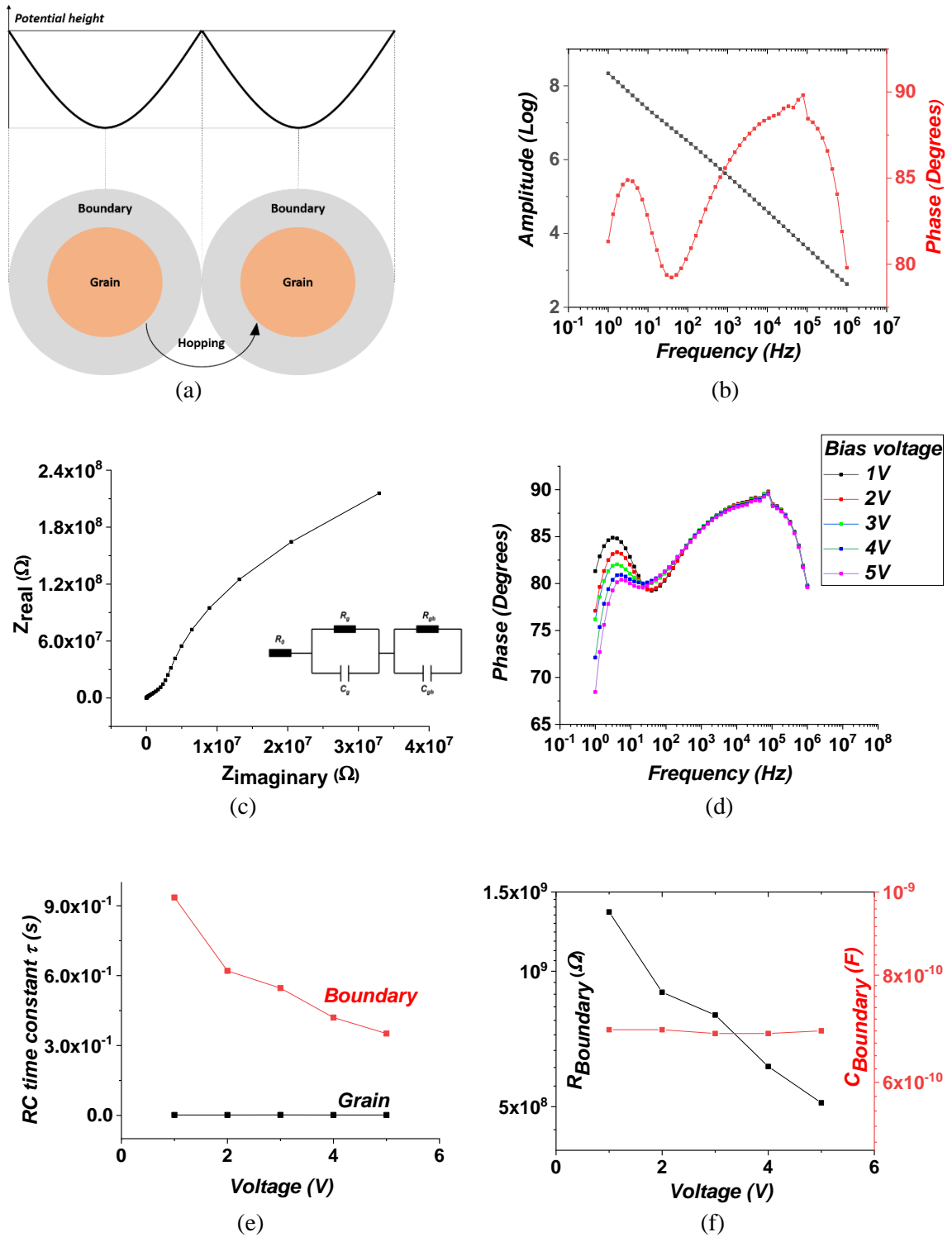


Figure 2.9 (a) The grain-boundary model and double-well potential model of ZnO NPs. The (b) Bode plot. (c) Nyquist plot. of ZnO NPs. (d) Phase under different DC bias voltages from 1V to 5V. (e) RC time constants of grain and boundary under different DC bias voltages. (f) Boundary resistance and capacitance under different DC bias voltages.

The dielectric properties of ZnO NPs was studied by impedance spectroscopy using Autolab PGSTAT302. A planar sample was used (same as the previous section). The Bode plot

(amplitude and phase of impedance against frequency) of ZnO NPs under 1V (DC bias) is shown in figure 2.9 (b). It is evident that there are two polarization mechanisms in ZnO NPs since there are two well-separated peaks in the phase plot (two peaks: one between $10^0\sim 10^1$ Hz and the other one between $10^4\sim 10^5$ Hz). There is a distortion on the second peak due to the transition of operation mode from high-speed mode to high-stability mode. Ideal dielectric materials have a phase of 90° while conductive dielectric materials have smaller phase as a result of dielectric loss.

The Nyquist plot (real impedance against imaginary impedance) is also plotted in figure 2.9 (c). It is clear that the Nyquist plot of ZnO NPs is composed by two semi-circles, indicating two polarization mechanisms as well. The Nyquist plot is useful to determine the equivalent circuit and RC time constant. RC time constant (τ) indicates the frequency dependence of different polarization mechanisms, which is equivalent to the relaxation time (the time it takes to restore from polarized state to thermal equilibrium state). RC time constant can be determined by the equivalent circuit model. According to the Nyquist plot, the equivalent circuit model of ZnO NPs is two parallel RC circuits (R_1C_1 and R_2C_2) in series with a resistor (R_0 , resistance associated with electrodes and cables), as is shown in the inset of figure 2.9 (c). Each parallel RC circuit represents a polarization mechanism and the RC time constant (in seconds) is calculated by the product of R and C in SI unit. The R and C values are determined by curve fitting, which is achieved by the built-in function of Autolab.

The measurement was also carried out under different DC bias voltages from 1V to 5V. The phase of Bode plot is illustrated in figure 2.9 (d) and it clearly shows that the low-frequency peak is suppressed at higher voltages while the other peak at high frequency is barely affected by the DC bias voltages. Lower phase indicates larger dielectric loss due to electrical conduction. This can be explained by the enhanced charge hopping at the boundary.

Moreover, the RC time constants for two polarization mechanisms are plotted against DC voltage in figure 2.9 (e). The polarization at the boundary (interface polarization) generally takes longer time to relax back because of the energy barriers. It is also noted that $\tau_{boundary}$ decreases (relax quicker) as voltage increases while τ_{grain} stays relatively constant at 1.88ms. The decrease of RC time constant at the boundary can be explained by the double-well potential model as is shown in figure 2.9 (a). DC bias voltage raises the potential height of one potential well and effectively decreases the potential barrier height. Higher DC voltage results in a lower barrier height and reduces the RC time constant.

Furthermore, the resistance and capacitance of the boundary are also plotted under different DC voltages in figure 2.9 (f). It is evident that the boundary resistance decreases at higher DC voltage due to the strengthening of charge hopping across the boundary between ZnO NPs.

Electrical hysteresis is a good way to visually represent the polarization of ZnO NPs. ZnO NPs are polarized in the opposite directions from the increasing voltage to the decreasing voltage. The electrical hysteresis of ZnO NPs was measured and the result is shown in figure 2.10 below. The current from 0V to 20V (I_{up}) is larger than that from 20V to 0V (I_{down}). This is the result of polarization because ZnO NPs are polarized as the voltage increases while the polarization remains when the voltage decreases (opposite direction), opposing the decreasing voltage. The key factor for electrical hysteresis is that the RC time constant of ZnO NPs is longer than the measuring interval (inverse of sampling frequency) so that the polarization state remains as the voltage decreases.

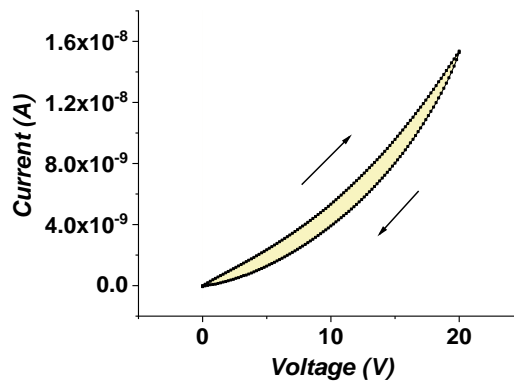


Figure 2.10 Electrical hysteresis of ZnO NPs.

Electrical polarization is a good measure of polarization density of ZnO NPs. It can be quantified by calculating the ratio between the area enclosed by two current curves (yellow area) and the area under the increasing current (with X axis). This is discussed in the later sections.

2.2.8 Optical absorption

Optical absorption is significant for photosensitive materials since it provides information on the ‘active’ wavelength and the status of energy band. Optical absorption spectroscopy is often used to characterize the optical absorbance of light with different frequencies (wavelengths), and the energy bandgap (E_g) can be therefore calculated. The optical absorption rises dramatically when the photon energy ($h\nu$) of the incident light reaches the bandgap of the material.

$$h\nu \geq E_g \quad (2.6)$$

where ν is the frequency of light.

The optical absorption of ZnO NPs was studied using UV-Visible spectroscopy in the wavelength range from 350nm to 1000nm. The measurement was conducted in the transmission mode and ZnO NPs were prepared on a transparent glass substrate (spin coating, followed by thermal annealing in air at 400°C for 3h). The absorption spectrum of the glass substrate was measured firstly as a reference, after the dark environment measurement. Then ZnO NPs thin film was measured, as is shown in figure 2.11 below.

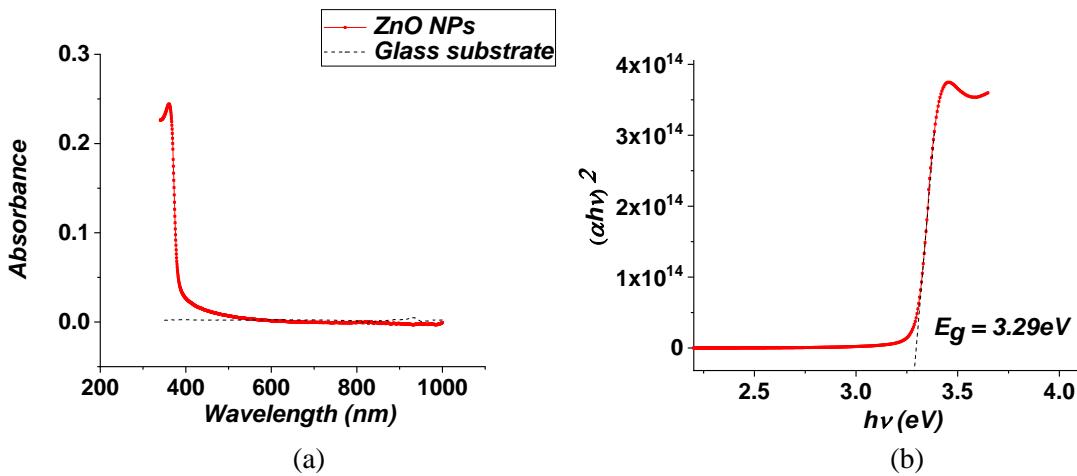


Figure 2.11 (a) UV-Vis spectroscopy of ZnO NPs. (b) The Tauc plot and energy bandgap.

The result in figure 2.11 (a) shows that the absorbance increases drastically when the wavelength is below 400nm while there is little absorbance above 400nm. This indicates the electronic transition from valence band to conduction band and the photon energy corresponds to the energy bandgap. In addition, the UV-Vis spectroscopy demonstrates that ZnO NPs are particularly useful for UV-sensitive applications and they are not sensitive to light in the visible range (400nm~700nm). ZnO NPs have a direct bandgap, which makes the recombination of photogenerated charge carriers more efficient.

The bandgap (E_g) is determined by Tauc method based on the following equation:

$$(\alpha h\nu)^{\frac{1}{n}} = K(h\nu - E_g) \quad (2.7)$$

where α is the absorption coefficient and $h\nu$ is the photon energy. K is a constant and n is dependent on the type of bandgap. The bandgap can be determined by the intersection of the linear part of $(\alpha h\nu)^2$ against $h\nu$, as is shown in figure 2.11 (b).

The absorption coefficient is calculated by absorbance (A) according to:

$$\alpha = A \times \ln(10) / d \quad (2.8)$$

where d is the thickness of ZnO NPs film. In the case of direct bandgap of ZnO, n is $\frac{1}{2}$ [101]. The energy bandgap of ZnO NPs is determined to be 3.29eV.

2.2.9 UV response

It has been concluded by UV-Vis spectroscopy in the previous section that ZnO NPs are sensitive to UV (below 400nm) so ZnO NPs are suitable for UV-sensitive applications such as UV detectors and UV-writing optically addressed spatial light modulators (OASLMs). The absorbed UV excites electrons from the valence band to the conduction band, creating free charge carriers and enhancing the electrical conductivity. Therefore, ZnO NPs is a kind of photoconductor. The UV response of ZnO NPs was carried out on a planar sample and the UV light was incident from the top. The result is shown below in figure 2.12 (a).

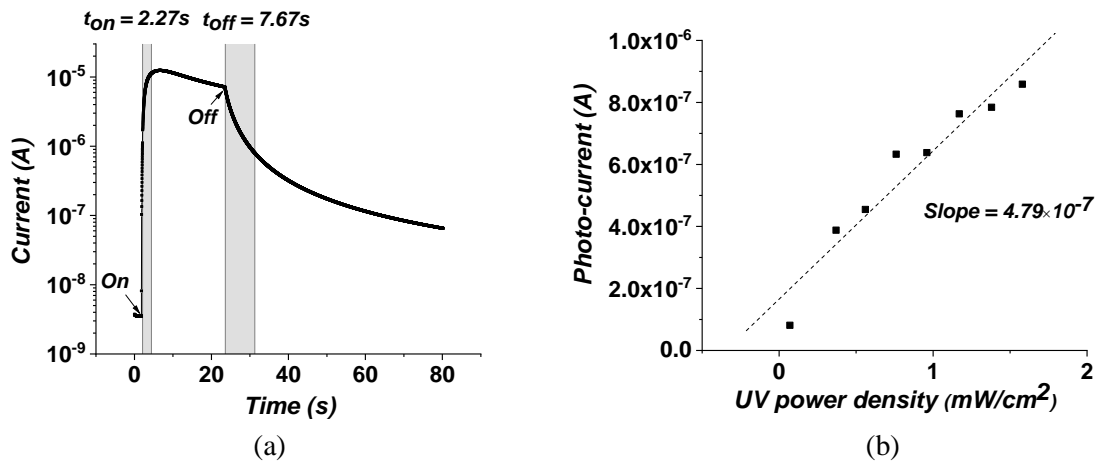


Figure 2.12 (a) UV response of ZnO NPs. (b) External quantum efficiency (EQE) of ZnO NPs.

The wavelength of the UV light is 365nm and the UV power was controlled by a current source. The power density was also measured with a power meter. Figure 2.12 (a) depicts that the current increases drastically (by an order of more than 3 in 2.27s) once the light is on. The on time is calculated by the time that current increases from 10% to 90% of the step current height. The off time is 7.67s, more than 3 times of the rise time. The fall time is longer than the rise time because ZnO NPs contain a large amount of trap states and part of photogenerated electrons are trapped in the trap states. The trapped electrons cannot recombine with holes and they have to be thermally excited to the conduction band before recombination. The time for thermal excitation is normally long and this extends the fall time. In addition, the existence of electron traps reduces the responsivity (maximum photocurrent) because some electrons are

attracted by the trap states (trap filling) and trapped electrons do not contribute to the photoconductivity.

External quantum efficiency (EQE) is also an important parameter to measure the generation of photoexcited electron. EQE is defined as the ratio between the number of photo-generated free charge carriers and the number of incident photons. It can be determined by the relationship between the photocurrent (I_{photo}) and the UV power density (P). The $I_{photo} \sim P$ relationship for ZnO NPs is plotted in figure 2.12 (b). The photocurrent (I_{photo}) can be expressed by elementary charge (q), irradiated area (A), external quantum efficiency (η) and photon energy ($h\nu$) based on the following equation:

$$I_{photo} = q\eta \frac{PA}{h\nu} \quad (2.9)$$

By extracting the slope of $I_{photo} \sim P$ plot, EQE for ZnO NPs is 2.38×10^{-7} . The EQE for ZnO NPs is low, which also indicates that a large portion of photogenerated charge carriers are trapped.

2.3 Annealing Effect on ZnO NP Thin Films

Annealing is an important post-processing method. It has been reported that annealing affects the size and morphology of nanoparticles, agglomeration, crystallinity, defect density and energy bandgap etc. [101]–[107] This section is concentrating on the effect of annealing on ZnO NPs, regarding the electrical, dielectric and optical properties. High-temperature annealing was performed in air on ZnO NPs by furnace.

2.3.1 Lattice structure

The lattice structure of ZnO NPs after annealing was studied by XRD and the result is shown below in figure 2.13. The characteristic XRD peaks of ZnO NPs annealed at 200°C and 500°C show that thermal annealing broadens the characteristic peaks. This is an indication of increased particle size. On the other hand, the height of characteristic peaks increases as temperature raises due to a better crystallinity of ZnO NPs. Therefore, high-temperature annealing increases the particles size and the crystallinity.

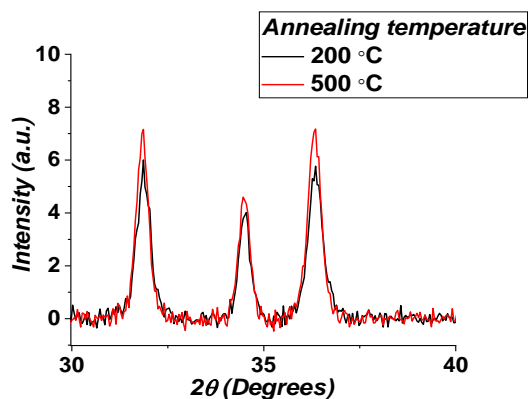


Figure 2.13 XRD pattern of ZnO NPs annealed at 200°C and 500°C.

2.3.2 Electrical properties

Electrical properties of ZnO NPs are strongly affected by thermal annealing. High-temperature annealing could evaporate organic surfactants surrounding the ZnO NPs, improve the crystallinity of ZnO NPs and decrease the trap activation energy. As a result, the electrical conductivity increases after thermal annealing.

The I-V measurement was carried out for ZnO NPs annealed at 300°C, 400°C, 500°C and 600°C in air for 3hs. The samples were also measured at lower temperatures and the results are shown in figure 2.14 (a). It is evident that higher annealing temperature results in a greater conductivity, which is consistent with theoretical expectation. On the other hand, the trap activation energy was also extracted for different annealing temperatures. It is evident that higher annealing temperature leads to shallower trap states from 113meV to 54meV. The shallower trap states could be a result of decreased impurities and defects (thermal annealing in air helps to diminish oxygen vacancies). ZnO NPs annealed at a longer annealing time of 5h were also measured and the result is shown in figure 2.14 (b). By comparing the trap activation energy of ZnO NPs annealed at the same temperature, it is noted that deeper trap states are created with longer annealing time (from 88meV to 121meV at 400°C, 76meV to 89meV at 500°C, and 54meV to 60meV at 600°C). This indicates that stronger thermal annealing could generate new trap states. These trap states are possibly caused by defects because defects could be generated by thermal annealing or mechanical rubbing. This can be further confirmed by the trap state at 0.235eV for ZnO NPs annealed at 600°C for 5h.

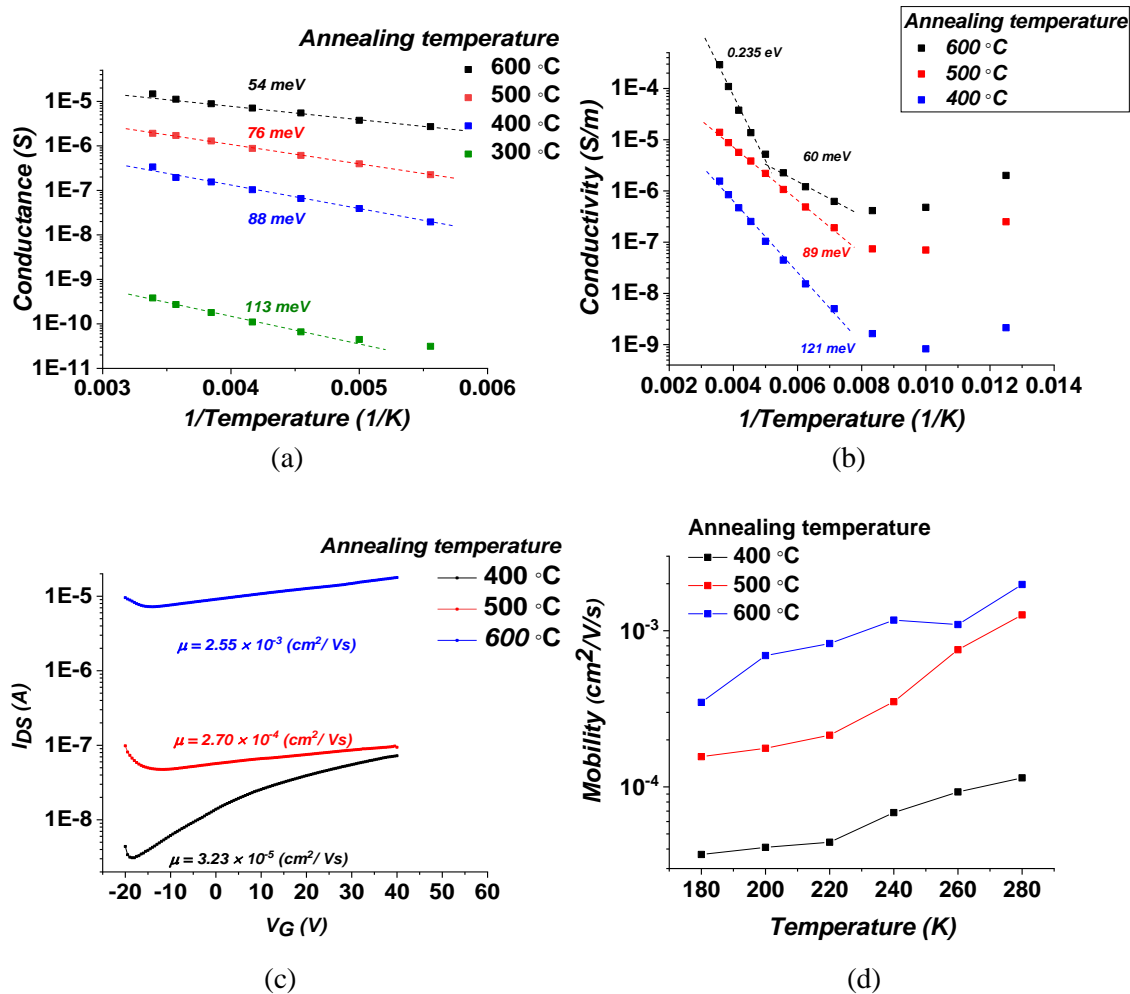


Figure 2.14 Arrhenius plot of ZnO NPs annealed at different temperatures for (a) 3h and (b) 5h in air. Annealing effect on (d) Transfer function and (e) Charge carrier mobility.

The transfer function of ZnO NPs-based FET was also measured, and the charge carrier mobility was then calculated, as shown in figure 2.14 (c). It is evident that higher annealing temperature results in a larger charge carrier mobility. This can be explained by less scattering from impurities and trap states. The transfer function also shows that the on and off current ratio decreases with higher annealing temperature. Figure 2.14 (d) shows the field effect mobility at lower temperatures. The mobility exhibits an increasing trend with increasing measuring temperatures for all the ZnO NPs, which confirms that the mobility is mainly affected by ionic scattering.

2.3.3 Dielectric properties

The annealing effect on dielectric properties was investigated by impedance spectroscopy. Similarly, the RC time constants for gain and boundary are extracted by fitting the Nyquist plot. The RC time constants against annealing temperature are plotted in figure 2.15 (a).

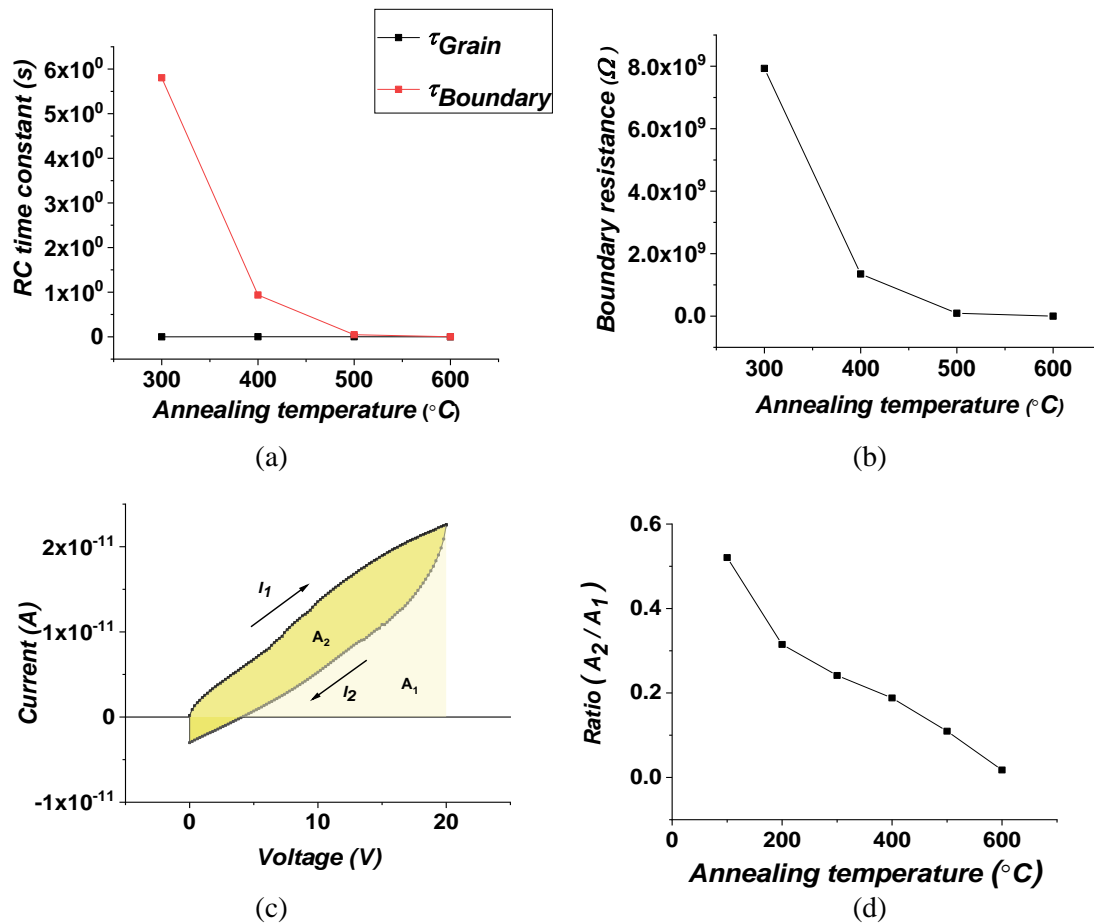


Figure 2.15 (a) RC time constant and (b) Boundary resistance of ZnO NPs annealed at different temperatures. (c) Electrical hysteresis for ZnO NPs. (d) Hysteresis ratio (A_2/A_1) against different temperatures.

It is clearly shown that the RC time constant of gain stays relatively constant. However, thermal annealing has a significant effect on the boundary. RC time constant decreases as annealing temperature rises, indicating a less amount of impurities and defects at the boundary or interface. Moreover, the boundary resistance is also plotted against annealing temperature in figure 2.15 (b) and it clearly demonstrates an improved conductivity at higher annealing temperatures.

The electrical hysteresis was used to reflect the effect of thermal annealing. As was mentioned previously, the hysteresis was quantified by the ratio of area A_1 and A_2 , where A_1 is the area enclosed by I_1 and X axis and A_2 is the area between I_1 and I_2 , as is shown in figure 2.15 (c). The hysteresis ratio against annealing temperature is plotted in figure 2.15 (d) and it is obvious that the ratio decreases as annealing temperature increases. This is because of the reduced RC time constant, which makes ZnO NPs relax quicker to the equilibrium state and respond faster to the change of electrical voltage.

2.3.4 Optical properties

The annealing effect on the optical properties of ZnO NPs is of great importance since this helps to locate the optimum annealing temperature for optical applications. The photogenerated (on) current and dark (off) current of ZnO NPs annealed at different temperatures are plotted in figure 2.16 (a). Both on and off current increase as annealing temperature raises. The current on/off ratio is further plotted in figure 2.16 (b). It is evident that the maximum on/off current ratio is achieved at 400°C (the ratio is about 4000), which means that the annealing temperature of 400°C is the best in terms of responsivity.

The fall time is the time duration from 90% to 10% of the step height in current and it is also plotted against annealing temperature in figure 2.16 (c). It is observed that the temperature range of 300°C ~ 400°C is preferred in order to obtain a quick fall time. The fall time is determined by recombination. On one hand, higher annealing temperature results in lower trap activation energy, which enables easier thermal activation and hence faster recombination. On the other hand, the diminish of impurities or deep-level states by higher annealing temperature decreases the amount of recombination centres and prolongs the fall time. Therefore, the fall time decreases first and then increases as the annealing temperature rises.

The UV-Vis spectroscopy was measured and the Tauc plot is shown in figure 2.16 (d). It clearly demonstrates that the energy bandgap (intersection point with X axis) is relatively constant regardless of the annealing temperature. This concludes that thermal annealing mainly affects the energy states within the bandgap while it has little effect on the bandgap.

Figure 2.16 (e) shows the relationship between photocurrent and UV power density for ZnO NPs annealed from 200°C to 600°C. The external quantum efficiency of ZnO NPs is extracted from the slope and plotted in figure 2.16 (f). It is evident that the quantum efficiency increases at higher annealing temperature, indicating a larger amount of free charge carriers are generated as a result of shallower trap states.

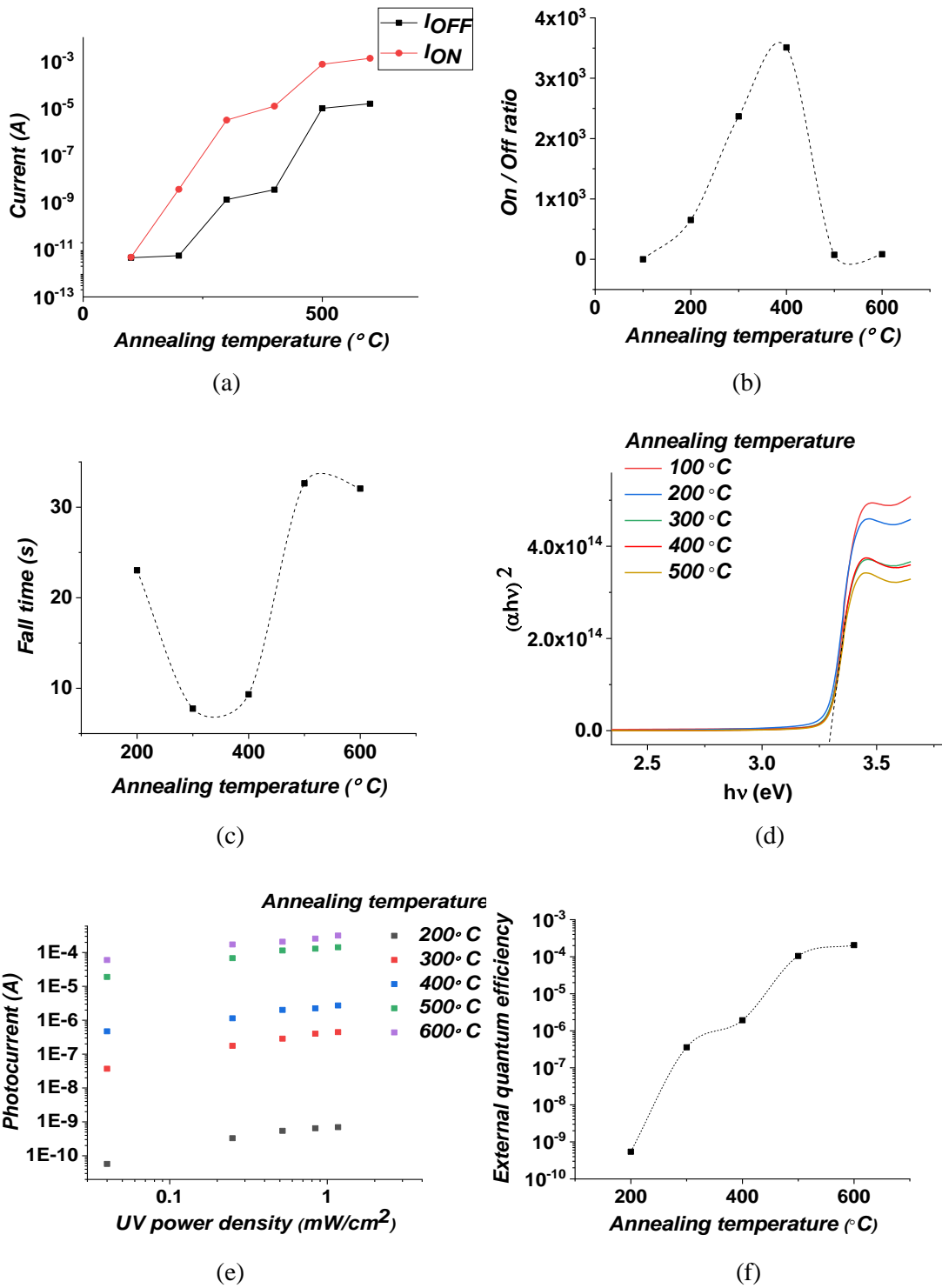


Figure 2.16 The (a) On and off current, (b) On/off current ratio, (c) Fall time, (d) Energy bandgap, (e) Photocurrent against UV power density and (f) External quantum efficiency of ZnO NPs annealed at different temperatures.

2.4 Oxygen Plasma Effect on ZnO NP Thin Films

Oxygen plasma is a mixture of various oxygen species such as ionized oxygen (O_2^+ , O_2^- , O^+ , O^-), oxygen atoms, oxygen molecules and ozone etc., and it was used to prove the existence of organic surfactant in the previous section. Moreover, oxygen plasma is an effective method to reduce the amount of oxygen vacancies, which equivalently reduces the donor density and increases the resistivity of ZnO NPs. The I-V characteristics of ZnO NPs annealed at 400°C was shown in 2.4 (b), indicating that ZnO NPs after oxygen plasma treatment have a lower conductivity. Same measurement was carried out for ZnO NPs annealed at 600°C and the I-V characteristics is shown below in figure 2.17 (a). It is evident that plasma reduces electrical conductivity by filling the oxygen vacancies.

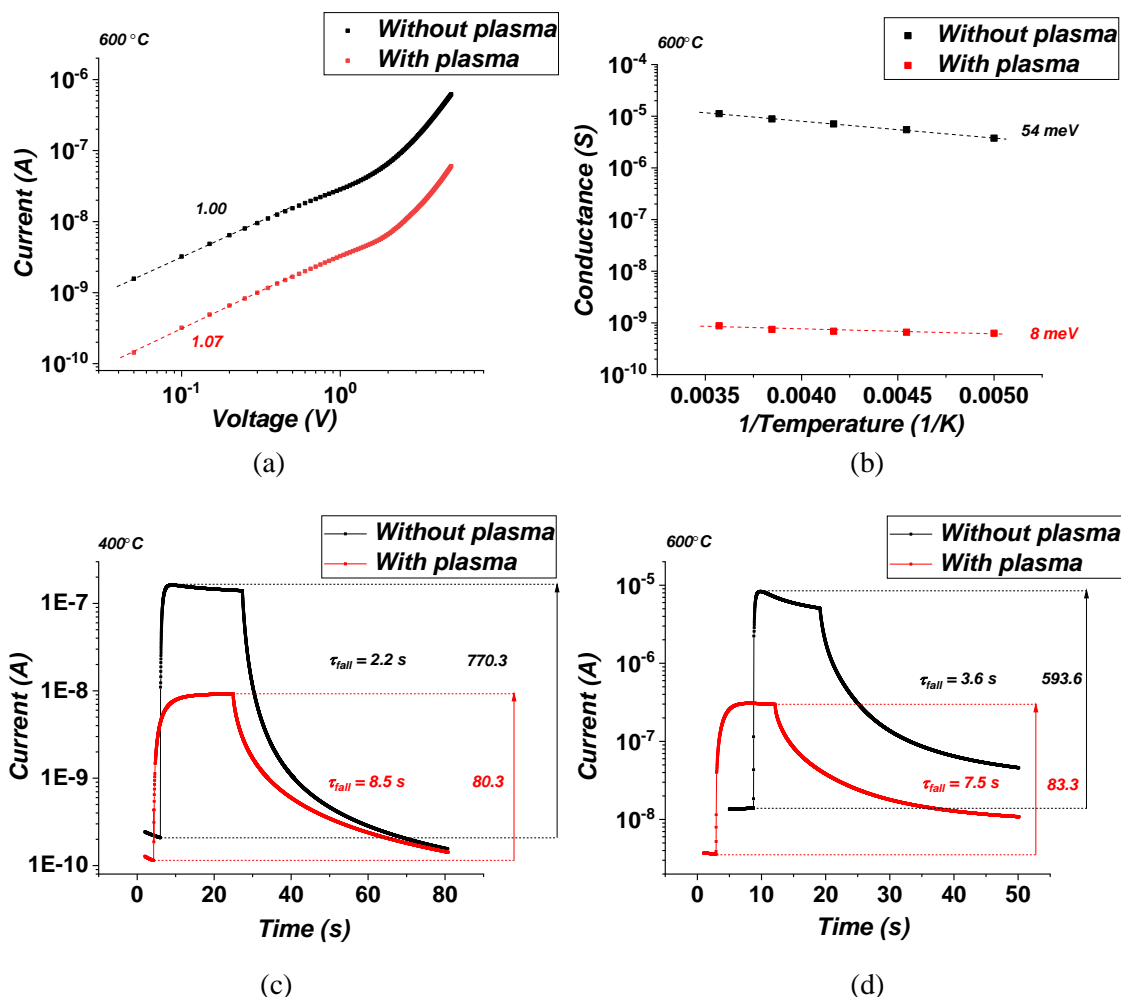


Figure 2.17 The (a) I-V characteristics and (b) Trap activation energy of ZnO NPs annealed at 600°C with and without oxygen plasma treatment. UV response of ZnO NPs annealed at (c) 400°C and (d) 600°C.

In addition, the trap activation energy was also determined for ZnO NPs annealed at 600°C, as is shown in figure 2.17 (b) below. It is straightforward that ZnO NPs after plasma treatment have a smaller activation energy (8meV) than ZnO NPs without plasma treatment (54meV). The trap activation energy of 8meV is smaller than the room-temperature thermal energy (25.7meV) so these shallow traps are not effective at room temperature.

The UV response was also investigated. Figure 2.17 (c) and (d) shows the on/off current ratio and fall time (off time) of ZnO NPs annealed at 400°C and 600°C respectively with the same UV power. It is clear that ZnO NPs without oxygen plasma treatment have a larger on/off ratio in both cases (9.6 times and 6.8 times larger for 400°C and 600°C respectively). This is because the photogenerated electrons are not recombined due to the existence of trap states for non-treated ZnO NPs. Therefore, a large number of free charge carriers are trapped and re-excited to the conduction band, leading to a larger photocurrent. On the contrary, photogenerated free charge carriers of treated ZnO NPs are recombined directly, leading to a larger recombination rate and smaller current.

Figure 2.17 (c) and (d) also illustrates the falling time of ZnO NPs, which shows that ZnO NPs without oxygen plasma treatment have a shorter falling time in both cases (26% and 48% of the treated ZnO NPs annealed at 400°C and 600°C respectively). This is because there is a large number of recombination centres in non-treated ZnO NPs such as organic surfactants (impurities) and deep states (defects). Recombination centres are effectively eliminated after oxygen plasma treatment, leading to a longer falling time.

One thing to be noted is the on current after it reaches its maximum. The rising current of non-treated ZnO NPs encountered a decrease while the rising current for treated ZnO NPs gradually saturates. This is due to the charge trapping effect. Trapped charge carriers take a relatively long time to be thermally re-excited to the conduction band, before they are recombined. Therefore, the slight decrease of on current reflects the increased recombination rate as more trapped charge carriers are re-excited. The on current of non-treated ZnO NPs shows a gradual saturation, which is a typical behaviour of photocurrent without apparent trapping effect.

Chapter 3 The Characterization and Optimization of ZnO NPs-based OASLMs

ZnO NPs are particularly promising for optical applications since they are sensitive to UV light and are barely sensitive to the visible light (380nm~740nm). The focus of this chapter is mainly on the application of optically addressed spatial light modulators (OASLMs) since ZnO NP-based OASLM can provide a considerably high spatial resolution (825 lp/mm), which surpasses all the past record [108]. This is particularly valuable for large-size and large-viewing angle holographic displays. In addition, OASLMs have many advantages over electrically addressed SLMs such as no pixel limit, no deadspace between pixels, easy fabrication and large device size etc. However, ZnO NP-based OASLMs are also limited by the low diffraction efficiency and long response time, which is a significant challenge for dynamic holographic displays. Therefore, the optimization of ZnO NP-based OASLM is particularly valuable.

This chapter starts with the simulation of OASLMs, from which the resolution limit by LC layer and ZnO NP layer was demonstrated. The effect of LC parameters (elastic constants, dielectric constants and thickness etc.) on phase profile was investigated so that a rule of thumb was established to achieve high resolution. Lateral diffusion in ZnO NP layer was also demonstrated by COMSOL. Then the characterization and optimization of OASLMs were presented. The diffraction efficiency was optimized by investigating the driving signal parameters (shape, amplitude and frequency). In the meanwhile, the fall time of OASLMs was shortened by increasing the annealing temperature of ZnO NPs, introducing a dielectric SiO₂ layer between LC and ZnO NP, and replacing the ZnO NP photoconductor with ZnO NP-PEDOT:PSS heterojunction photodiode.

3.1 Simulations of LCs in OASLMs

A typical structure of OASLM is shown in figure 3.1 below. A LC layer is sandwiched between a ZnO NP layer and an alignment layer. Spherical spacers (not shown) are used to separate the substrates. LCs layer is highly influential to the performance of OASLMs. For instance, the response time of OASLMs is partly dependent on the RC time constant of LCs. Moreover, the resolution of OASLMs is limited by electrical fringing field in LCs layer [3], which is further dependent on the thickness and elastic constants LCs. This section investigates the effect of LCs on the resolution of OASLMs by computer simulation.

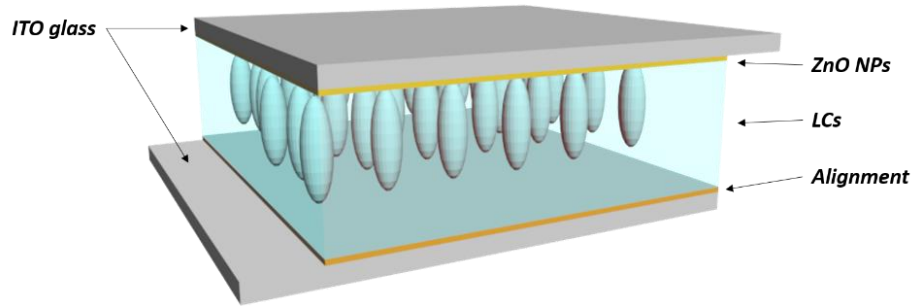


Figure 3.1 The typical structure of OASLMs.

3.1.1 Electric fringing field in LCs

Resolution of OASLMs is represented by the molecular orientation of LCs. The orientation of LCs can be mathematically determined by continuum elastic theory and this was carried out by computer simulations. The simulation was conducted using LCD Master and the LCs arrangement of the cross-section in the middle (plane $x=0$) is shown below in figure 3.2. Figure 3.2 (a) clearly shows the molecular orientation of LCs (nails) and the phase retardation (red line) in plane $x=0$. The incident light is linearly polarized (polarization direction is parallel to the director of LCs) and has a wavelength of 550nm. Figure 3.2 (b) illustrates the potential distribution (equal-potential lines and colormap) and electric force (black arrows) inside LCs. The resolution of OASLMs can be indicated by phase retardation profile and it is evident that electric fringing field is degrading the resolution. The electric fringing field normally exists at the edge (fringe) as a result of boundary conditions. Extended electric field also results in the orientation of LCs and an enlarged effective area (decreased resolution).

One thing to be noted is that there is a peak in the middle of retardation profile. This is caused by the symmetric electric field distribution in the middle, as is shown in figure 3.2 (c). LCs always orient themselves to align with the electric field (yellow arrow). Electric forces are also symmetric on the two sides of axis of symmetry, which means LCs on the two sides rotate in the opposite directions because they are pre-tilted at 3° . On the other hand, elastic force opposes the movement of LCs so there is a competition between elastic force (red arrows) and electric force (black arrows). The elastic force near the axis of symmetry is larger than that away from the middle so LCs tend to remain original orientation (do not rotate) in the middle unless electric force is large enough to surpass elastic force. As a result, there is a minimum peak for phase retardation near the axis of symmetry.

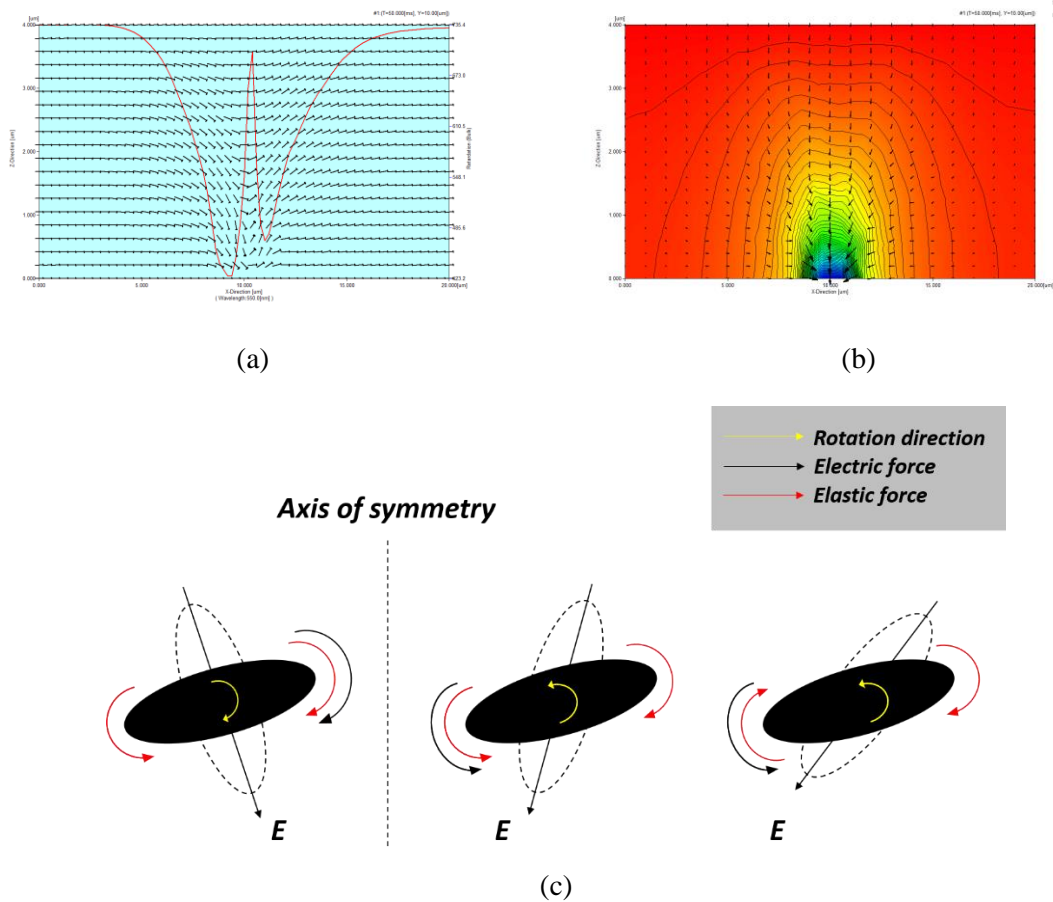


Figure 3.2 The simulated results for (a) Director (nail) and phase retardation profile (red line), (b) Electric force (arrow) and electric potential (colormap) of the cross-section. (c) Force analysis for LCs in the middle.

Another important fact is that nematic LCs are anisotropic, so the electric field is different from that in isotropic media. Molecules of LCs orient themselves under electric field due to induced dipole moments and LCs in turn influence the distribution of electric field. Therefore, it is a dynamically interactive process between LCs and electric field.

A simple model is built up using nematic LCs (5CB, $\epsilon_{\perp} = 6.9$ and $\epsilon_{\parallel} = 17.9$, $k_1 = 6.37$, $k_2 = 3.81$ and $k_3 = 8.60$), as is shown in figure 3.3 (a). LCs are sandwiched by ITO electrodes on both sides and ZnO NPs are coated on the bottom. LCs are pre-tilted at 3° on both sides with parallel alignment configuration. A 3D model is established within the software, as is shown in figure 3.3 (b). The area of the top and bottom sides is $20\mu\text{m} \times 20\mu\text{m}$ and LCs layer has a thickness of $4\mu\text{m}$. Illuminated area by the write light ($1\mu\text{m} \times 1\mu\text{m}$) is located in the centre (depicted with a red square in 3D model). The intensity profile of the write light is assumed to be square, providing a step change in conductivity of ZnO NPs. Furthermore, in order to simplify the calculation, it is assumed that the illuminated ZnO NPs are grounded (0V) while the un-

illuminated ZnO NPs are insulating (large resistance). Moreover, the interface effect between LCs and ZnO NPs is also neglected. A DC voltage of 5V is applied across LCs.

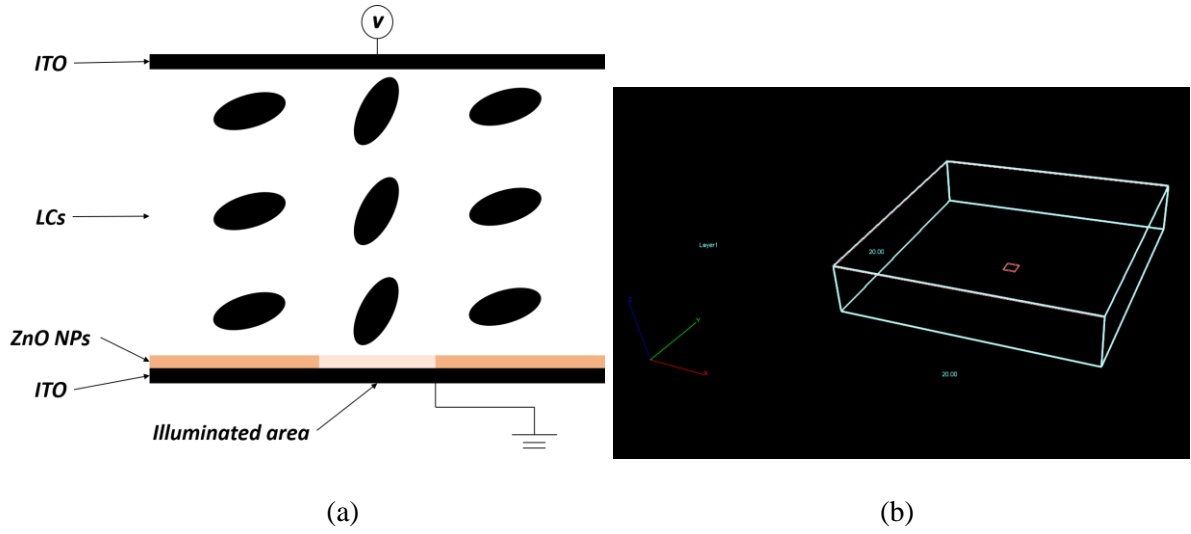


Figure 3.3 (a) Model of LCs cell. (b) 3D model in LCD Master.

In order to see the effect of anisotropy in dielectric constant, isotropic media is used as a comparison. The magnitude and angle of electric force at $z=2\mu\text{m}$ is plotted, as is shown in figure 3.4 (a) and (b) below.

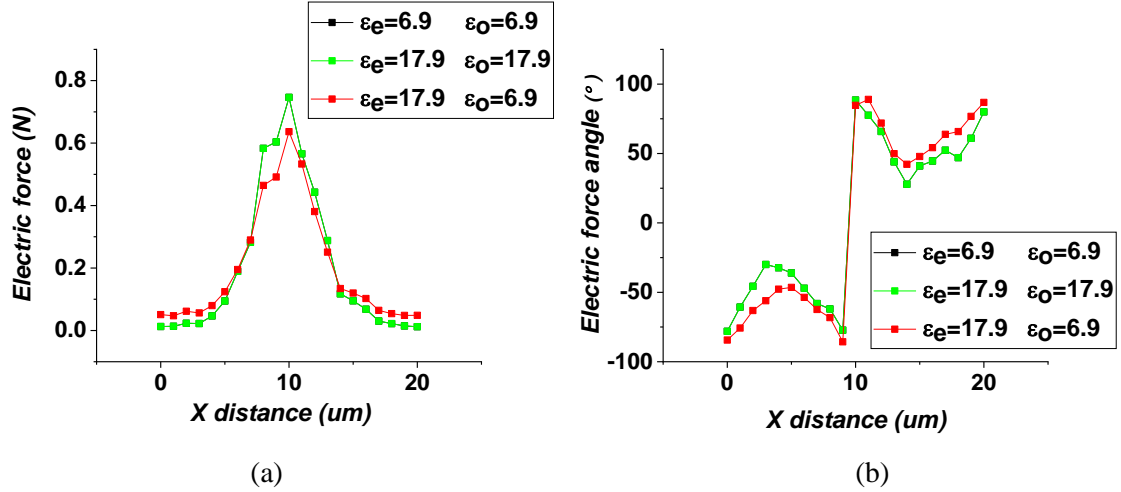


Figure 3.4 The (a) magnitude and (b) angle of electric force in LCs.

It is clearly shown that the amplitude and angle of electric force in two isotropic media with $\epsilon_{\perp} = \epsilon_{\parallel} = 17.9$ and $\epsilon_{\perp} = \epsilon_{\parallel} = 6.9$ are exactly identical (overlap). However, electric force is different both in amplitude and angle in anisotropic LCs due to the interaction between LCs and electric field. The interaction is based on the Coulomb force, which is defined by:

$$F = \frac{1}{4\pi\epsilon_0\epsilon_r} \frac{q_1q_2}{r^2} \quad (3.1)$$

where q_1 and q_2 are the charges with a distance of r . ϵ_0 and ϵ_r are the absolute and relative permittivity (dielectric constant) LCs. Electric force at a certain point is equivalent to the superposition of Coulomb forces from all directions. The dielectric anisotropy of LCs molecules results in macroscopic non-uniformity of dielectric constant within LCs, leading to different electric field distribution in LCs.

The electric potential at $z=2\mu\text{m}$ is also plotted in figure 3.5 below. This is consistent with electric force distribution since electric field (E) is the rate of change in electric potential (V).

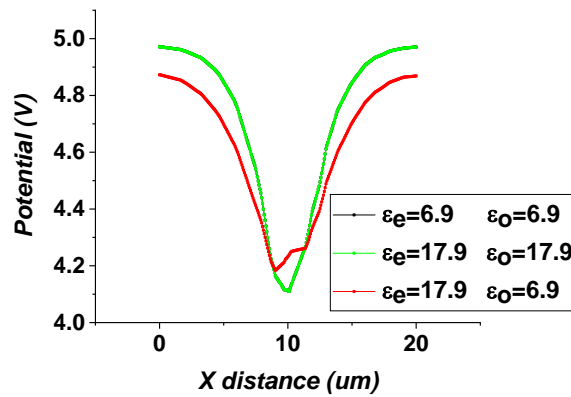


Figure 3.5 Electric potential distribution in LCs.

Moreover, the potential distribution is symmetric in isotropic media whereas it is asymmetric in LCs. This is related to the molecular orientation of LCs and this is discussed in the following section.

3.1.2 Effect of driving voltage and thickness

LCs are voltage-driven so the driving voltage across LCs affects the resolution of OASLMs. A DC voltage was used in the model and the result is shown in figure 3.6 below. It is clear that as the voltage raises from 1V to 5V, resolution degrades (phase retardation profile becomes wider) due to a stronger electrical fringing field. In the meanwhile, modulation depth also increases at the same position. Figure 3.6 (b) shows the phase retardation near the axis of symmetry under increasing driving voltages and it exhibits a decreasing trend as electric force becomes more and more dominant over elastic force with increasing voltage. This is consistent with previous analysis.

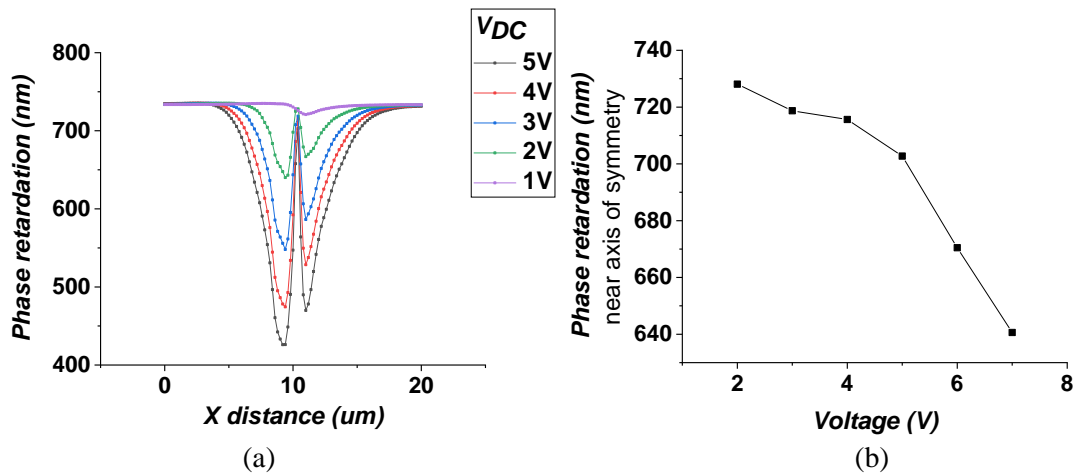


Figure 3.6 (a) The phase retardation profile under different driving voltages. (b) The distortion at the axis of symmetry under different voltages.

The thickness of LCs layer is also affecting the resolution of OASLMs, as is shown in figure 3.7 below. It is obvious that larger thickness results in a larger affected area as a result of electric fringing field. Simulation was carried out with LCs thickness from 1μm to 5μm and the resolution of OASLMs is defined here by the width of phase retardation profile at 90% of its maximum, as is shown in figure 3.7 (a). The resolution (phase width) and maximum modulation depth are shown in figure 3.7 (b) at different LCs thickness. The trend shows that larger thickness provides larger modulation depth though the resolution also degrades.

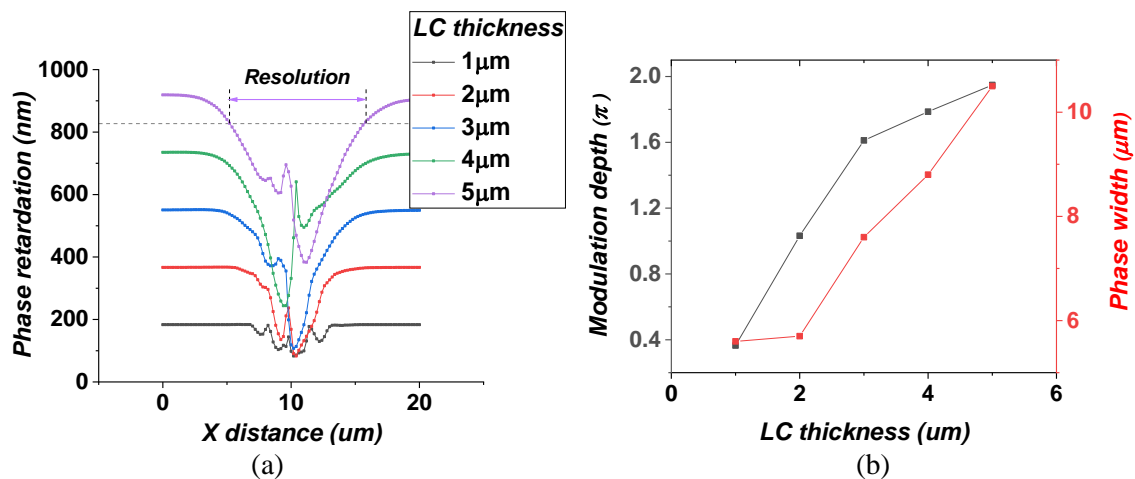


Figure 3.7 (a) Phase retardation profile of various LCs thickness. (b) The modulation depth and phase width at different LCs thickness.

In summary, the resolution of OASLMs is strongly affected by the driving voltage and LCs thickness. It is preferred to use lowest driving voltage and thinnest LCs layer when designing OASLMs, however these also lead to a compromised phase modulation depth. Therefore, the

optimum design of OASLMs should be different for different applications depending on the requirement.

3.1.3 Effect of elastic constants and dielectric constants

It has been introduced in chapter 1 that elastic constants are intrinsic parameters of LCs that determine the elastic force. Therefore, elastic constants are extremely important to the orientation of LCs since elastic force always resists electric force. Based on the definitions of elastic constants for splay, twist and bend (k_1 , k_2 and k_3 respectively), it is clear that k_1 and k_3 are dominant for LCs with parallel-alignment configuration or electrically controlled birefringence (ECB) configuration.

In order to determine the effect of k_1 and k_3 , LCs with various values of k_1 and k_3 are simulated. The simulation starts with small value so that LCs are mainly affected by one elastic constant only. It is found out that the phase retardation profile changes little when k_1 and k_3 are between 0.01 and 0.1 so $k_1 = 0.01$ and $k_3 = 0.01$ are chosen as the starting values.

Firstly, the effect of k_1 (splay) is investigated by keeping k_3 constant (0.01) and increasing k_1 from 0.01 to 9. The results are shown below in figure 3.8:

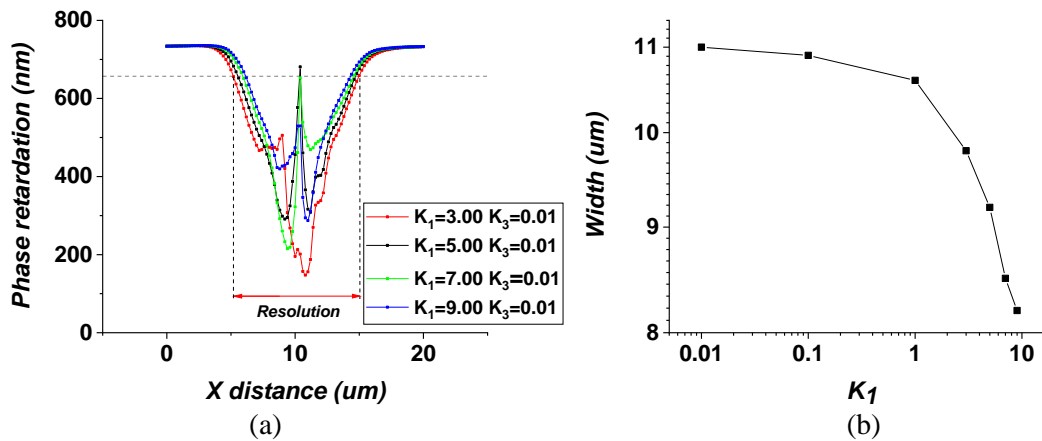


Figure 3.8 (a) Phase retardation profile for different k_1 values. (b) The phase width (resolution) for different k_1 values.

It is evident from figure 3.8 (b) that the resolution decreases little when k_1 is below 0.1 and it rapidly drops when k_1 is above 1. Therefore, the resolution of OASLMs is strongly affected by k_1 and LCs with larger k_1 have better performance in resolution (narrower width). This is because higher k_1 results in a larger elastic force, which prevents LCs from rotation by electric field and weakens the effect of electric fringing field.

Moreover, the peak in phase retardation profile near the axis of symmetry emerges when k_1 reaches 5. This is because higher elastic force is generated with larger k_1 and electric force is not strong enough to orient LCs when k_1 is above 5. As k_1 increases from 5 to 9, the peak value also decreases since more LCs are restrained by elastic forces. Therefore, it can be concluded that splay contributes to the deformation of LCs at the axis of symmetry.

Similarly, the effect of k_3 is also studied by varying k_3 from 0.01 to 9 ($k_1 = 0.01$). From simulation results shown in figure 3.9 below, it is clear that k_3 has very limited effect on resolution. Figure 3.9 (b) also shows that the phase width varies between 11~12 as k_3 increases from 0.01 to 9.

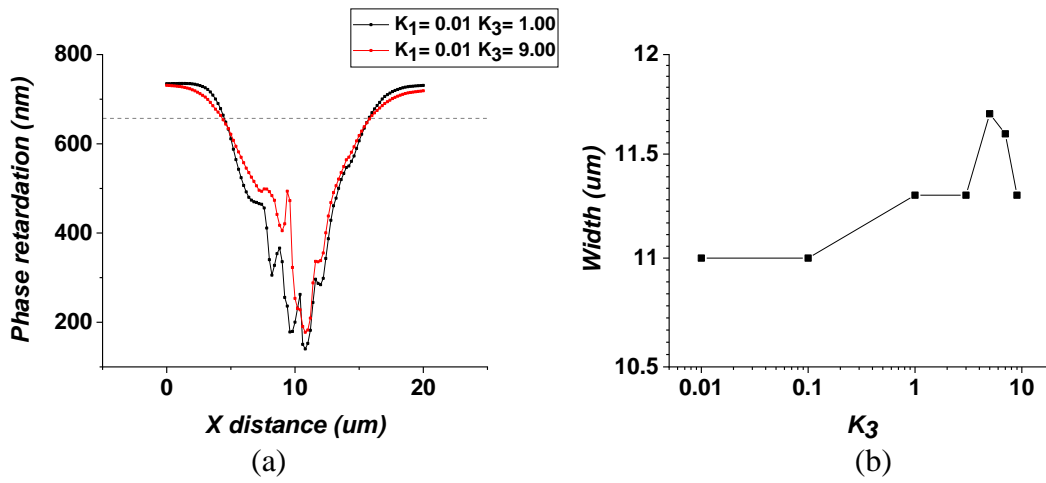


Figure 3.9 (a) Phase retardation profile for different k_3 values. (b) Phase width for different k_3 values.

To summarize the effect of k_1 and k_3 , it can be concluded that k_1 plays a dominant role in the resolution of OASLMs. LCs with larger k_1 should be preferred since electric fringing field has a smaller effect in this case compared with LCs with smaller k_1 . Similarly, this also limits the modulation depth of LCs.

Another important intrinsic parameter of LCs is dielectric constant, which determines the response of LCs to electric field. LCs molecules are polarized in the presence of electric field and dipole moments are generated. As a result, LCs rotate themselves due to the torque. The amount of dipole moments per unit volume (also called polarization density, \mathbf{P}) is proportional to dielectric constant (ϵ_r) by the following equation (for isotropic media):

$$\mathbf{P} = (\epsilon_r - 1)\epsilon_0\mathbf{E} \quad (3.2)$$

Therefore, LCs with larger dielectric constant encounter larger polarization density, which means more torque is applied to LCs. In terms of anisotropic LCs, there are two induced torque

with opposite directions, corresponding to ϵ_{\perp} and ϵ_{\parallel} . In the case of horizontally aligned LCs with parallel-alignment configuration, ϵ_{\parallel} is associated with the torque that aligns LCs with electric field while ϵ_{\perp} is related to the resisting torque, as is shown in figure 3.10 below.

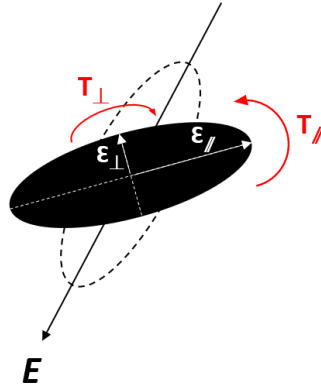


Figure 3.10 The torque of LCs under electric field.

Based on the analysis above, LCs with higher ϵ_{\parallel} or lower ϵ_{\perp} would experience larger torque to align with the electric field so this would lead to a wider phase retardation profile given the same elastic force. This is validated by the simulations shown below in figure 3.11. It is evident from figure 3.11 (a) and (b) that higher value of ϵ_{\parallel} results in a larger width and on the contrary, larger ϵ_{\perp} brings about a decreasing width. This is because high ϵ_{\parallel} or lower ϵ_{\perp} equivalently increases the torque exerted on LCs, strengthening the effect of electric field particularly at the fringing area. Therefore, higher ratio of $\epsilon_{\parallel}/\epsilon_{\perp}$ will compromise the resolution of OASLMs.

This section investigates the effect of intrinsic parameters of LCs such as elastic constant and dielectric constant in order to provide a guidance for choosing appropriate LCs materials. Elastic constants describe the internal force opposing any movement of LCs and dielectric constants determine the external force to rotate LCs. Better resolution can be achieved by selecting LCs with larger elastic constant (especially k_1) and smaller $\epsilon_{\parallel}/\epsilon_{\perp}$ ratio. In the meanwhile, modulation depth would be decreased so appropriate thickness and voltage should be used.

On the other side, LCs larger elastic constant (especially k_1) and smaller $\epsilon_{\parallel}/\epsilon_{\perp}$ ratio actually face less rotating force (or torque), which would slow the rotating speed and cause longer response time ('turn on'). Although 'turn off' time (in the absence of electric field) is also shortened since elastic force is strengthened and RC time constant is shortened.

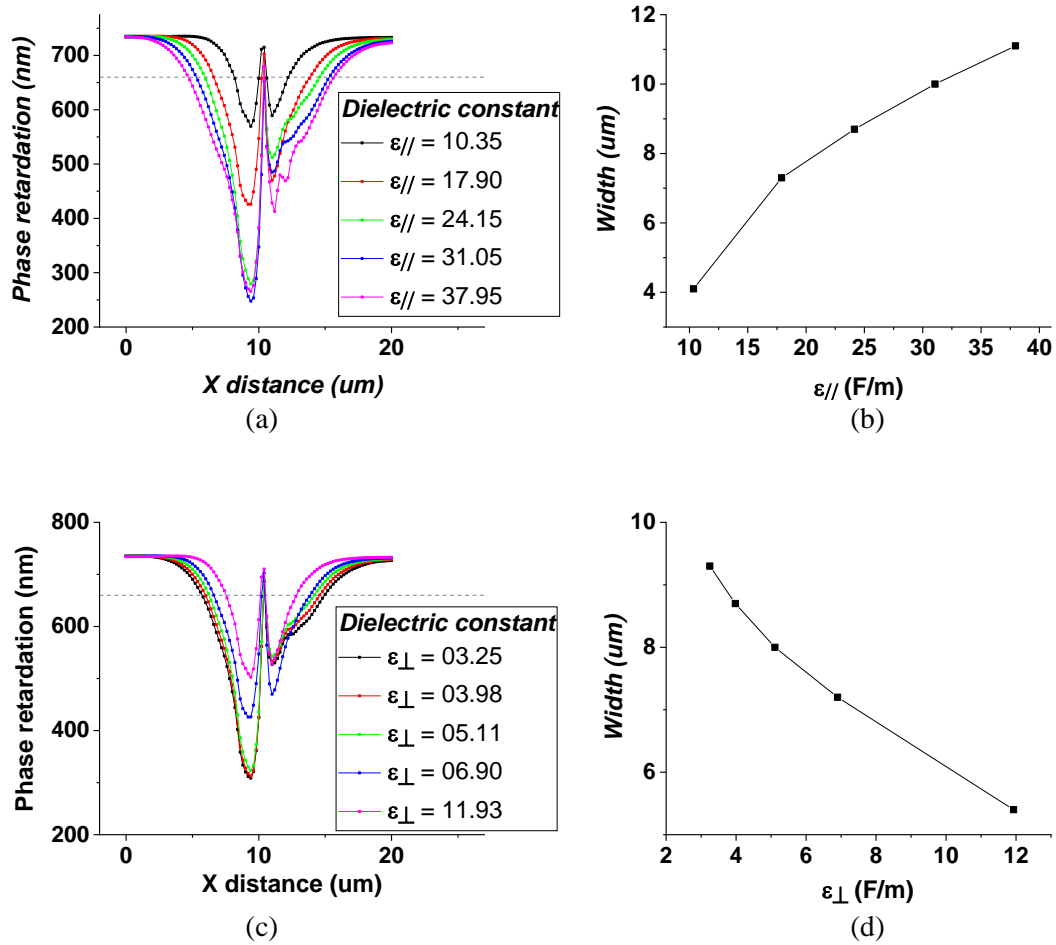


Figure 3.11 Phase retardation profile of different (a) $\epsilon_{//}$ and (b) ϵ_{\perp} values. Phase width (resolution) of different (c) $\epsilon_{//}$ and (d) ϵ_{\perp} values.

3.2.4 Other effects

There are several other factors that also affect the resolution of OASLMs. For instance, LCs in Y direction also affect the LCs in X-Z plane due to elastic force. The elastic force in Y direction was not considered in the previous sections and the bottom electrode was kept constant (1um \times 1um) for all the simulations. In order to visualize the effect of elastic force in Y-direction, a set of bottom electrodes with increasing length in Y direction from 1um to 5um until 20um are simulated while remaining the length of the other side. The results are shown below in figure 3.12:

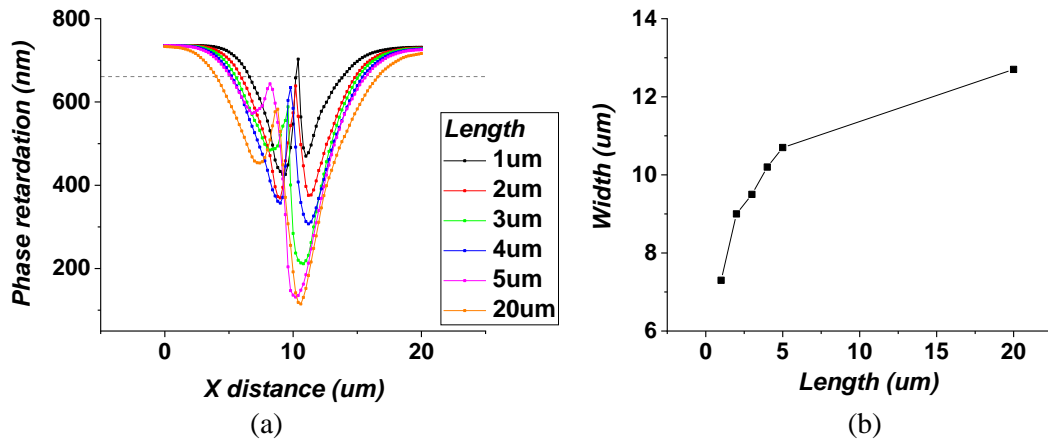


Figure 3.12 (a) The phase retardation profile for different bottom electrodes. (b) The phase width at different electrode lengths.

It is evident that the phase width (resolution) increases with longer bottom electrode because of increased elastic force in Y direction, which results in a larger rotation in X-Z plane. This provides a reference in terms of the design of the write light pattern: larger gaps between excited area help with minimising this effect.

Another approach to minimize the electric fringing field in LCs is to introduce a ‘guiding’ electrode on the other side of LCs. This can be achieved by adding a second ZnO NPs layer on the top electrode. Once the OASLM is illuminated by write light, ZnO NPs on both sides are photo-excited. As a result, the voltage drop across LCs is limited in the illuminated area.

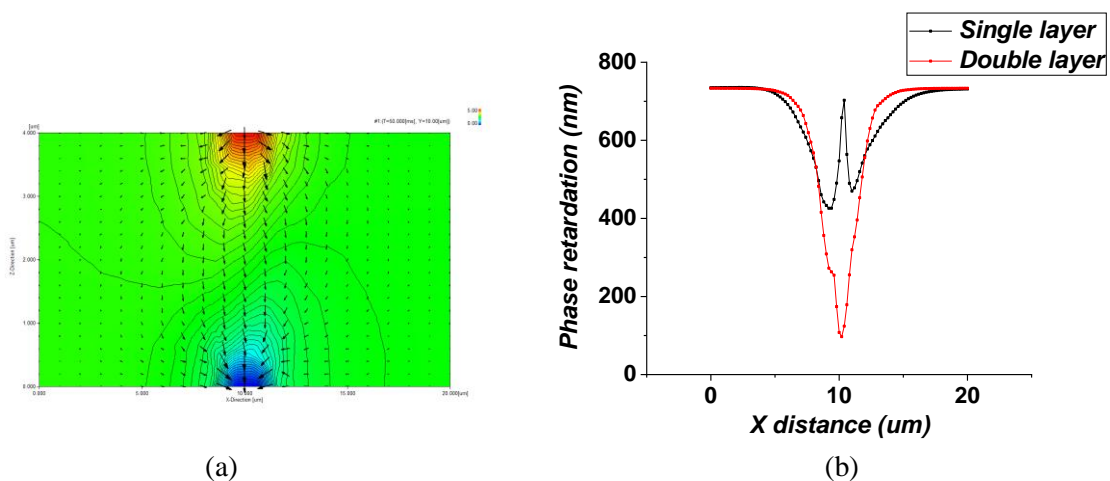


Figure 3.13 (a) The potential distribution and electric force in LCs with two ZnO NPs layers. (b) The comparison in phase retardation profile for single and double ZnO NPs layers.

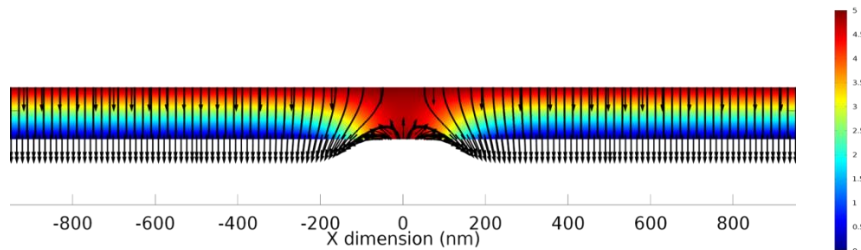
This can be simulated by using an identical electrode on the top side instead of a large-area electrode. The potential distribution (colormap and equal potential lines) and electric force

(black arrows) for two ZnO NPs layer is shown in figure 3.13 (a) above. This is completely different from OASLMs with single ZnO NPs layer, as was shown in figure 3.2 (b). Moreover, the phase retardation profiles for single ZnO NPs layer and double ZnO NPs layer are illustrated in figure 3.13 (b). It is evident that the phase width is shortened in the case of double ZnO NPs layer due to the guiding effect for electric fringing field.

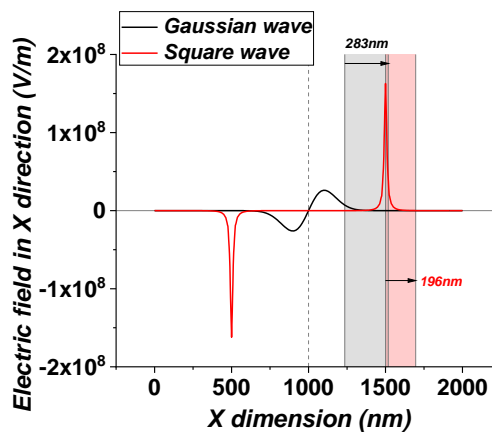
It can be concluded that double-layer ZnO NPs enables a narrower phase retardation profile by shrinking the electric fringing field.

3.2 Simulations of ZnO NP Thin Films in OASLMs

The resolution of OASLMs is also affected by ZnO NPs due to the electric fringing field. The simulation is achieved by COMSOL and a simple model for ZnO NPs layer is established as is shown in figure 3.14 (a).



(a)



(b)

Figure 3.14 (a) Simulated electric field in ZnO NPs layer. (b) Comparison of electric field in X direction at the bottom for different light intensity profiles.

A layer of ZnO NPs with 100nm in thickness is driven by a DC voltage of 5V and the write light is incident on the ZnO layer in the middle ($X=0\text{nm}$). The light intensity profile is Gaussian, and the total width is set to be 1000nm. The potential distribution (colormap) and electric force

(black arrows) are illustrated in figure 3.14 (a). It is evident that electric fringing field exists at the boundary of illuminated area, leading to the lateral drift of photogenerated charge carriers.

Electric field in X direction at the bottom is plotted in figure 3.14 (b). The affected area of the Gaussian beam is defined here by the distance in x direction from FWHM to the point with zero electric field. The affected length on one side is measured to be around 283nm. This can be improved by using a write light with sharp intensity profile such as square wave. So, a square wave of 1000nm in width is also used to compare with Gaussian beam and the affected area is measured to be 196nm, which is 70% of that for Gaussian beam. Two peaks are noticed in figure 3.14 (b) for square wave. This is because the conductivity of ZnO NPs illuminated by a write light with square intensity profile is assumed to have square shape as well. So, the electric field at the step change is large. This is ideal only for simplification and as a matter of fact, the conductivity would change gradually due to the diffusion of photogenerated charge carriers and the affected area could be even larger.

There are other factors coming from ZnO NPs that affect the resolution of OASLMs. For instance, the charge spreading at the interface between LCs and ZnO NPs would degrade the resolution. The charge spreading is caused by lateral electric field and diffusion (concentration gradient). A good way to mitigate the effect of lateral diffusion and drift is to introduce trap states such that photogenerated free charge carriers would be caught by traps in the dark area (not illuminated by write light). ZnO NPs contains a large amount of trap states and this is one of the biggest advantages of ZnO NPs as photoactive material.

3.3 Fabrication Process of OASLMs

The fabrication of OASLMs is significant since device optimization can be achieved by process optimization. In order to minimize contaminations, OASLMs were fabricated in the cleanroom (class 1000). The standard fabrication process is described below:

1. Cleaning glass substrate
 - a. Clean ITO-coated soda-lime glass substrates (1.5cm×1.5cm) with DI water, acetone and IPA respectively in ultrasonic bath for 10min each.
 - b. Dry the substrates with IPA dryer.
 - c. Treat the substrates with oxygen plasma for 5min (oxygen content 5%).
2. Coating ZnO NPs
 - a. Dispense ZnO NPs dispersion (85mg/ml) on one substrate (substrate A) by spin coating with a speed of 4000RPM for 30s (acceleration speed of 500RPM/s).

- b. Anneal the substrate in air at 200°C for 1h.
- 3. Coating alignment material
 - a. Dispense the alignment material (AM1254) on the other substrate (substrate B) by spin-coating (3000RPM, 1500RPM/s, 50s).
 - b. Pre-bake the substrate at 80°C for 2min on a hotplate, followed by baking at 200°C for 30min.
 - c. Rub the substrate with rubbing machine (roller speed of 400RPM, moving at 10mm/s).
- 4. Gluing the substrates
 - a. Dispense the glue and spacer (5µm in diameter) mixture on two sides of substrate B with a syringe, as is shown in figure 3.15 (a). The syringe is pressured by air piston.
 - b. Locate substrate A on top of substrate B (with coated side face to face), leaving a certain offset distance for external cabling, as is shown in figure 3.15 (b). Gently press the substrates until the mixture is fully expanded.
 - c. UV curing for 3min.

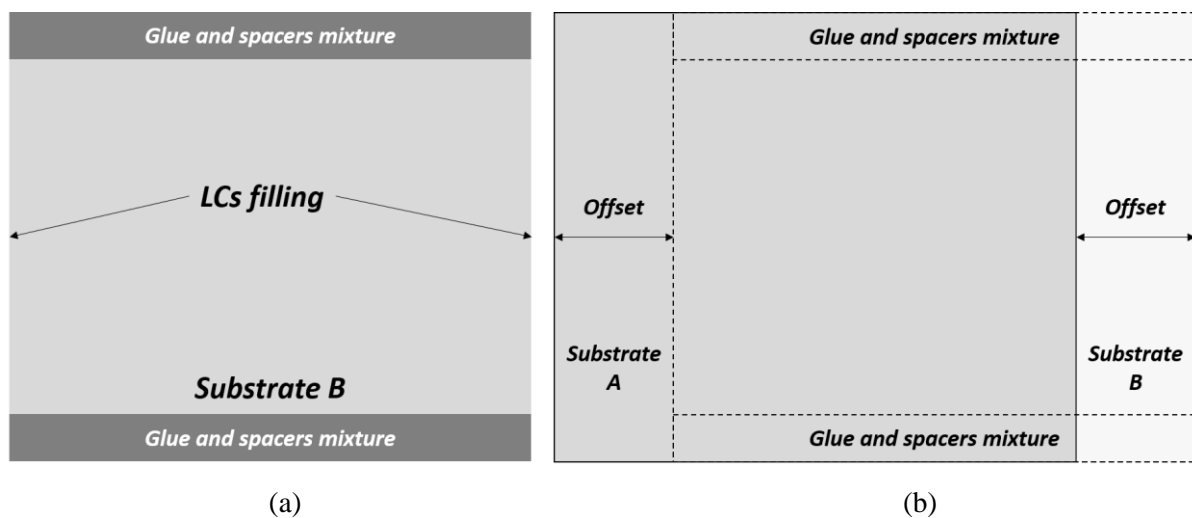


Figure 3.15 (a) Dispense the glue on two sides. (b) Offset for cabling.

- 5. Filling LCs
 - a. Put the cell on a hotplate (90°C).
 - b. Feeding the filling gap with LCs until the cell is filled with LCs by capillary force.
 - c. Cool down the cell.
- 6. Sealing the cell

- a. Seal the cell gaps with the same spacer and glue mixture.
- b. UV curing for 3min.

In the end, the cell is cleaned by acetone and IPA, and external cables are soldered onto the offset area (expose the ITO with a plastic sharp).

3.4 Characterization of OASLMs

The simulation and fabrication of OASLMs have been introduced in the previous sections. This section is to characterize the OASLMs device by experiments. OASLMs were investigated in terms of dielectric properties and optical behaviour. RC time constant influences the response time and is affected by voltage. So, the voltage providing the shortest RC time constant is valuable. RC time constant of LC was determined by dielectric measurement, which was also used to determine the RC time constant of OASLM as a whole. Optical measurement was also carried out for the purpose of determining the diffraction efficiency and response time (fall time in particular).

3.4.1 Dielectric properties LCs

Theoretical introduction to the dielectric properties of LCs has been discussed in chapter 1 and experimental study of the dielectric response of LCs is investigated in this chapter by impedance spectroscopy. A LCs cell was fabricated using similar processes as OASLM. The alignment layer (AL1259) was spin-coated and baked, prior to gluing the substrates with spacer-glue mixture (4 μ m in diameter). Alignment layer was spin-coated on both substrates (top and bottom). Nematic LCs (8CB) was filled at 90°C (on a hotplate) by capillary force and external cables were soldered in the end.

Impedance spectroscopy was performed on the cell using Autolab PGSTAT302. The frequency range was 0.01Hz~1MHz. The Bode plot and Nyquist plot at 1V (DC) are shown below in figure 3.16 (a) and (b) respectively. It is evident that there are two relaxation mechanisms existing (two relaxation peaks in Bode plot and two semicircles in Nyquist plot). Therefore, two RC parallel circuits in series were used to simulate the cell. The simulated results for R and C values are shown in figure 3.16 (c) and (d). According to the actual structure of the cell, one RC represents LCs and the other one represents the alignment layer. The alignment layer is insulating and has larger resistivity while LCs layer is more conductive due to the existence of ionic impurities inside LCs. Moreover, the capacitance for LCs layer increases with higher DC voltage as LCs molecules rotate towards vertical direction under electric field and the effective

dielectric constant of the LCs layer increases. So R_1/C_1 represents LCs and R_2/C_2 represents the alignment layer.

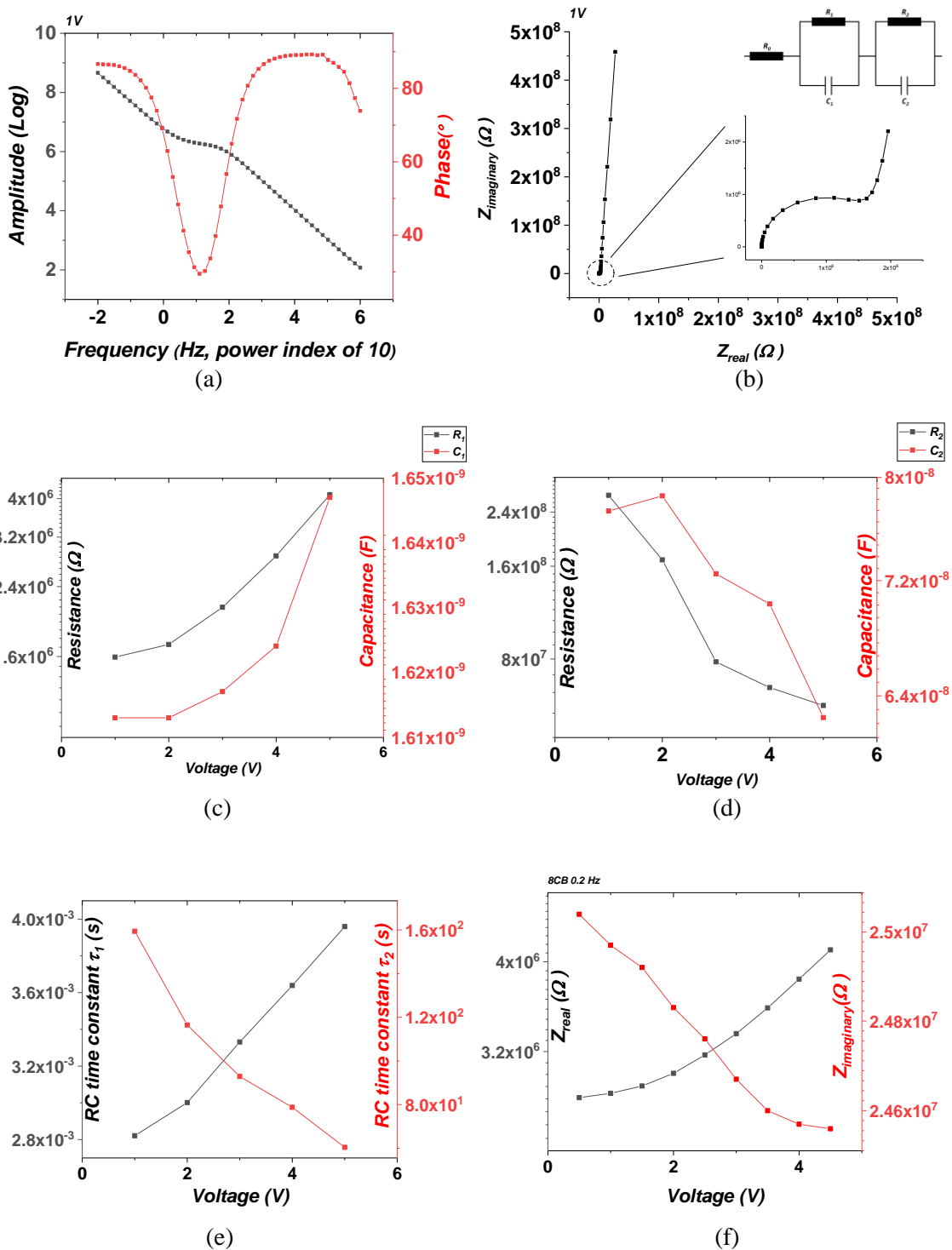


Figure 3.16 The (a) Bode plot and (b) Nyquist plot of the LCs cell. The simulated (c) Resistance and (d) Capacitance of LCs and alignment. The (e) RC time constants of LCs and alignment under different DC voltages. (f) The overall impedance of the cell under different DC voltages.

The RC time constants of LCs and alignment layer are also shown in figure 3.16 (e). Based on the analysis above, the RC time constant τ_1 stands for LCs while τ_2 stands for the alignment layer. The RC time constant of LCs is in the order of milliseconds while that of alignment layer is much larger (more than 4 orders). In addition, it is clear that higher DC voltage results in a larger RC time constant of LCs because LCs under higher DC voltages rotates more (more deviation from equilibrium position) and it takes a longer time (RC time constant) to relax back to the equilibrium position. Figure 3.16 (f) also shows the overall resistance and capacitance of the LCs cell. The imaginary impedance decreases at higher DC voltage because higher DC voltage results in the molecular orientation and increases the effective dielectric constant and capacitance. On the contrary, the real impedance increases with higher DC voltage, this might be associated with higher barrier for charge movement.

Furthermore, another type of nematic LCs (E7) was also investigated with the same method. The E7 cell was fabricated with the same parameters (cell size and thickness) and the RC time constants are shown in figure 3.17 (a). Similarly, the RC time constant for E7 LCs also increases at higher DC voltages. The RC time constant for alignment layer in both cases are in the same order but not exactly the same. This might be caused by the error generated during fabrication or the different interaction with two types of LCs. The comparison of RC time constant between E7 and 8CB LCs is shown in figure 3.17 (b). It is clear that 8CB LCs are more suitable than E7 LCs for high driving voltage (>3V) because they have less RC time constant, indicating a shorter time to relax back.

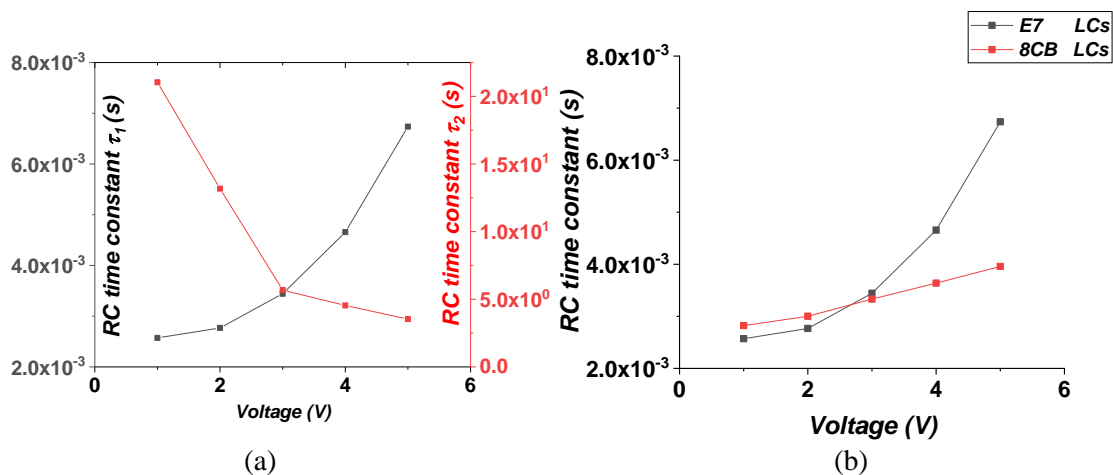


Figure 3.17 (a) RC time constants for E7 LCs. (b) Comparison between E7 and 8CB LCs under different DC voltages.

3.4.2 Dielectric properties of OASLMs

The dielectric response of OASLMs was investigated. The dielectric response of OASLMs as a whole system is important because the dielectric response of LCs and ZnO NPs in the same system (OASLMs) is not necessarily identical (normally different) to the response of the individuals. The interaction between ZnO NPs and LCs could strongly affect their behaviour under electric field. For instance, the interface between LCs and ZnO NPs is extremely important as it is full of trap states, defect states and impurities, strongly affecting the charge carrier distribution and hence the electric field.

The dielectric response OASLMs was characterized with the same method. The Bode plot of OASLM is shown below in figure 3.18 (a). It is clear that two apparent relaxation peaks exist, indicating two polarization mechanisms (LCs and ZnO NPs). By simulating and fitting the Nyquist plot, the R / C values of LCs / ZnO NPs were calculated. The RC time constants for LCs and ZnO NPs are shown in figure 3.18 (b). It is shown that the RC time constants are distinctive (almost 2 order of difference). According to the previous investigation, it is reasonable to conclude that ZnO NPs layer has a larger RC time constant than LCs layer, indicating that ZnO NPs layer is the main limiting factor for the response speed of OASLMs.

The dielectric response of OASLMs under UV (write light) was also measured, as is shown in figure 3.18 (c). It is evident that the low-frequency peak disappeared (flattened) under UV because ZnO NPs became conductive under UV excitation. Conductive ZnO NPs have little dielectric behaviour so the phase plot (red axis) is close to zero. This confirmed the previous conclusion. In addition, the overall R and C values of OASLMs under UV are shown in figure 3.18 (d). The capacitance increases with DC voltage as LCs molecules rotate, increasing the effective dielectric constant (same as the previous results). The resistance decreases with higher DC voltage and reaches a minimum at about 3V.

The RC time constant of OASLM under UV is shown in figure 3.18 (e). It shows a decreasing trend from 0V to 3V and increases after 3V. The minimum RC time constant is about 4×10^{-5} s at 3V. This finding is of great importance to the practical operation of OASLMs as this finds the optimum operating voltage of 3V that the OASLM has the quickest response time during the writing period.

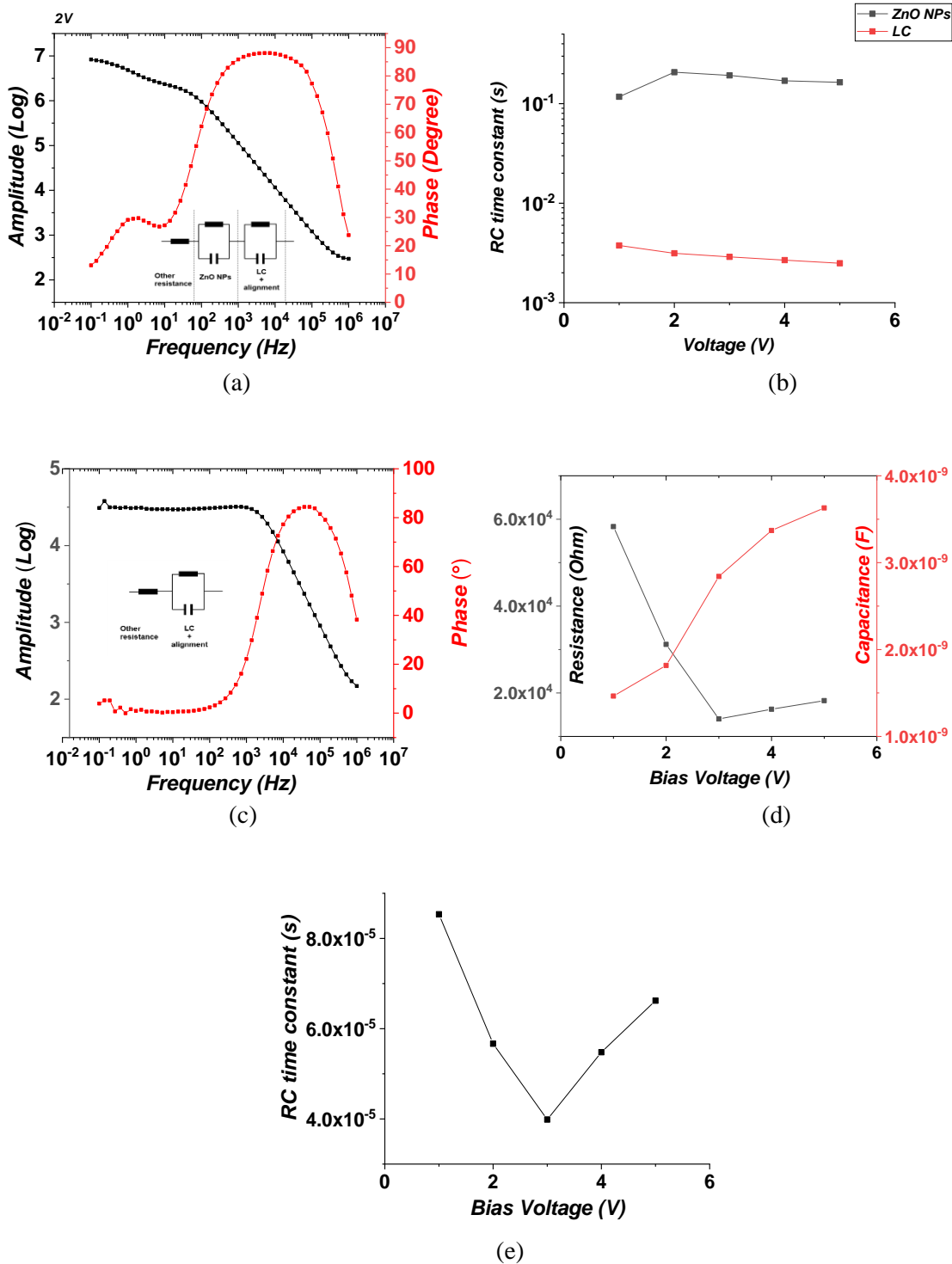


Figure 3.18 The (a) Bode plot and (b) RC time constants of OASLM. The (c) Bode plot and (d) overall resistance / capacitance of OASLM under UV. (e) The RC time constant of OASLM under UV.

3.4.3 Optical properties of OASLMs

The optical characterization of OASLMs was carried out on an optical bench with the following optical setup (figure 3.19).

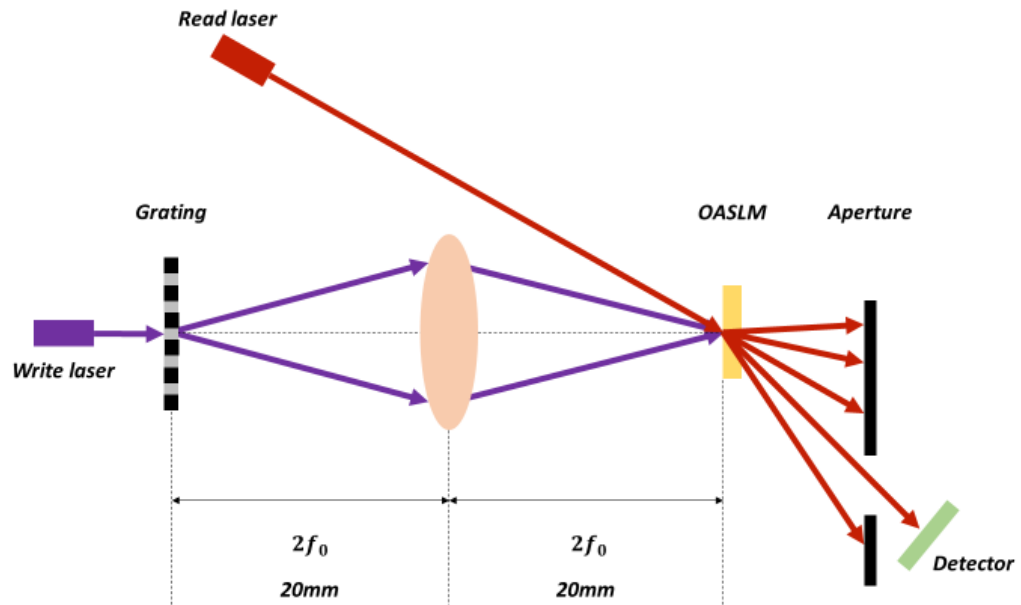


Figure 3.19 The optical setup for OASLM characterization.

A 4-f configuration was used to write the grating pattern onto the OASLM. A write laser (405nm) was placed behind the grating and a read laser (635nm) was located near the lens. Light from the read laser was diffracted by OASLM because the grating was transferred onto OASLM by the write light. The first order of the diffraction pattern was recorded by a photodetector while the rest of the diffraction pattern was blocked by an aperture. The OASLM was driven by a signal generator, outputting a sinusoidal wave with the frequency of 0.5Hz and the peak-to-peak voltage of 2V. The photodetector was connected with an oscilloscope such that the first-order diffraction pattern could be recorded instantly. The position and orientation of the photodetector was adjusted such that the recorded light had the maximum intensity and the least interference from other diffraction orders.

With the write laser always on (constant writing), the signal of the read light (first-order) was recorded in figure 3.20 (a) below. It is clear that there are 4 peaks in each driving cycle (2 seconds): two peaks with large intensity and two peaks with small intensity. This is associated with the peak amplitude of the driving voltage, which is discussed in detail later.

Figure 3.20 (b) shows the decrease of the signal after the write light was turned off. The 'off' time from 90% to 10% was measured to be 47.5s. This is the actual challenge for OASLMs because slow fall time means that there would be ghost images or sticking images if the write light is off.

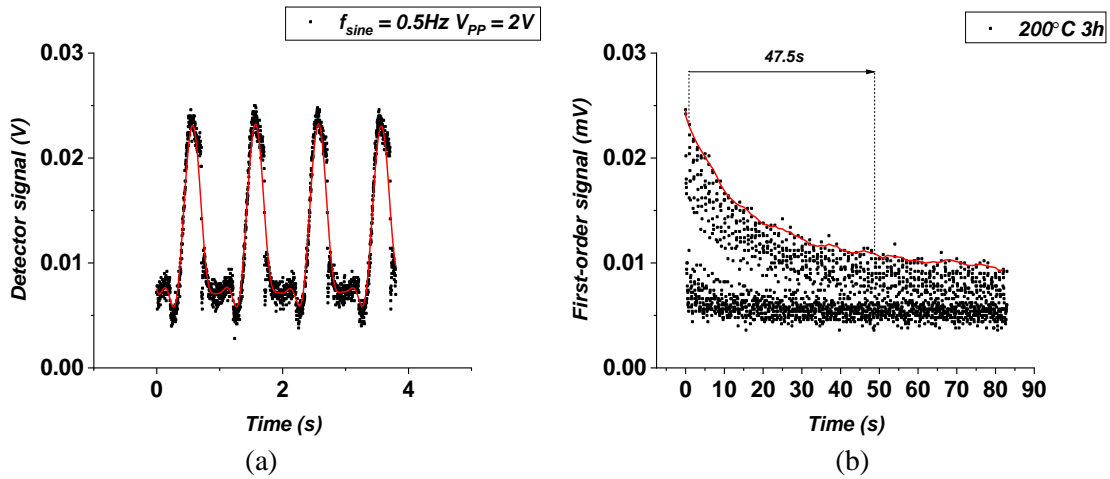


Figure 3.20 (a) Recorded signal from photodetector. (b) The decrease of signal intensity after the write light was turned off.

The long ‘fall’ time reveals that it is not applicable for dynamic applications like video-rate 3D holographic displays, however it might be suitable for static applications such as the exhibition in the museum.

3.5 The Optimization of ZnO NPs-Based OASLMs

As was mentioned before, a record-high resolution of 825 lp/mm has been successfully achieved by ZnO NP-based OASLM as a result of trap states in ZnO NP layer [108]. This is significant for the application of holographic displays since a larger size of the reconstructed image and a larger viewing angle can be realized with a higher spatial resolution from OASLM (hologram). However, ZnO NP-based OASLM also has weaknesses such as low diffraction efficiency (2.26%) and slow response time (tens of seconds), heavily limiting the development in dynamic holographic displays. Therefore, the optimization of ZnO NP-based OASLM is necessary and valuable.

3.5.1 Improving the diffraction efficiency

- **Sinusoidal signal**

A sinusoidal driving signal was initially used to drive the OASLM with a peak voltage (V_P) of 2V and a driving frequency (f_{sine}) of 0.5Hz. The first-order diffraction signal recorded by the photodetector is shown in figure 3.21 (a). It is clearly shown that there are four peaks during a full driving period (2s): two peaks (V_{peak} and V_{side}) on both sides of the rising peak of the driving signal and two peaks (V_{valley}) on two sides of the falling peak. The maximum intensity of the

first-order diffraction pattern is an indication of maximum diffraction efficiency (η_{\max}) according to equation 3.3:

$$\eta = \frac{I_1}{I_0} \quad (3.3)$$

where I_1 and I_0 are the intensity of first-order diffraction pattern and zeroth-order pattern without write light. It is also noted from figure 3.21 (a) that there is a shift in time between the peaks of the driving signal and η_{\max} . This can be explained by the nature of a phase grating. OASLM in this optical configuration is effectively acting as a binary phase grating and the diffraction efficiency (η) is dependent on the difference in phase retardation ($\Delta\delta$) between adjacent phase levels, as is shown in figure 3.21 (c). This is based on the equation below:

$$\eta = \left[\frac{2}{\pi} \times \sin(\Delta\delta)\right]^2 \quad (3.4)$$

Therefore, η_{\max} occurs when $\Delta\delta$ is $\pi/2, 3\pi/2, 5\pi/2 \dots$ etc. Moreover, the phase retardation is determined by the birefringence (Δn) of LCs based on:

$$\delta = \Delta n \times 2\pi \frac{d}{\lambda} \quad (3.5)$$

where d is the thickness of the LC layer and λ is the wavelength of the read light. The birefringence of LCs is controlled by the amplitude of the driving signal (V_P) so the diffraction efficiency is also controlled by V_P . As sinusoidal V_P rises from 0V to 2V, $\Delta\delta$ also increases from 0 to $\pi/2$ where diffraction efficiency reaches its maximum. However, the diffraction efficiency reduces when V_P continues to rise since diffraction efficiency decreases after $\pi/2$ (V_2 in figure 3.21 (c)). Accordingly, V_P of 2V results in $\Delta\delta > \pi/2$, and this is the reason of four peaks generated in the diffracted signal on both sides of the driving peaks. The difference in height among four peaks might be a result of charge sticking at the interface between ZnO NP layer and LCs layer. This is verified by reducing V_P to 1.2V and the result is shown in figure 3.21 (b). The number of peaks within a full driving cycle is reduced to two, corresponding to the peaks of the driving signal. This situation is depicted in figure 3.21 (c) as V_1 . Peak height of V_{peak} and V_{side} in the diffracted signal driven by various V_P is depicted in figure 3.21 (d). It is evident that the maximum V_{peak} is obtained at $V_P=1.6V$, at which the side peak (V_{side}) starts to appear. It can be concluded that the diffraction efficiency of the OASLM driven by a sinusoidal signal reaches its maximum when the peak amplitude is 1.6V.

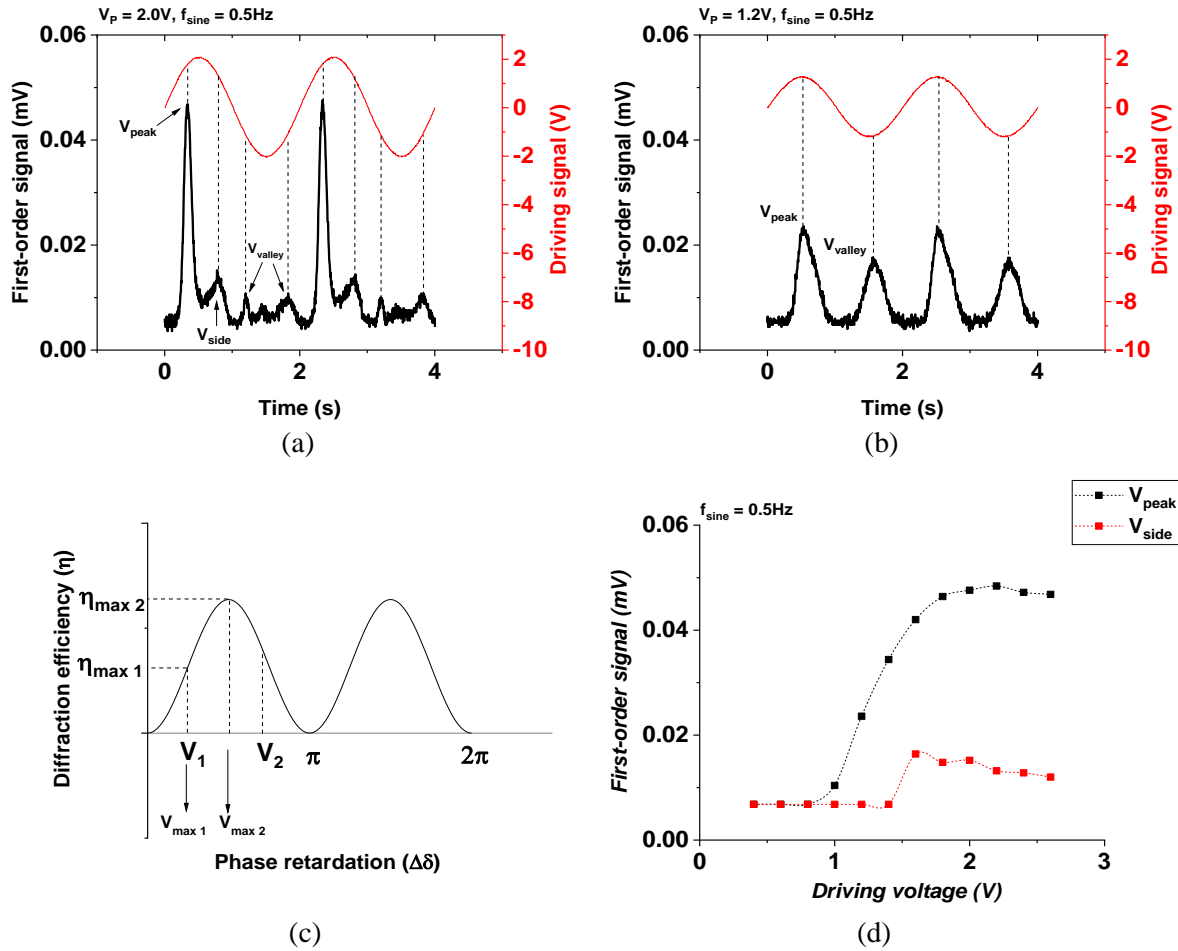


Figure 3.21 First-order diffraction signal when the driving voltage has an amplitude of (a) $V_P=2V$ and (b) $V_P=1.2V$. (c) The relationship between diffraction efficiency and phase retardation. (d) The intensity of V_{peak} and V_{side} at different voltage amplitudes.

- **Triangular signal**

Experiments were carried out for OASLMs driven by a triangular signal. The driving frequency is maintained at 0.5Hz and the results of $V_P=2V$ is shown in figure 3.22 (a). Similarly, four peaks in the diffracted signal were detected in one period while the peak number is reduced to two when $V_P=1.4V$, in alignment with the peaks in the driving signal (figure 3.22 (b)). Figure 3.22 (c) shows the voltage dependence of the V_{peak} and V_{side} . It can be concluded that the maximum diffraction efficiency is realized when $V_P=1.8V$ for a triangular driving signal. By comparing the intensity of the first-order diffraction pattern obtained by a sinusoidal and triangular driving signal (figure 3.22 (d)), it can be concluded that sinusoidal driving signal can provide a higher diffraction efficiency compared to triangular driving signal for OASLM under the same driving frequency.

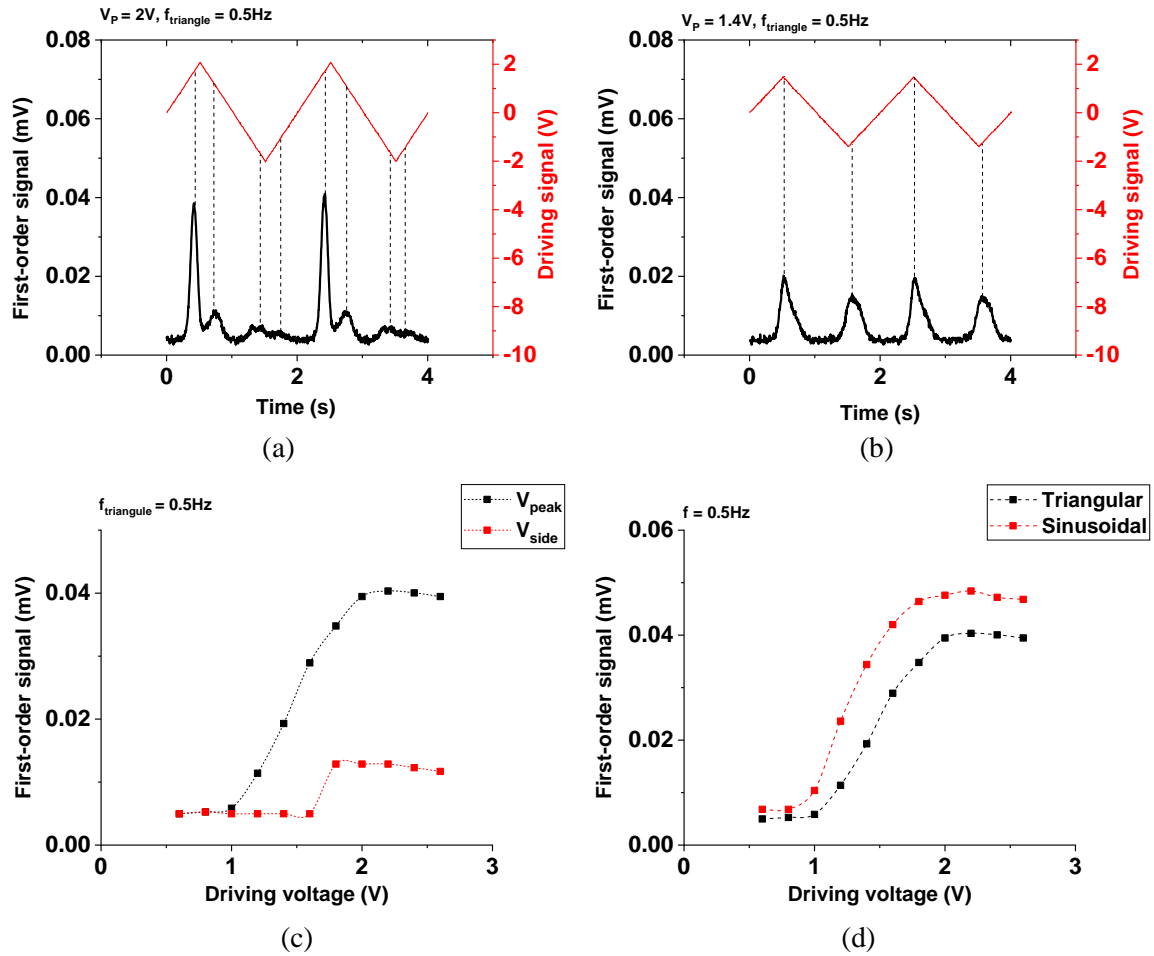


Figure 3.22 First-order diffraction signal when the driving voltage has an amplitude of (a) $V_p=2V$ and (b) $V_{pp}=1.4V$. (c) The intensity of V_{peak} and V_{side} at different voltage amplitudes. (d) Comparison of first-order diffraction signal between sinusoidal and triangular driving signal under the same driving frequency (0.5Hz).

Higher diffraction efficiency can be realized by a sinusoidal driving signal because the charge accumulation across LC layer is faster for a sinusoidal signal compared to a triangular signal. In the meanwhile, lateral diffusion of photogenerated charge carriers exists in both cases, increasing the phase retardation (δ) at the lower level of the phase grating, compromising the difference in phase retardation ($\Delta\delta$) and thus diffraction efficiency. The charge leakage caused by diffusion was studied by a square driving signal. A square signal of 1V in peak amplitude and 0.5Hz in frequency was used to drive the OASLM, as is shown in figure 3.23 (a). It is clear that the diffraction efficiency increases after the driving voltage changes its sign and it then decreases within the period. The decay of diffraction efficiency results from the charge leakage. The voltage dependence of the diffracted signal is shown in figure 3.23 (b) and the maximum diffraction efficiency was achieved at 1.2V. It is also observed that the maximum intensity of the diffracted signal during the positive driving period and the negative driving period is

different due to the charge sticking. In addition, the diffraction efficiency in this case is only 47.9% of that obtained by a sinusoidal driving signal.

The charge sticking was also investigated by measuring the imaginary impedance of an OASLM cell (in dark condition) under positive and negative DC bias voltages, as shown in figure 3.23 (c). Impedance measurement was carried out by Autolab PGSTAT302 at a fixed frequency of 10Hz. Figure 3.23 (c) shows the decrease of imaginary impedance as the DC voltage increases because of the rotation of LCs. It is also observed that the imaginary impedance on the two sides of DC voltage is not symmetrical, which is a result of remaining charges across LC layer.

The effect of driving frequency was also studied, as shown in figure 3.23 (d).

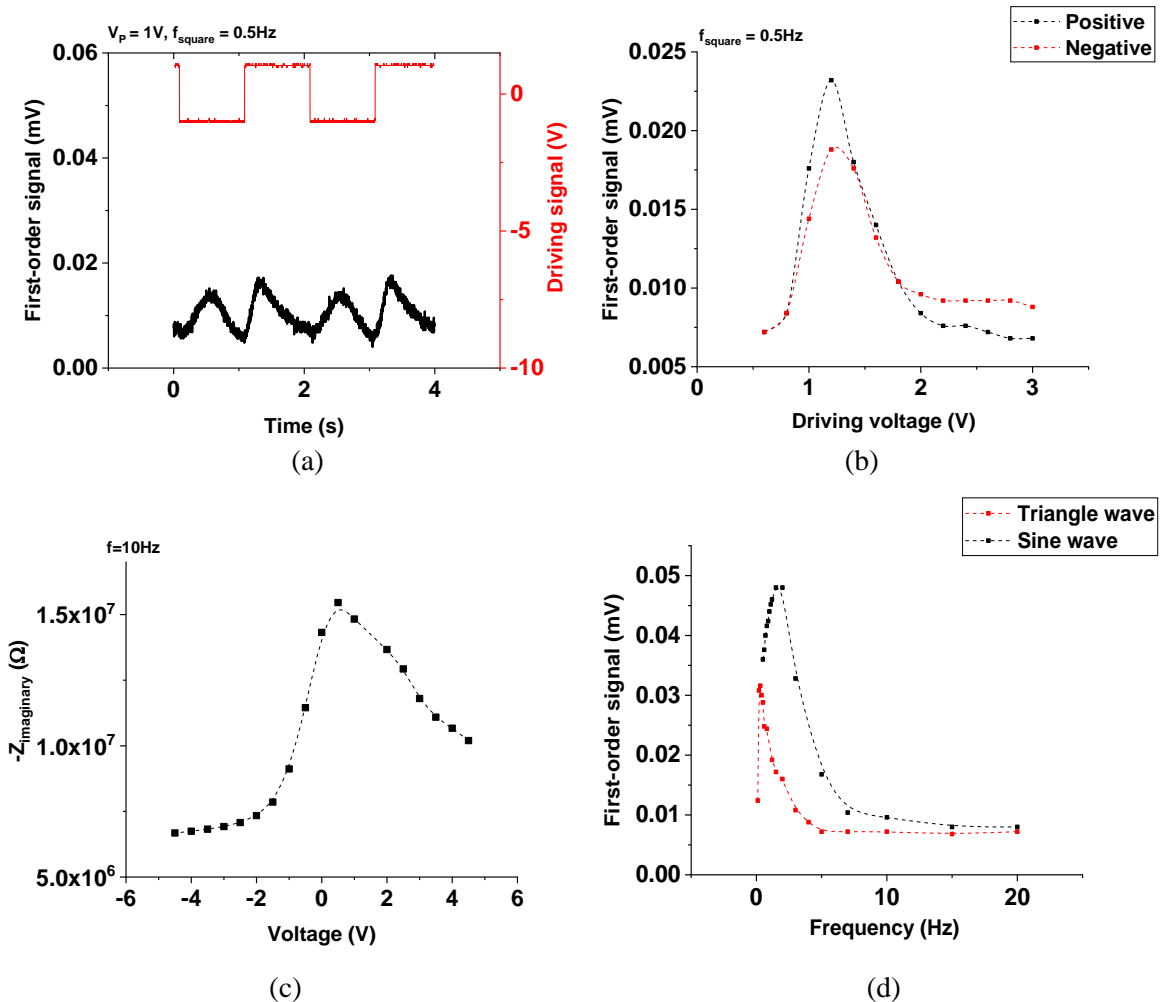


Figure 3.23 (a) The first-order diffraction signal driven by a square signal. (b) The height of the diffracted signal at different voltage amplitudes. (c) The imaginary impedance of an OASLM cell measured with positive and negative DC bias voltages. (d) The effect of driving frequency on diffraction efficiency.

It can be observed that the diffraction efficiency reaches its maximum at certain frequencies for both waveforms and it is illustrated that the OASLM can be operated at a higher frequency by a sinusoidal wave (1.5Hz) than triangular wave (0.3Hz). Moreover, the maximum diffraction efficiency is higher if the OASLM is driven by a sinusoidal wave.

By comparing the diffraction efficiency of different waveforms, amplitudes and frequencies, it can be concluded that the maximum diffraction efficiency of ZnO NP-based OASLM can be obtained by a sinusoidal driving signal with a peak amplitude of 1.6V and frequency of 1.5Hz.

In order to further confirm the existence of charge sticking and to investigate its effect on device performance, OASLMs with a SiO₂ interface layer between ZnO NP layer and LC layer was investigated. A 50nm (in thickness) SiO₂ layer was slowly deposited on top of ZnO NP layer by e-beam evaporation, followed by the same OASLM assembly processes. The signal of the first-order diffraction pattern was received and shown in figure 3.24 (a) and (b) below.

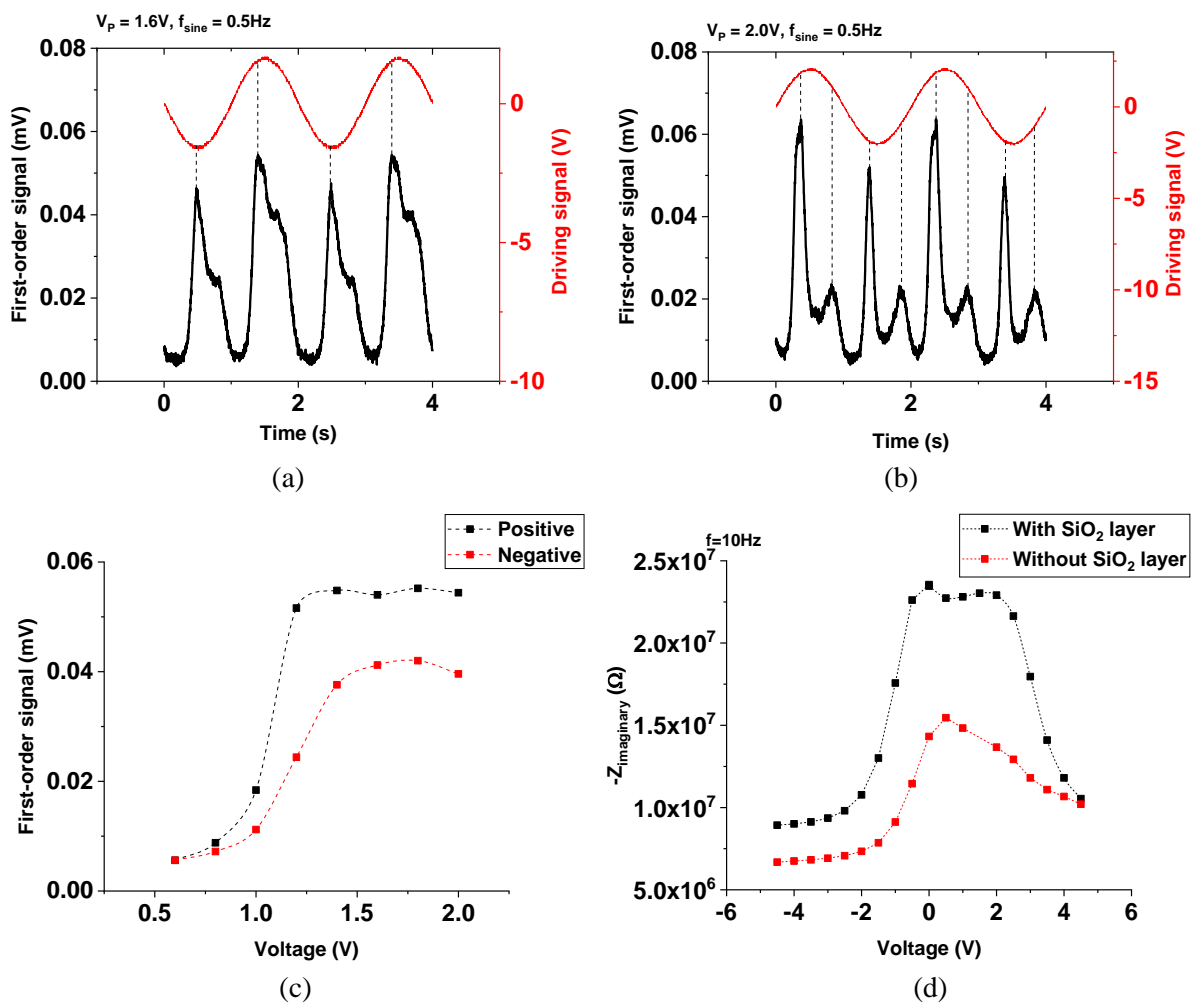


Figure 3.24 The first-order diffraction pattern generated by a sinusoidal wave with (a) $V_{peak}=1.6V$, $f=0.5Hz$ and (b) $V_{peak}=2.0V$, $f=0.5Hz$. (c) The height of the diffracted signal at different voltage amplitudes. (d) The imaginary impedance of OASLM with and without SiO₂ layer.

The OASLM was driven by a sinusoidal wave with a peak amplitude of 1.6V and 2.0V respectively while the driving frequency was kept at 0.5Hz for both cases. It is clearly demonstrated that the diffraction peaks in the positive and negative driving cycle have similar height, much less than the height difference of previous OASLMs (without SiO₂ layer). This indicates that the charge sticking is suppressed by adding a SiO₂ layer whereas it still exists.

The diffraction efficiency is also dependent on the amplitude of driving voltage, as is shown in figure 3.24 (c). It also shows a difference between positive and negative driving voltages. Finely deposited SiO₂ layer can protect the ZnO NPs layer from charge exchange with LCs layer. However, the charge sticking still exists at the interface between SiO₂ layer and ZnO NPs layer.

In addition, the imaginary impedance (Z_{imag}) was compared by conducting impedance spectroscopy at 10Hz, as is illustrated in figure 3.24 (d). The Z_{imag} decreases after introducing a SiO₂ layer as a result of series capacitance. Moreover, the difference in Z_{imag} between positive and negative driving voltages is reduced. The ratio of Z_{imag} at -4.5V over Z_{imag} at +4.5V is 1.1 for OASLM with SiO₂ compared to 1.5 for OASLM without SiO₂.

3.5.2 Improving the response time

According to the previous analysis, the response speed of OASLMs is limited by the trap states at the interface between LCs and ZnO NPs. Photogenerated charge carriers are trapped at the interface and they stay at the interface after the write light is off. The trapped charge carriers maintain the voltage across LCs and ghost images are formed. Therefore, two approaches were taken in order to shorten the fall time: decrease the trap activation energy by raising the annealing temperature of ZnO NPs and introducing a layer of SiO₂ (50nm in thickness) between the interface. The results are shown below in figure 3.25. It has been clearly shown that OASLM with low annealing temperature had a longer falling time (47.5s) while the falling time was shortened to 14.4s if ZnO NPs were annealed at higher temperature. This is because the trap activation energy is decreased after annealing so that photogenerated charge carriers are easily excited by thermal energy and recombined with holes.

Figure 3.25 (b) also proves that the interface trapping can be further improved by introducing a SiO₂ layer. A thin layer (50nm) of SiO₂ was deposited by e-beam evaporation on top of ZnO NPs (annealed at 200°C for 1h). The falling time was recorded to be 2.9s, which is about 1/15 of non-SiO₂ OASLM. This indicates that the interface plays an extremely important role in falling time of OASLMs.

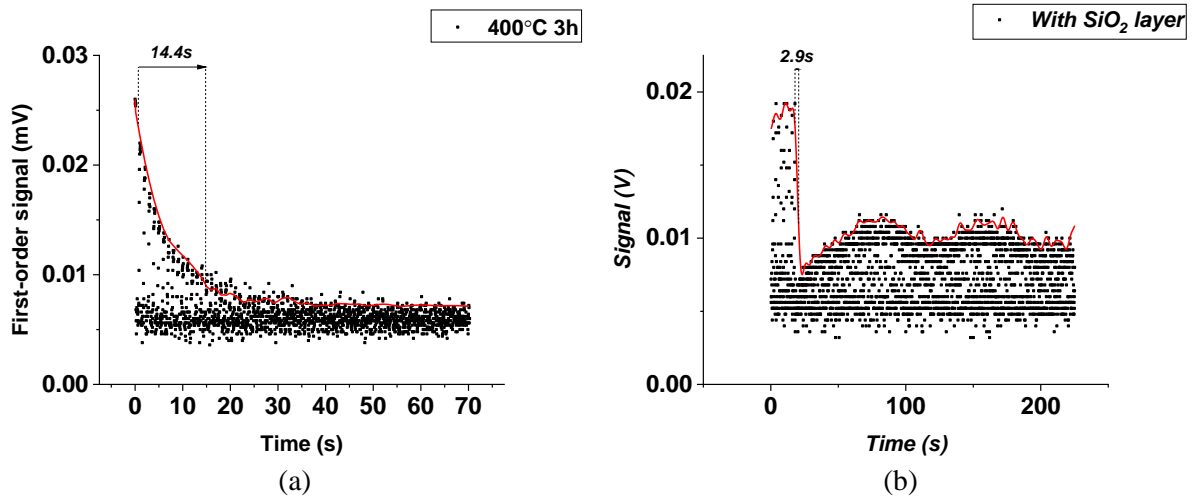


Figure 3.25 The signal falling after write light is off. (a) ZnO NPs were annealed in air at 400°C for 3h. (b) A layer of SiO₂ was introduced between ZnO NPs and LCs.

One thing to be noted is that high annealing temperature results in the deformation of substrate surface. This is illustrated in figure 3.26 below.

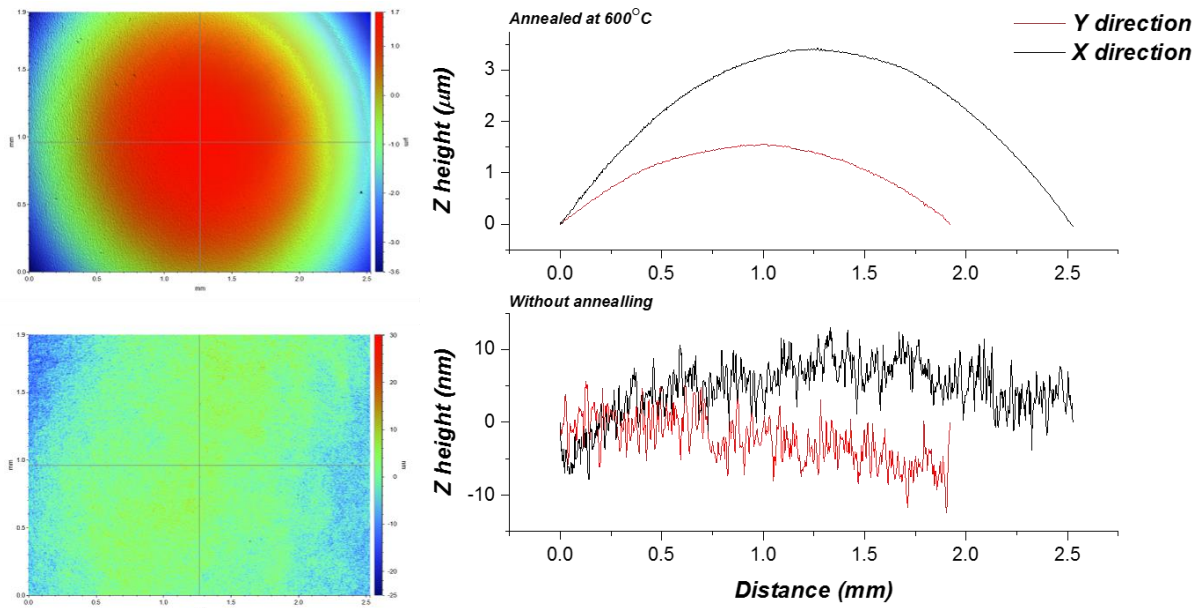


Figure 3.26 The annealing effect on glass substrate.

The surface profile of soda lime glass substrates after 600°C annealing for 3h was measured. It clearly showed a curved surface profile and the maximum variation in surface height is more than 3μm in 2mm×2mm area. In contrast, the surface variation without annealing is less than 10nm. Undesired contact was generated during the assembly of OASLMs due to the surface curvature and this also led to the thickness non-uniformity of LCs layer. Quartz or sapphire glass substrate can be used for high-temperature treatment.

To summarize the conclusions so far, ZnO NP-based OASLM was optimized in terms of diffraction efficiency and response time. By investigating the driving signal of OASLM, the highest diffraction efficiency was achieved by a sinusoidal driving signal with a peak amplitude of 1.6V and frequency of 1.5Hz. And it was also found out that the introduction of a SiO₂ layer can effectively improve the diffraction efficiency by mitigating the charge sticking effect.

The response speed was also optimized by reducing the fall time. Two approaches were used: increasing the thermal annealing temperature of ZnO NP layer and introducing a SiO₂ layer. The shortest fall time was achieved at 2.9s compared to 47.5s (non-optimized OASLM).

3.5.3 Heterojunction Photodiode in OASLMs

The photoconductive property of ZnO NP has been investigated and utilized for high-resolution OASLMs. However, photoconductors are susceptible to material imperfections such as trap states and defect states. Therefore, a photodiode structure was proposed in this section: ZnO NPs and PEDOT:PSS heterojunction.

Poly(3,4-ethylenedioxythiophene) polystyrene sulfonate (PEDOT:PSS) is a type of organic conductor material with great potential, which is particularly suitable for optical applications due to its optical transparency and water-solubility. PEDOT:PSS is composed by conjugated conductive polymer, which can be further classified into two ionomers: poly(3,4-ethylenedioxythiophene) (PEDOT) carrying positive charges and polystyrene sulfonate (PSS) with negative charges, as is shown in figure 3.27.

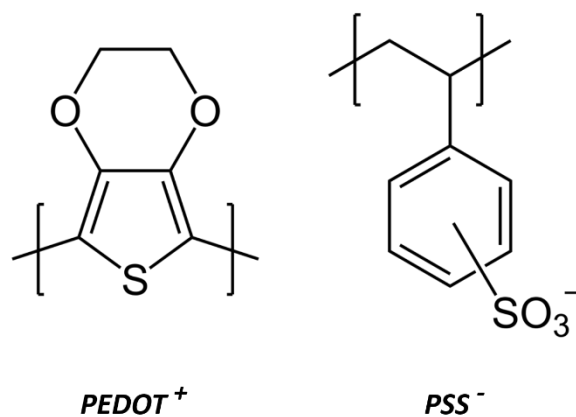


Figure 3.27 The molecular structure of PEDOT and PSS ionomer.

PEDOT:PSS has attracted a large amount of research interests due to its high electrical conductivity (up to 4000 S/cm depending on the processing conditions) [109][110], optical transparency in the visible range (up to 95%) [110] and chemical stability in air. PEDOT:PSS has been used in various applications such as light emitting diode as the hole injection layer,

solar cells as the interlayer, and supercapacitors and flexible devices as the electrode [109]. Water dispersion of PEDOT:PSS are available because PSS is playing the role of surfactant, dispersing and stabilizing the PEDOT. In addition, PSS increases the solubility, enabling the solution-based processes of PEDOT:PSS such as drop-casting, spin-coating, dip-coating, inkjet printing and roll-to-roll printing.

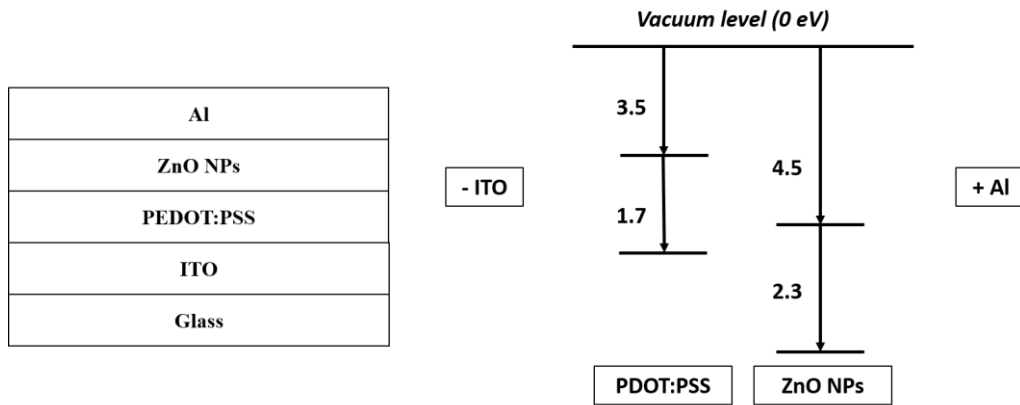


Figure 3.28 The structure of ZnO NPs-PEDOT:PSS heterojunction and the energy band diagram.

An organic-inorganic heterojunction is formed between ZnO NPs and PEDOT:PSS, which is effectively a photodiode instead of a photoconductor. Photodiode is expected to provide a better performance than photoconductor in terms of response time and responsivity. The structure of the sample is shown in figure 3.28. Samples were prepared by firstly spin-coating PEDOT:PSS solution (in water) on thoroughly cleaned glass substrates (covered with ITO electrodes). The substrate was then baked on a hotplate at 200°C in air for 1h. Next, ZnO NPs dispersion (85 mg/ml in ethanol) was spin-coated on top of PEDOT:PSS film, and the substrate was baked again at 200°C in air for 1h. Finally, aluminium electrode was deposited on top by thermal evaporation.

- **Electrical properties**

The I-V characteristics of PEDOT:PSS and ZnO NPs heterojunction displayed a strong electrical rectification behaviour, as is shown in figure 3.29 (a). It is clear to see that the current ratio of forward bias and reversed bias at 2V is about 6700. The junction was able to operate at a maximum of 4V~5V. Samples of ZnO NPs sandwiched between ITO and Al was prepared and measured for comparison, as is shown in figure 3.29 (b). It is evident that the current shows no difference for both positive and negative voltages. In addition, the current for the heterojunction is lower than ZnO NPs because PEDOT:PSS in this case is resistive.

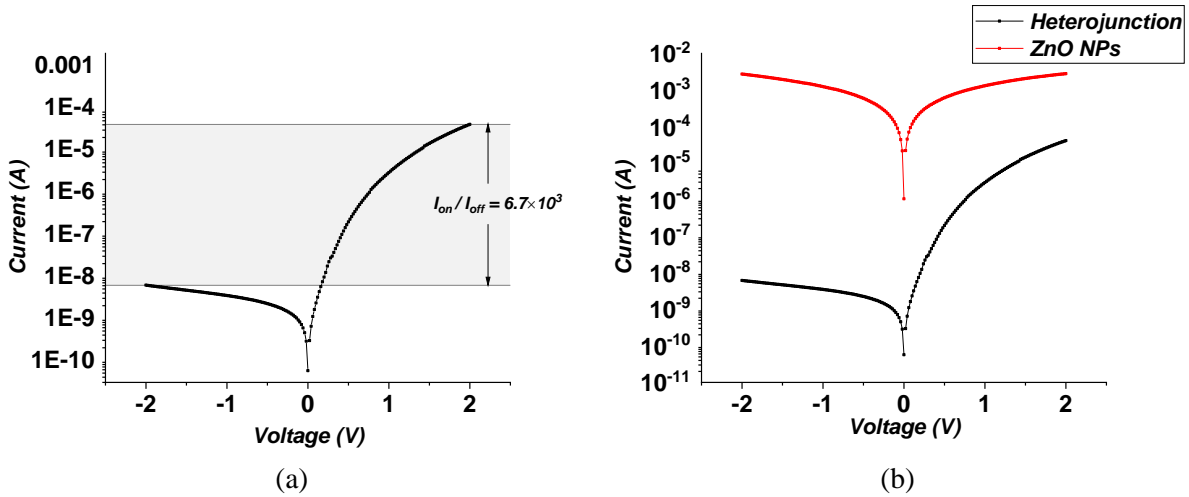


Figure 3.29 (a) The I-V characteristics of ZnO NPs and PEDOT:PSS heterojunction. (b) The comparison in I-V characteristics between heterojunction and ZnO NPs.

- **Junction barrier height**

The junction barrier height can be determined by two different methods: capacitance-voltage measurement (CV) and low-temperature measurement. Low-temperature measurement was not available in this case because the properties of ZnO NPs are strongly affected by vacuum ambient. Therefore, the potential barrier height was measured by CV method in this case. The CV measurement was performed by impedance spectroscopy at 120Hz. The imaginary impedance and $1/C^2$ at different reversed-bias voltages are shown in figure 3.30 below.

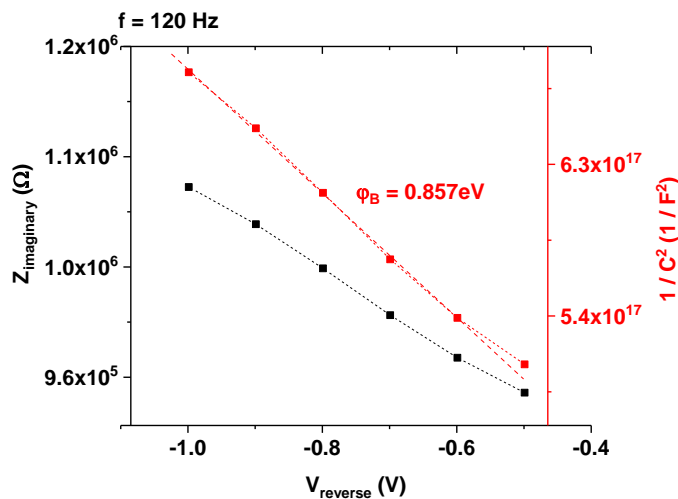


Figure 3.30 The imaginary impedance (black) and $1/C^2$ (red) at different reversed bias voltages.

The energy band diagram of the sample structure was shown in figure 3.28, based on the values from literature. The practical barrier height can be different from theoretical value because the actual ZnO NPs and PEDOT:PSS prepared in this case are different from the ideal ZnO and

PEDOT:PSS. In addition, the other factors also result in the difference such as the surface states from ZnO NPs and tunnelling effect. Figure 3.30 clearly shows that the imaginary impedance increases as the reversed-bias voltage increases due to an enhanced width in depletion region. The barrier height is determined by the intersection of $1/C^2$ with X axis and it is 0.857eV.

A full voltage scan was performed over -1V~1V, the result is shown below in figure 3.31:

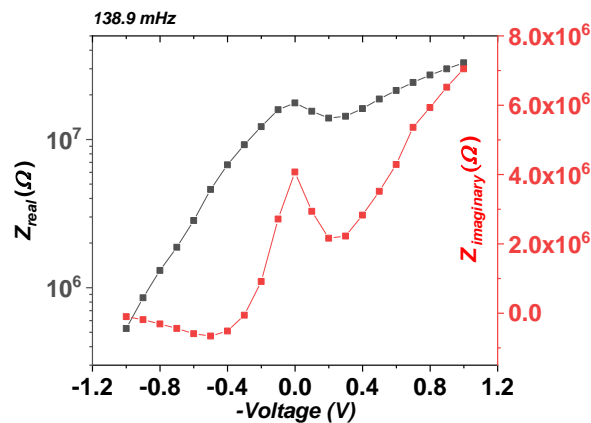


Figure 3.31 The real and imaginary impedance of heterojunction at -1V~1V.

It is evident that real impedance increases from -1V (forward bias) to 1V (reversed bias). There is a local peak at about 0V in imaginary impedance. This is highly possibly due to the existence of surface states or image force so that a second built-in potential exists near the surface and the direction of this electric field is opposite to that in the depletion region of the heterojunction. This was not investigated in detail. Moreover, it can be noticed that the imaginary impedance is negative at forward bias. This is related to the movement of ions in PEDOT:PSS and this is discussed in the following section.

- **Dielectric response**

The dielectric response of the heterojunction was carried out by impedance spectroscopy. The Bode plot and Nyquist plot for forward bias and reversed bias are plotted in figure 3.32 (a) and (b).

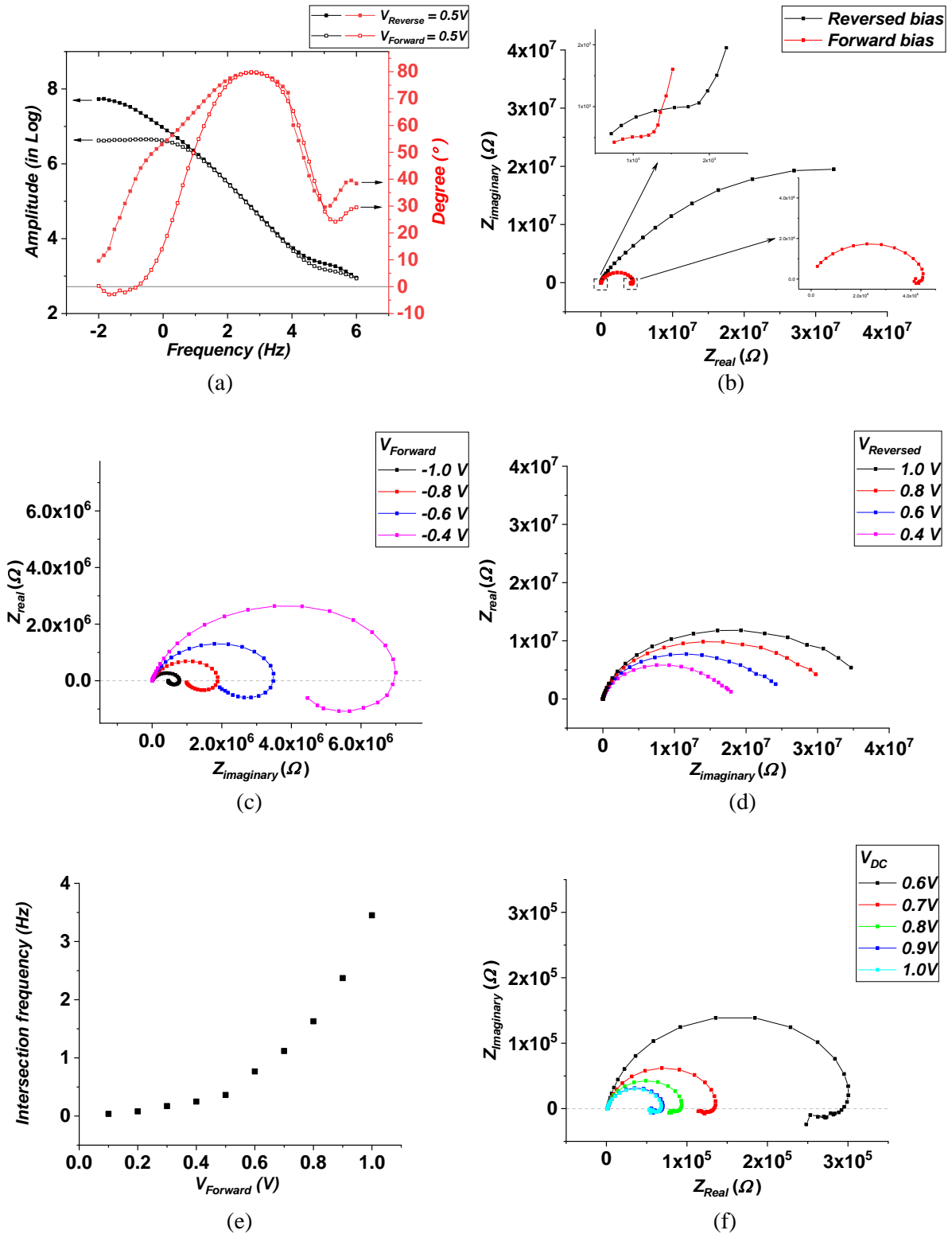


Figure 3.32 The (a) Bode plot and (b) Nyquist plot of the heterojunction under forward and reversed bias. The Nyquist plot under several (c) Forward bias and (d) Reversed bias voltages. (e) The intersection frequency under increasing forward bias voltages. (f) Pseudo-inductive behaviour.

It is evident that the main difference between forward and reversed bias is at low-frequency range (near DC). In addition, there is a pseudo-inductive behaviour under forward bias in the

low-frequency range (0.1Hz~0.01Hz). This is confirmed by the negative phase in the Bode plot in figure 3.32 (a) and negative semicircle in the Nyquist plot in figure 3.32 (b). This could be related to the movement of ionic species [111]–[114]. The associated ions species and ionic movement was not investigated further because this is less relevant to OASLMs. The Nyquist plot at different forward and reversed bias voltages are shown in figure 3.32 (c) and (d). It is clearly shown that the pseudo-inductive behaviour exists in the forward-bias condition only while it disappears under the reversed bias. The pseudo-inductive behaviour is generally related to the ionic movement and the change of sign indicates that the ions reach the boundary.

The frequency of the intersection points under different forward-bias voltages from figure 3.32 (c) are extracted, as is plotted in figure 3.32 (e). One thing to be noted is that the frequencies are estimated values since the impedance measurement was made only for limited and discrete frequencies. However, it can be seen that the frequency increases at higher forward bias voltage, indicating a shorter time for ions to reach the boundary.

Moreover, in order to verify the ionic movement in the PEDOT:PSS layer, the impedance spectroscopy was performed on an ITO-PEDOT:PSS-Al sample. The Nyquist plots are shown in figure 3.32 (f). It is convincing that the pseudo-inductive behaviour also exists.

- **Optical response**

The optical response the heterojunction and the heterojunction-based OASLMs were also studied. The UV response of ZnO NPs and the heterojunction is shown in figure 3.33 (a). The ZnO NPs sample was prepared in a sandwiched structure (ITO-ZnO NPs-Al) with an annealing temperature of 200°C (1h in air) so that the ZnO NPs are identical to that in the heterojunction. It is evident that the heterojunction had a larger On/Off current ratio of more than 60, compared to 2.1 of ZnO NPs. On the other hand, the fall time of the heterojunction is 11.4s (under reversed bias), compared to 32.8s of ZnO NPs. The response time of the sample improved by 2/3 after introducing PEDOT:PSS heterojunction. Therefore, it is convincing that the heterojunction is providing a better optical response in terms of on/off current ratio and switch-off speed.

The conductance of the heterojunction against increasing UV power is also plotted in figure 3.33 (b). The heterojunction can provide a larger responsivity if it is operated under reversed bias. This implies that the heterojunction under reversed bias is more sensitive to UV light.

The heterojunction was incorporated into the OASLMs and figure 3.33 (c) shows the intensity of the first-order diffraction pattern under different bias conductions. The OASLM was driven by a square wave in this case (0.5Hz) in order to keep the bias voltage constant. It is evident

that the signal remains constantly low under the forward bias while it shows high signal intensity under the reversed bias. This is because the heterojunction under forward bias has a large conductivity even without UV illumination so that the LCs are always switched on and the grating image is lost. On the contrary, the heterojunction under reversed bias has a large resistivity in the dark and it also has a large photosensitivity and photoconductivity. So, the signal received is distinctive under reversed bias. Figure 3.33 (d) presents the falling characteristic of the heterojunction-based OASLMs and the falling time is about 1.8s. This is a huge improvement compared to ZnO NPs-only OASLM (47.5s).

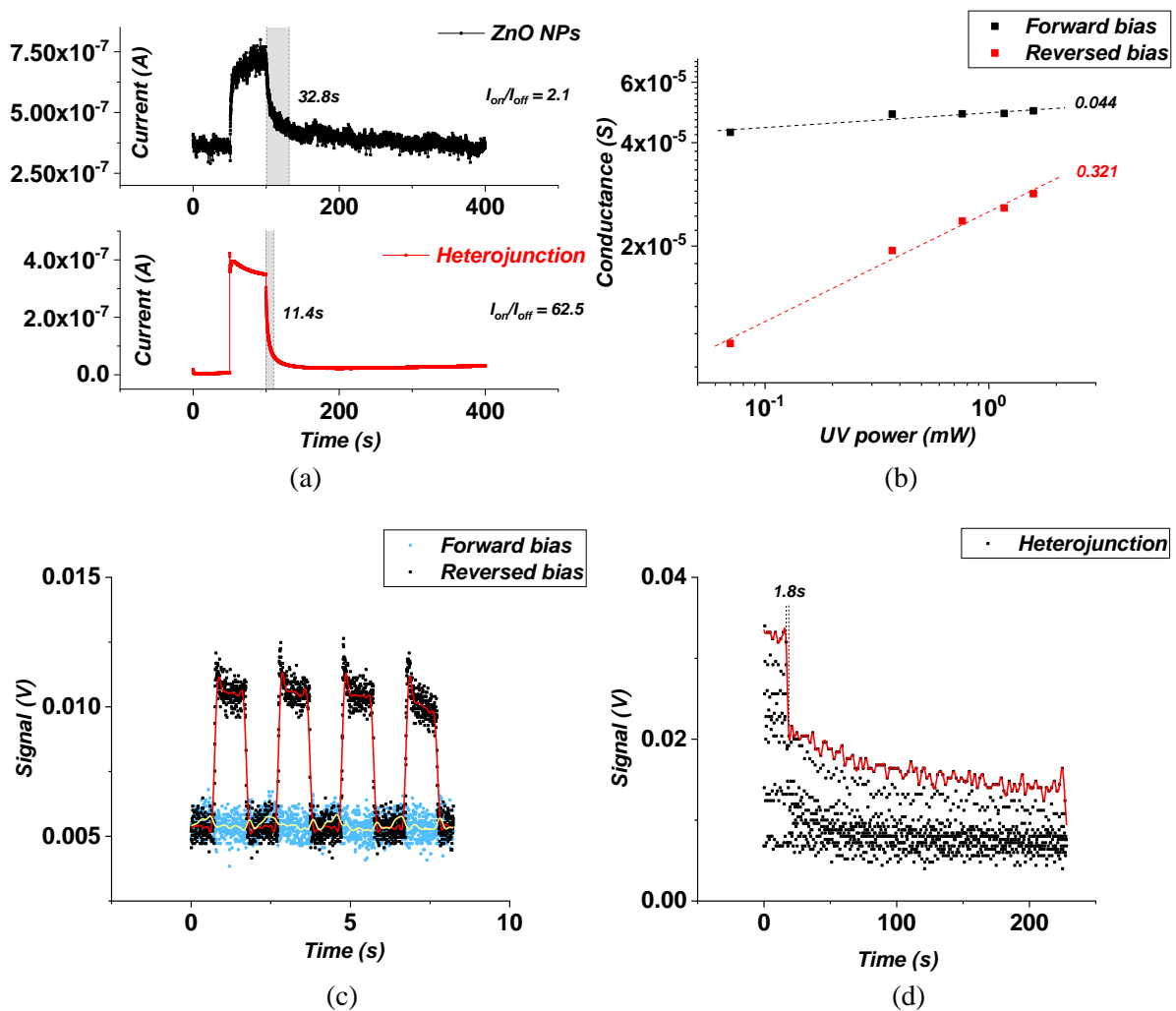


Figure 3.33 (a) The photo response of ZnO NPs and ZnO NPs - PEDOT:PSS heterojunction. (b) The photo conductance of ZnO NPs - PEDOT:PSS heterojunction at different bias conditions and light intensities. (c) The signal intensity of heterojunction-based OASLM. (d) The falling time of heterojunction-based OASLM after write light was off.

In summary, a photodiode structure has been used in OASLM and it was also experimentally proved that a shorter fall time of 1.8s can be achieved by photodiode-based OASLM. In the

meanwhile, photodiode structure can also provide a larger on/off current ratio compared to photoconductor processed under the same conditions. This chapter also characterized electrical properties of ZnO NP-PEDOT:PSS heterojunction and determined the barrier height of solution-processed heterojunction, indicating a good electrical rectification behaviour.

This chapter focuses on the optimization of ZnO NP-based OASLM in terms of resolution, diffraction efficiency and most importantly the response speed. Although the highest resolution has been achieved by ZnO NP-based OASLM, room for improvement still exists such as minimising the phase retardation (electrical fringing field) in LC layer and the lateral drift in ZnO layer, by selecting or tuning the material properties (elastic constants, dielectric anisotropy, trap states etc.). This was studied in detail by simulation. The diffraction efficiency was also optimized by determining the optimum driving signal (waveform, amplitude and frequency). In terms of the response time (fall time), three methods were used to enhance the response speed: raising the annealing temperature of ZnO NP, introducing a SiO₂ layer between LC and ZnO NP, and replacing the ZnO NP with ZnO NP-PEDOT:PSS heterojunction. It has been proved that the fall time was reduced by more than 10 times after optimization.

Chapter 4 ZnO NPs-based Sensor for Oxygen

Partial Pressure in Air

The sensitivity of ZnO NPs to oxygen partial pressure in air results from the adsorption and desorption of oxygen onto the surface of ZnO NPs, as was introduced in chapter 2. Adsorbed oxygen captures free electrons from ZnO NPs, forming a depleted ‘shell’ around ZnO NPs, as is shown in figure 4.1. Accordingly, the electrical conductivity of ZnO NPs decreases as oxygen adsorbs. Similarly, the decrease in oxygen partial pressure results in the desorption of oxygen species, releasing electrons and increasing the conductivity. In addition, ZnO NPs have a large surface-to-volume ratio, which enables a greater capacity for oxygen adsorption on ZnO NPs. So, ZnO NPs are advantageous for oxygen partial pressure sensing. Adsorbed oxygen can also be removed by UV illumination or heat and this could be used for sensor erasure (refreshing). Moreover, ZnO NPs are non-toxic to human cells and even shows antibacterial properties, which makes ZnO NPs-based sensors eco-friendly and suitable for bio-applications.

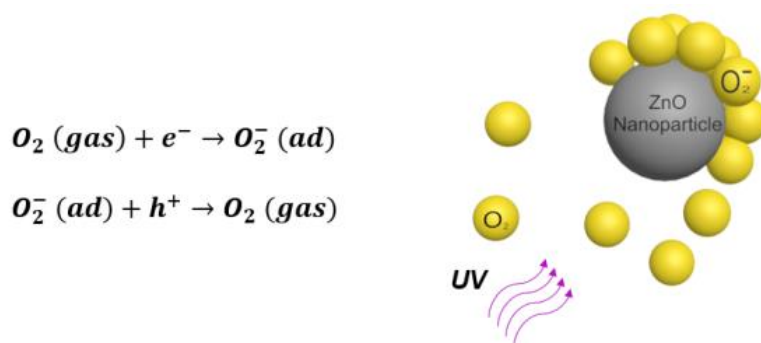


Figure 4.1 Oxygen adsorption and desorption on ZnO NPs.

This chapter mainly focuses on the behaviour of ZnO NPs in the low-pressure ambient. Then the fabrication and characterization of ZnO NPs-based oxygen partial pressure sensor are introduced. Moreover, the patterning of nanoscale ZnO NPs lines and their sensing behaviour are discussed in the end.

4.1 Oxygen Partial Pressure Effect

The electrical properties of ZnO NPs in vacuum was measured, as is shown in figure 4.2 below. In order to amplify the effect of oxygen partial pressure, high-concentration ZnO NPs suspension (1150mg/ml in ethanol) was used to fabricate the sample. A sandwiched structure (Al-ZnO NPs-ITO) was used. The ZnO NPs layer was formed by spin-coating and it was

annealed at 400°C in air for 3h. Al electrodes were deposited by thermal evaporation. The vacuum ambient was achieved by the roughing pump and turbo pump, and the minimum pressure was 10⁻⁵ mBar.

Figure 4.2 (a) demonstrates the I-V characteristics of ZnO NPs in vacuum, which shows a linear relationship below 2.6V, indicating the Ohmic conduction mechanism (the slope is 1.09). The field effect of ZnO NPs in vacuum was also investigated, as is shown in figure 4.2 (b). The sample was fabricated in a planar structure.

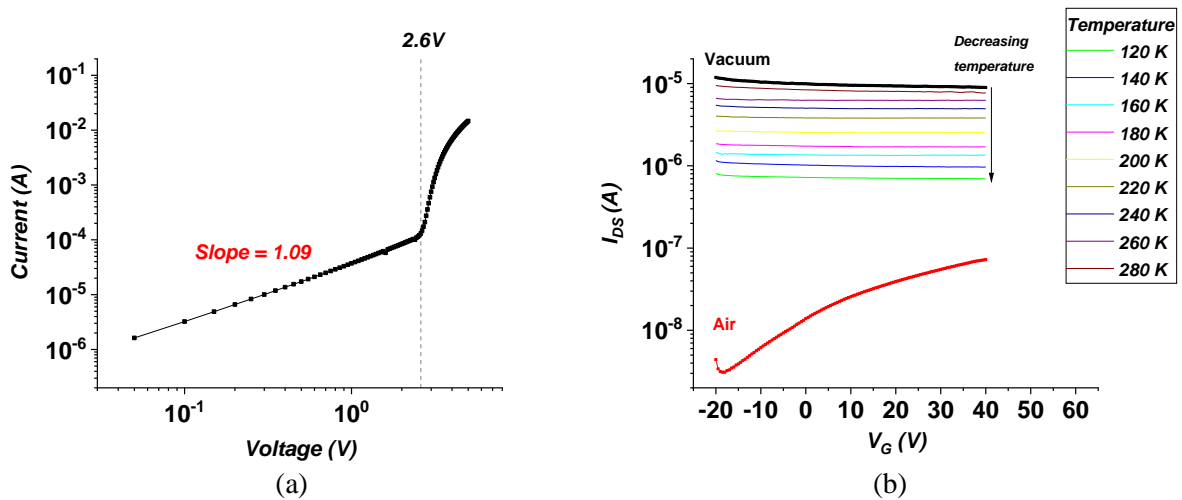


Figure 4.2 (a) I-V characteristics of ZnO NPs in vacuum. (b) Field effect of ZnO NPs under different measuring conditions.

It is evident that the field effect exists when ZnO NPs are in air while the field effect disappears when they are in vacuum. This is also because of the oxygen desorption in vacuum, which removes the depletion layer around ZnO NPs and enhances the electrical conductivity. As a result, the gate has little effect on the conduction between drain and source (like short circuit). In contrast, oxygen adsorbs and captures free electrons when ZnO NPs are in air, giving rise to the gate-controlled field effect. Figure 4.2 (b) also shows the low-temperature I-V characteristics (in vacuum) and the current decreases when the measuring temperature drops because of decreasing charge carrier mobility and density.

4.2 Sensor Fabrication and Characterization

An oxygen partial pressure sensor with heat-erasing capability was fabricated and the structure of the sensor is shown in figure 4.3 below. A layer of photoresist was patterned into a hollow rectangular shape by photolithography on a silicon substrate as a protector layer for etching. And the substrate was then etched by Reactive Ion Etching (RIE) with SF₆ to form a platform

in the centre. This platform was designed to confine the generated heat (for erasing) in the target area. A thin layer of chromium (100nm) was deposited by E-beam evaporation. Cr was used because it has a relatively large resistivity (125 nΩ·m at 20°C) compared to other metals. So, Cr is an effective material for power heat. Cr was patterned like a ‘bottleneck’ so that the Cr layer could generate a massive amount of heat in a very short period on the etched platform. A thin layer of SiO₂ (100nm) was further deposited by E-beam evaporation to electrically isolate Cr. Then ZnO nanoparticles dispersion was spin-coated on the platform and annealed at 400°C in air for 3hours. Finally, Al electrode (100nm) was deposited by thermal evaporation. A current source was connected to Cr to generate heat.

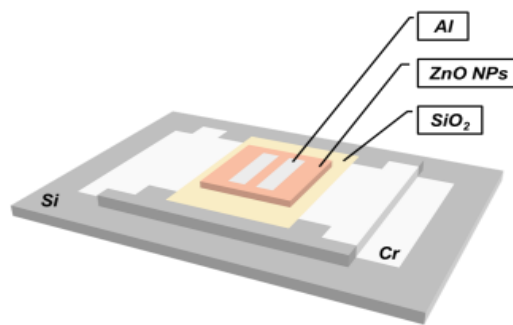


Figure 4.3 The structure of ZnO NPs-based oxygen sensor.

The electrical conductance of ZnO NPs under different pressure was measured by a probe station in a vacuum chamber, as is shown in figure 4.4 (a).

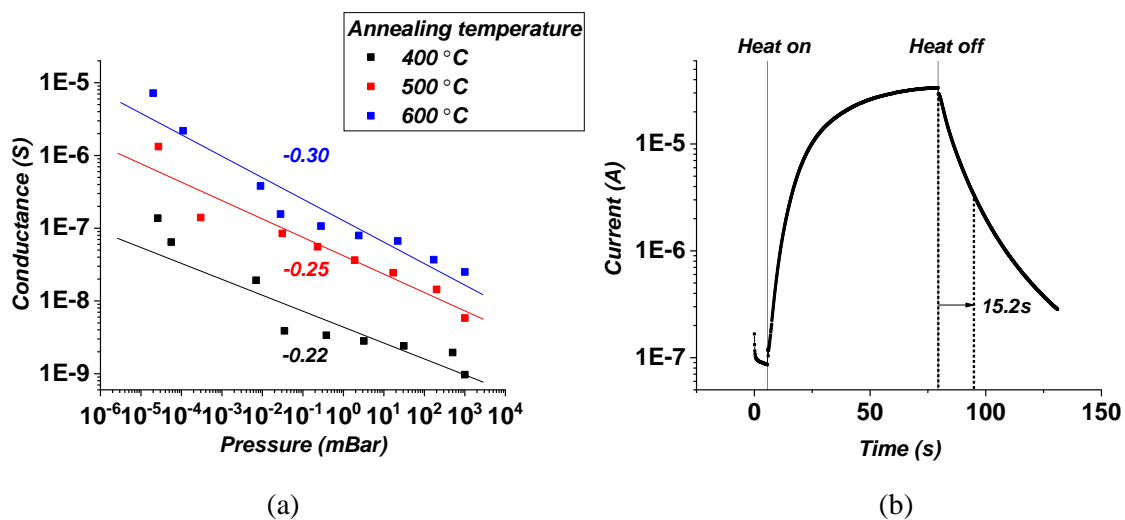


Figure 4.4 (a) The conductance of ZnO NPs under different air pressure. (b) The electrical response to the erasing heat.

The pressure in the chamber can be controlled within the range from 10⁻⁵mBar to 10³mBar. And the corresponding change in conductivity is more than 100. Figure 4.4 (a) also shows the

pressure-dependent conductance of ZnO NPs annealed at different temperatures (400°C, 500°C and 600°C in air for 3h).

The relationship between oxygen partial pressure (P_{O_2}) and electrical conductivity (σ) is defined by equation 4.1:

$$\sigma = A \exp\left(-\frac{E_a}{kT}\right) P_{O_2}^m \quad (4.1)$$

where E_a is the trap activation energy and A is a constant.

The power index m is normally used to quantitatively describe the sensitivity to oxygen partial pressure and it is dependent on the charge carrier type and defects. It can be extracted by the slope of $\log(\sigma) \sim P_{O_2}$, and it is clear that the index m is -0.22 for ZnO NPs annealed at 400°C. Furthermore, it is evident that the absolute value of power index $|m|$ increases at higher annealing temperature. The highest power index of 0.3 is achieved at 600°C, indicating the best sensitivity of ZnO NPs to oxygen partial pressure. On one side, higher annealing temperature improves the purity by removing organic surfactants, providing larger capacity for oxygen adsorption. On the other side, greater number of free electrons are generated at higher annealing temperature because of the shallower trap states, which also leads to a larger capacity for adsorbed oxygen. Accordingly, a larger number of pressure-induced electrons are released, and a larger sensitivity is obtained. In conclusion, a better sensitivity to air pressure can be realized by raising annealing temperature. This is a valuable and practical conclusion for high-sensitivity oxygen partial pressure sensors.

Figure 4.4 (b) shows the heat erasing feature of the sensor. The current surges dramatically once the power heat (Cr) is on because electrons from the valence band and adsorbed oxygen are excited by thermal energy, becoming free electrons and contributing to the current. Current drops after the heat is off and the 'off' time is about 15.2s.

4.3 Miniaturized Oxygen Sensor

The demand for miniaturized sensors is increasingly high nowadays in integrated applications since they have lower cost in material, less power consumption and better space utilization. The size of ZnO NPs-based oxygen sensor can be minimized by patterning ZnO NPs into small features. ZnO NPs lines were fabricated by two approaches: photolithography and mould-guided drying.

Photolithography is a traditional patterning method, which has been widely used in the fabrication of integrated circuits. Similar to the standard photolithography process, photoresist (AZ5214) was spin-coated on ZnO NPs film. The ZnO NPs film was prepared on a silicon substrate by spin-coating and the film was annealed at 400°C in air for 3h. A line mask was used to form protective lines on top of ZnO NPs. After exposing and developing, ZnO NPs film was immersed in diluted HCl acid (0.5% in DI water) for 2s to remove the unprotected ZnO NPs. Finally, the photoresist was removed by acetone. The optical image and SEM image of the patterned ZnO NPs lines are shown in figure 4.5 below. The average width of ZnO NPs lines are about 7µm. However, the edges of ZnO NPs lines show variations due to the wet etching. The contact between ZnO NPs and silicon substrate is not sufficient (only the boundaries of NPs) so HCl could easily penetrate into protected ZnO NPs, causing various line widths.

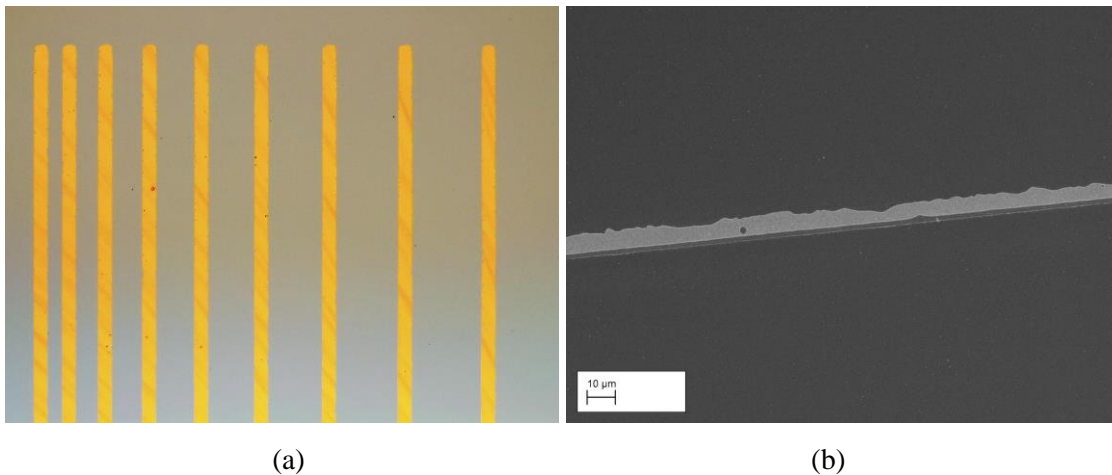
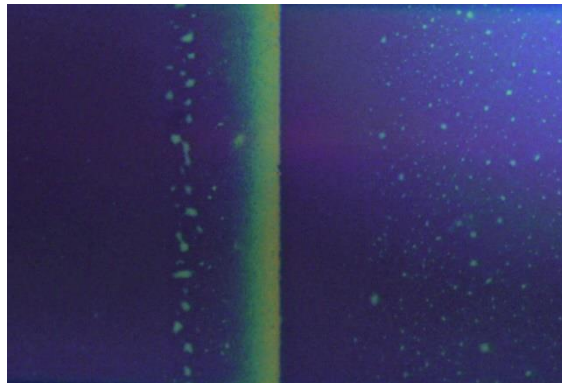
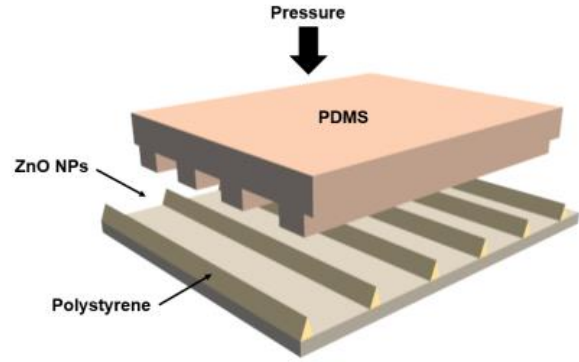


Figure 4.5 The ZnO NPs lines fabricated by photolithography, observed by (a) Optical microscope and (b) SEM.

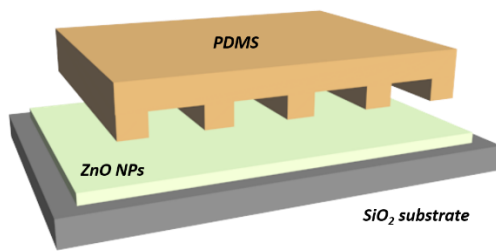
Another method to pattern ZnO NPs is mould-guided drying. Mould-guided drying technique is extremely suitable for the patterning of solution-processable materials into lines. In addition, it is low in cost, reproducible and efficient for large-scale fabrication. The production process has been introduced in chapter 1. However, the direct patterning using mould-guided drying is not suitable for NPs because NPs could stay in the contact area between the stamp and substrate, leaving NPs residuals, as is shown in figure 4.6 (a). Therefore, two approaches were used to optimize this process.



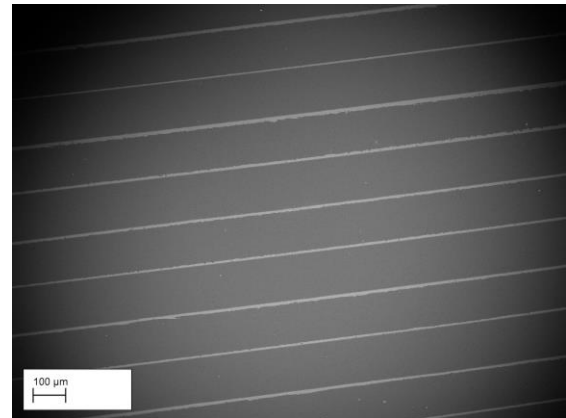
(a)



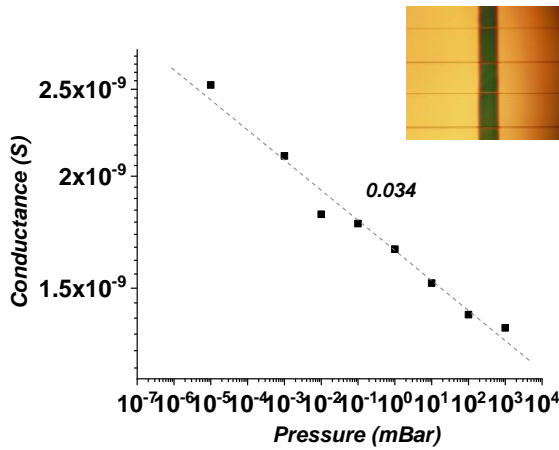
(b)



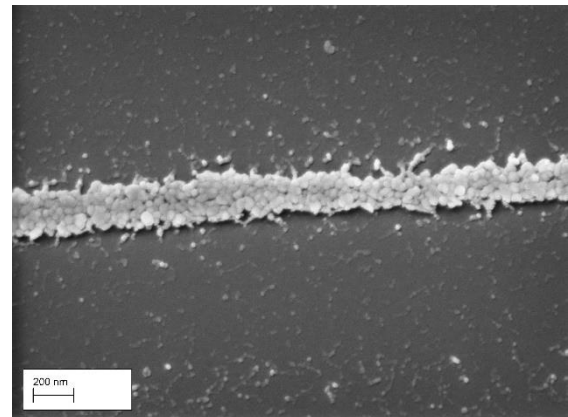
(c)



(d)



(e)



(f)

Figure 4.6 (a) ZnO NPs lines by direct stamping. (b) The fabrication of ZnO NPs lines by PS ‘spacer’. (c) Patterning PS lines on top of ZnO NPs film. (d) SEM image of ZnO NPs lines. (e) The oxygen sensing performance of ZnO NPs lines. (f) The minimal line width achieved.

The first method is to use another material (Polystyrene in this case) as spacer between the stamp and substrate, so that NPs are not trapped by the contact. Firstly, lines of polystyrene (PS)

were fabricated using the mould-guided drying technique from PS solutions in 1,2-dichlorobenzene (DCB, 0.4 mg/ml). Then ZnO NPs lines were formed in the orthogonal direction, as is shown in figure 4.6 (b). This method is good to fabricate segments of ZnO NPs lines and the length of ZnO NPs lines is determined by the gap between PS lines.

In order to pattern continuous and long ZnO NPs lines, PS lines were patterned on top of ZnO NPs as protective lines by mould-guided drying. To be more specific, a layer of ZnO NPs thin film was firstly spin-coated on a substrate, followed by thermal annealing in air at 400°C for 3h. Next, polystyrene (PS) lines were formed on top of ZnO NPs film by mould-guided drying, as is shown in figure 4.6 (c). PS lines were then annealed in air at 100°C for 1h. The sample was immersed in diluted hydrochloric acid (HCl, 0.5%) for 2s to remove the uncovered ZnO NPs. Finally, the sample was treated in oxygen plasma for 5min to remove the PS. As a result, the PS pattern was transferred to ZnO NPs and the finished ZnO NPs lines are shown in figure 4.6 (d). The line width is between 6~7µm.

Furthermore, the oxygen sensing properties of ZnO NPs lines was measured by depositing Al electrodes on top, and the result is shown in figure 4.6 (e). The inset image shows the ZnO NPs lines formed between Al electrodes. It is clear that the electrical conductance of ZnO NPs lines increases as the pressure drops. The slope of $\log(\sigma) \sim P_{O_2}$ is 0.034 which is much smaller than that of ZnO NPs thin films (0.22). This is due to the smaller number of NPs in lines compared to thin films, which results in a weaker capacity for adsorbed oxygen and thus smaller responsivity.

Thinner ZnO NPs lines are also achievable by thinning the width of PS lines. Nanosized ZnO NPs lines can be obtained by reducing the concentration of PS solution. Figure 4.6 (f) demonstrates the nanoscale ZnO NPs lines and the line width is less than 190nm. Nanopatterning of ZnO nanoparticles makes it suitable for miniaturized and integrated systems. Besides the low power consumption, integrated gas sensors offer low signal-to-noise ratio, therefore making them particularly attractive in biomedical and electronic devices.

ZnO NPs were removed by wet etching in all the methods mentioned above. Wet etching is fast and effective. However, the etched edges are not uniform and ZnO NPs lines are susceptible to fall off the substrate, especially in the case of small line width. Therefore, dry etching by Reactive Ions Etching (RIE) is recommended for higher-resolution patterning.

The mould-guided drying technique was also used for various solution-processable materials. For instance, indium oxide (In₂O₃) lines were also patterned from its solution in 2-

Methoxyethonal (2-Me). The patterned In_2O_3 lines were further annealed in air at 200°C for 1h to remove the solvent and Al electrodes were deposited as electrodes. The In_2O_3 lines and electrical characteristics are shown below in figure 4.7 (a)~(c). The linewidth is about $1.64\mu\text{m}$ and the spacing is $126.29\mu\text{m}$.

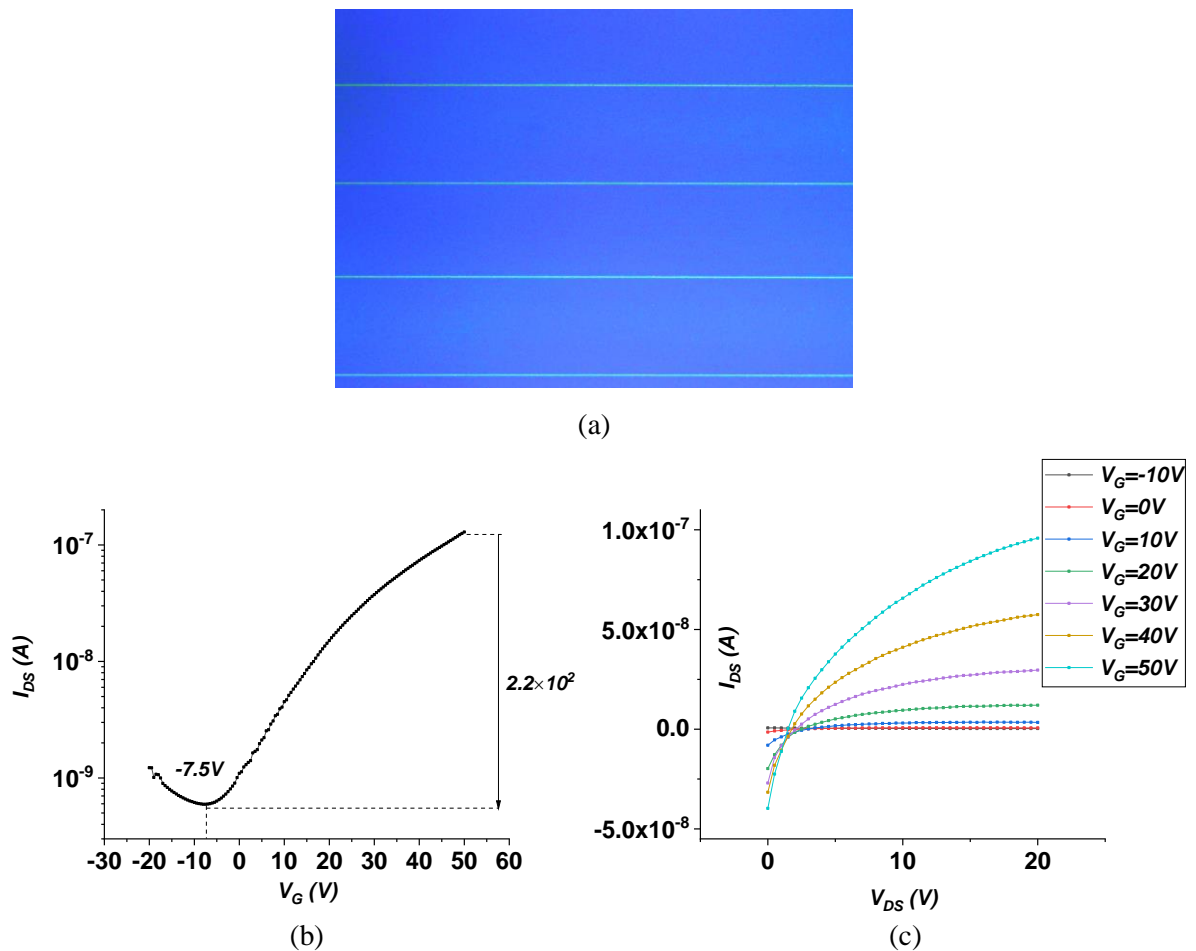


Figure 4.7 (a) In_2O_3 lines under optical microscope. The (b) Transfer function and (c) Output function of In_2O_3 lines transistor.

The transfer function of In_2O_3 lines transistor shows that the turn-on voltage is about -7.5V and the on/off current ratio is more than 220. This opens the door for the nanofabrication of IGZO-based transistors and it also shows a promising future for miniaturized applications with low-cost and large-scale fabrication processes.

Moreover, polymeric conductor PEDOT:PSS was successfully patterned into micro- and even nano-scale lines, which were used in organic electrochemical transistors (OECTs). The detailed fabrication process and its characterization are discussed in the following chapter.

Chapter 5 High-Resolution Patterning of PEDOT:PSS and PEDOT:PSS-based Organic Electrochemical Transistors (OECTs)

The patterning of ZnO NPs by photolithography and mould-guided drying has been demonstrated in the previous chapter. The mould-guided drying technique has displayed a great potential for solution-processable materials. In fact, not only is this technique suitable for metal-oxide materials, but it is also attractive to organic functional materials. The patterning of organic materials with traditional methods has been very challenging compared to the patterning of inorganic materials due to the potential contamination, chemical reaction and degradation during the process. Therefore, new approaches to pattern organic materials are demanded. In this chapter, mould-guided drying is used to pattern PEDOT:PSS, an attractive and promising organic conductor.

Various patterning techniques for PEDOT:PSS have been reported such as spin-coating, photolithography, dry etching, laser ablation, inkjet printing and roll-to-roll printing [115]–[117]. Direct spin-coating of PEDOT:PSS is difficult since Si or SiO₂ substrate is hydrophobic. This is generally solved by oxygen plasma treatment or adding hydrophilic additives (Triton). Dry etching is normally achieved by Reactive Ion Etching (RIE), where oxygen, argon or fluorinated gases are used to chemically and physically etch PEDOT:PSS. Photolithography is not suitable for PEDOT:PSS patterning, because chemical reactions exist between acidic PEDOT:PSS and photoresist [118].

In this chapter, PEDOT:PSS from its water suspension was patterned by mould-guided drying technique. Furthermore, the organic electrochemical transistors (OECTs) based on the patterned PEDOT:PSS and NaCl solution were fabricated and characterized. More importantly, the advantage and advance of this patterning technique was reflected by the nanoscale feature achieved, and OECTs with nanoscale channel width and length were successfully fabricated. Nanosized OECTs are undoubtedly captivating since high-resolution detection, low power consumption and integrated devices can be realized. In particular, nanoscale OECTs have a bright future in synaptic transistors for neuromorphic computing [119].

5.1 Electrical Properties of PEDOT:PSS Thin Film

The electrical conduction mechanism in PEDOT:PSS has not been fully understood yet. Some researchers claimed that PEDOT:PSS is composed by conductive PEDOT-rich grains (20nm~70nm in diameter) [120] and insulating PSS-rich boundaries (weak ionic conduction) [121]. Therefore, the electrical conduction is ascribed to the hole transport in PEDOT polymers and charge hopping between PEDOT and PSS. The conductivity is represented by the following equation [120]–[122]:

$$\sigma = \sigma_0 \exp\left[-\left(\frac{T_0}{T}\right)^\alpha\right] \quad (5.1)$$

where σ_0 is a constant and T_0 indicates the potential barrier height of thermally activated charge hopping. The power index α is dependent on the type of charge transport. A range of α values (0.25~1) has been reported (1 for lateral and normal conduction) [122]. The typical α value of 0.25 was ascribed to variable range hopping (VRH) conduction [120]–[122]. Others also proposed the value of 0.5, representing the Coulomb interaction between the charges or the tunnelling between PEDOT grains [121], [122]. For solution-processed PEDOT:PSS thin films, electrical conduction is anisotropic (3 order of difference was reported [120]). Lateral and normal conduction are attributed to variable range hopping (VRH) and nearest-neighbour hopping respectively. Therefore, lateral conduction shows a larger conductivity while normal conduction has a much smaller conductivity.

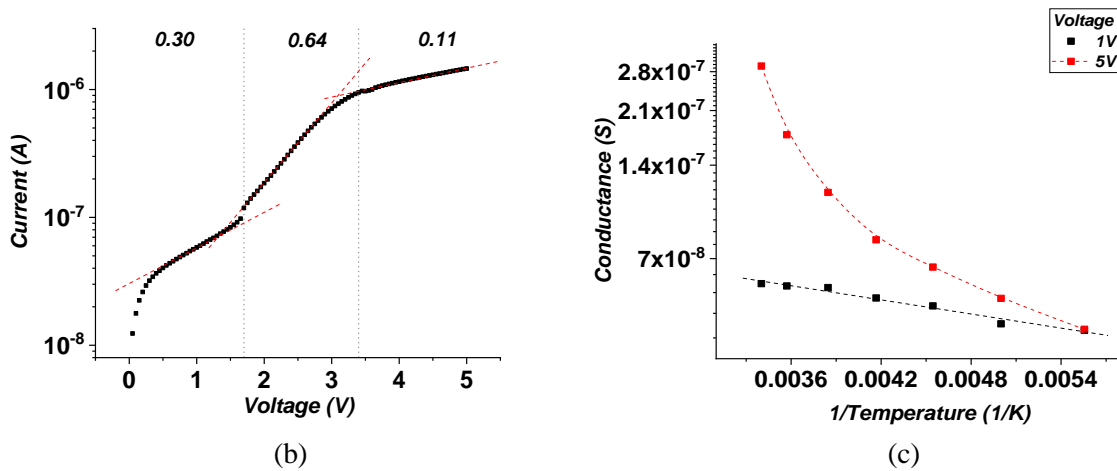
I-V measurement was conducted for PEDOT:PSS thin films. The PEDOT:PSS thin film was formed by spin-coating from its water dispersion on a SiO₂ substrate with pre-deposited Al electrodes (85 μ m channel length), as is shown in figure 5.1 (a). The substrate was then annealed in air at 200°C for 1h to remove the solvent. The relation between ln(I)~V is plotted in figure 5.1 (b). The slope of ln(I)~V plot is related to the hopping distance according to the definition of hopping conduction. It can be seen from figure 5.1 (b) that the hopping distance varies in different voltage ranges.

This was further investigated by low-temperature I-V measurement as is shown in figure 5.1 (c). It is evident that the conductance at 1V (in log scale) shows a linear relationship with 1/T. This confirms that the power index α is 1, indicating the nearest-neighbour hopping conduction [120]. The Arrhenius-type relationship represents the thermally activated process so T_0 in this case represents the energy barrier height between intersites. The value of activation energy is extracted by the slope and it is calculated to be 6.55meV. The conductance at 5V (red) is rather complicated. Figure 5.1 (c) shows a linear relationship between conductance (log) and 1/T at

high measuring temperatures while it has a low-order relationship at lower temperatures. This could be the result of variable-range hopping (VRH). VRH conduction is to describe the charge transport in disordered semiconductor system.



(a)



(b)

(c)

Figure 5.1 (a) The planar structure of Al-PEDOT:PSS-Al sample. (b) I-V characteristics of PEDOT:PSS. (c) Low-temperature conductance of PEDOT:PSS.

The dielectric properties of PEDOT:PSS thin film was also studied using impedance spectroscopy. The Bode plot and Nyquist plot are shown below in figure 5.2 (a) and (b). The impedance spectroscopy was measured under 1V. It is clear from figure 5.2 that there are more than two polarization mechanisms in PEDOT:PSS and they have overlapped peaks in the Bode plot and overlapped semicircles in the Nyquist plot. Further approaches need to be taken to distinguish these mechanisms.

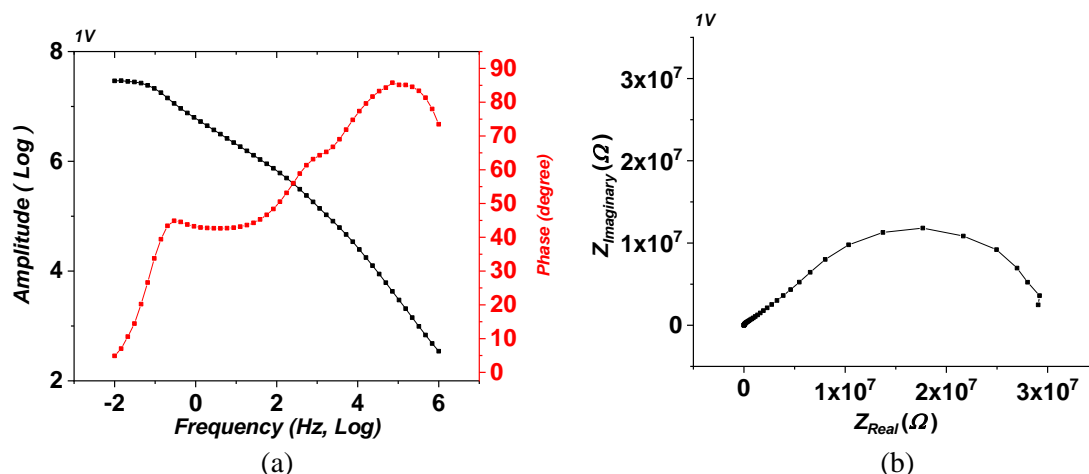


Figure 5.2 The (a) Bode plot and (b) Nyquist plot of PEDOT:PSS.

The investigation of electrical conduction mechanism at high voltage and polarization mechanisms were not proceeded in this work since they are not significant in the application of OECTs. However, they are interesting topics for future research.

5.2 The Patterning of PEDOT:PSS Lines

Various techniques have been used to pattern PEDOT:PSS such as mask etching, soft-lithography, nanoimprint, pulsed laser ablation and direct UV-patterning etc. These patterning techniques are generally associated with high power consumption (UV and plasma) and limited by insufficient resolution. Two patterning methods were attempted in this chapter: photolithography and mould-guided drying. Both techniques are based on the post-processing of PEDOT:PSS thin films. The film was formed by spin-coating PEDOT:PSS water dispersion on SiO₂. Triton was added into the dispersion beforehand in order to increase the adhesion to SiO₂ substrate. In addition, the patterned lines were characterized in terms of the electrical and optical anisotropy.

5.2.1 The patterning process

Traditional photolithography was firstly attempted. A substrate with pre-deposited Al electrodes was treated with oxygen plasma for 1min and PEDOT:PSS water dispersion was spin-coated on the SiO₂ substrate (4000RPM for 30s). Then the sample was annealed in air at 200°C for 1h to remove the solvent and to increase adhesion to the substrate. Higher annealing temperature could result in the degradation of PEDOT:PSS [123]. The sample is shown in figure 5.3 (a).

Photolithography was carried out after spin-coating photoresist (AZ5214E) on top of PEDOT:PSS thin film, leaving a 10 μ m gap between PEDOT:PSS and Al. One thing to be noted is that the baking time before UV exposure was reduced to 1min in order to reduce the connection between PEDOT:PSS and photoresist. After UV exposure, the sample was rinsed in the developer and treated with low-power oxygen plasma (avoid high-power annealing) to remove the unprotected PEDOT:PSS. Eventually the sample was immersed in Acetone for 1min to remove the photoresist and the result is shown in figure 5.3 (b).

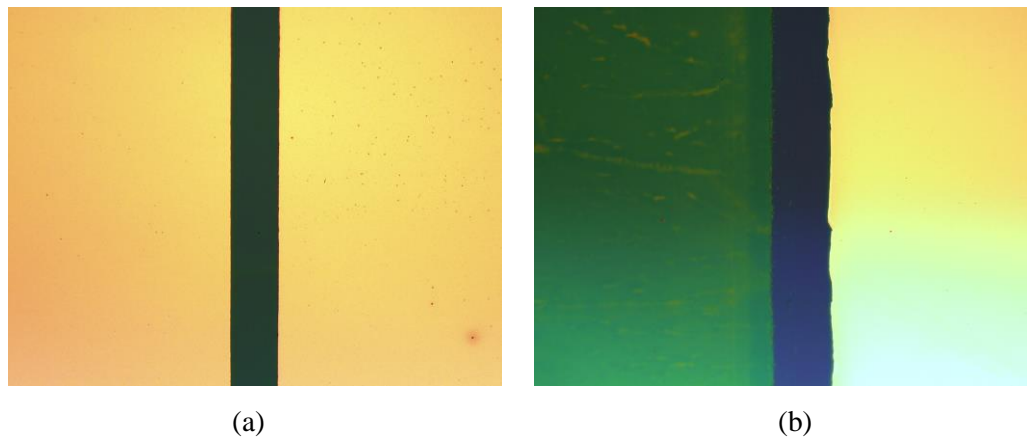


Figure 5.3 (a) The PEDOT:PSS thin film formed on the SiO₂ substrate. (b) A gap between PEDOT:PSS and Al was created by photolithography.

However, it was also noticed that PEDOT:PSS after annealing still had a certain solubility in Acetone and this resulted in residual PEDOT:PSS in the gap. Therefore, photolithography is not a good method for PEDOT:PSS patterning, especially for electrical applications.

The second approach is the mould-guided drying method, which possesses high resolution, inexpensive cost and applicability to a range of situations, which are not suitable by conventional lithography technologies since material could be damaged by UV irradiation and chemical reactions. The fabrication process has been introduced in chapter 1. To be more specific, a small amount of PEDOT:PSS suspension ($\sim 3\mu$ L) was drop-casted onto the surface of polydimethylsiloxane (PDMS) mould ($\sim 1\text{cm}^2$) with pre-defined patterns. Then, a SiO₂ substrate was gently brought into contact with the PDMS mould by a designed clamp under a small applied pressure (about 5 MPa). The clamp was left in air at room temperature for 4 hours. After the solution completely dried out, PDMS mould was removed from SiO₂ substrate, leaving the patterned PEDOT:PSS lines on the substrate. The depth of the grooves on the PDMS mould was 1.5 μ m. In addition, 20% ethylene glycol was added into the PEDOT:PSS suspension to improve the conductivity. Triton X-100 (0.92mg/mL) was also added to modify the surface

tension of the solution and to make the solution hydrophilic. The pattern quality is particularly sensitive to the amount of Triton X-100 added to the solution. It was also found that a high-quality pattern was obtained when 0.92mg/mL of Triton X-100 was added. Insufficient amount of Triton resulted in the line discontinuity due to the high surface tension of the liquid, while higher concentrations of Triton often caused residual PEDOT:PSS between the patterned lines. The line width was dependent on the solution concentration.

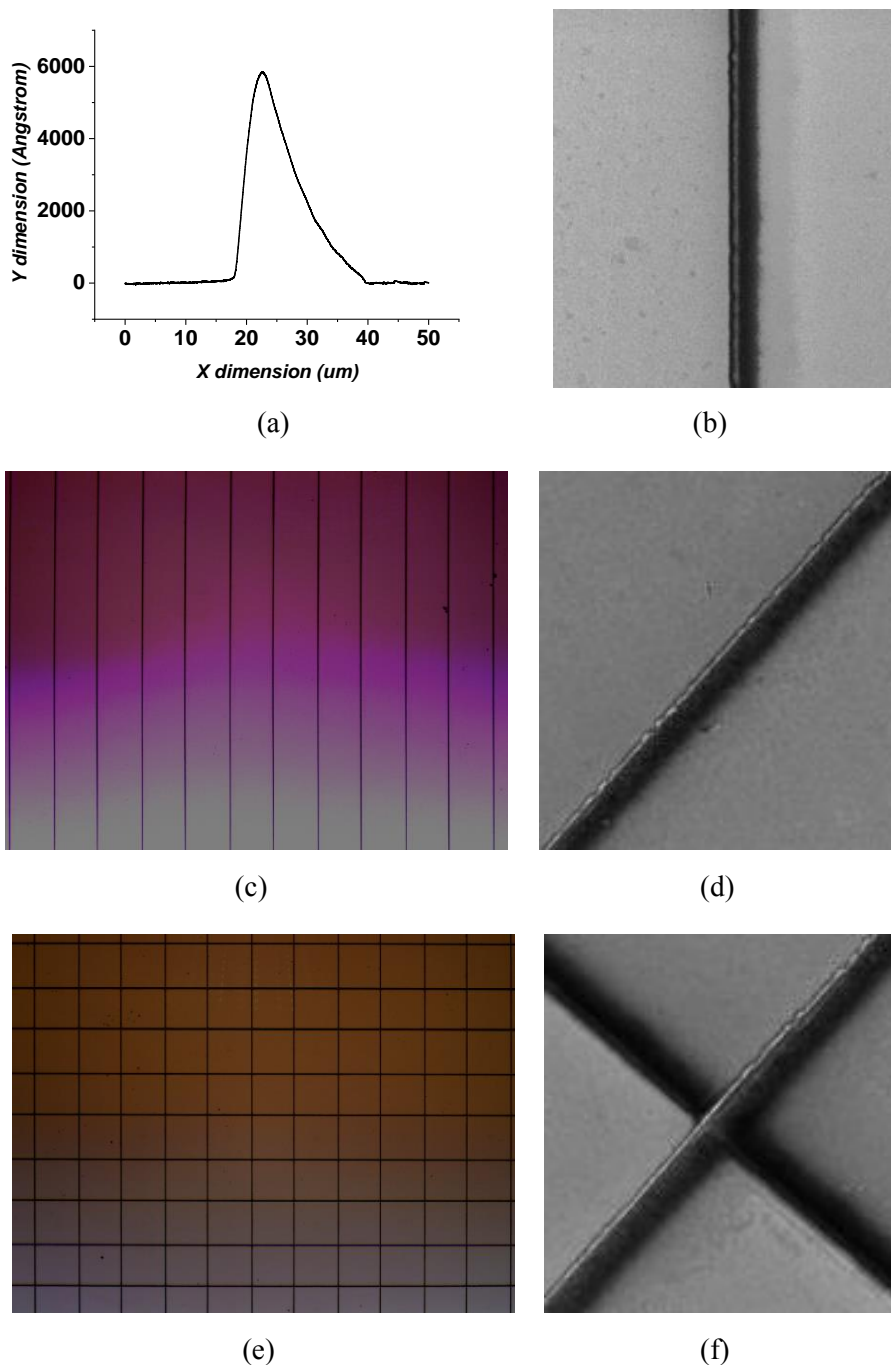


Figure 5.4 The (a) Cross-section profile and (b) SEM image of a single PEDOT:PSS line. (c) PEDOT:PSS lines and (d) SEM image. (e) PEDOT:PSS grid and (f) SEM image.

As the solvent evaporated, capillarity bridges of PEDOT:PSS were formed and pinned by the stamp grooves. As a result, thin PEDOT:PSS lines were subsequently formed next to the groove. Figure 5.4 (a) and (b) shows the cross-section and the SEM image of one single PEDOT:PSS line. The cross-section was obtained by a profiler and the profile clearly confirms the triangle-like shape.

The patterned PEDOT:PSS lines are shown in figure 5.4 (c) and (d). The linewidth was measured to be 700nm. The PEDOT:PSS grid was also patterned by consecutive patterning in orthogonal directions and the grid is shown in figure 5.4 (e) and (f).

5.2.2 Optical and electrical anisotropy of the patterned PEDOT:PSS lines

Mould-guided drying of polymer solutions can result in polymeric alignment along the grooves during the drying process. This was confirmed by polarized UV-visible absorption spectroscopy and electrical conductivity measurements. In polarized UV-Vis spectroscopy, maximum absorption is expected when the transition dipole moments of polymers are parallel to the electrical polarization direction of light since the transition dipole moment components of conjugated polymers are oriented in the direction along the polymer backbone. Figure 5.5 (a) shows the absorbance anisotropy of the fabricated PEDOT:PSS lines. Larger absorbance was observed when the direction of PEDOT:PSS lines was oriented parallel to the light polarization direction which indicates that the PEDOT chains are aligned in the fabricated line direction. This is reasonable since polymer chains tend to align with the grooves in order to have minimum internal energy.

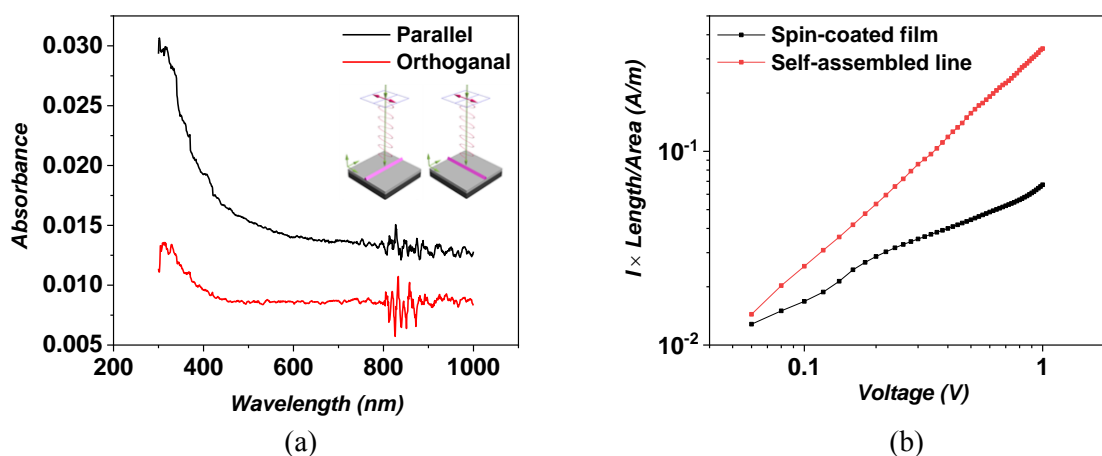


Figure 5.5 (a) Optical anisotropy. (b) Electrical conductivity of PEDOT:PSS thin film and lines.

The electrical conductivity of spin-coated PEDOT:PSS thin film and the patterned PEDOT:PSS lines with identical post thermal treatment (140°C for 1 hour) further confirmed this. The conductivity (σ) of PEDOT:PSS is defined by the following equation:

$$I \times \frac{L}{A} = V \times \sigma \quad (5.2)$$

where L and A are the conductive length and cross-section area of PEDOT:PSS respectively. So, the conductivity can be reflected by the slope of $I \times \frac{L}{A} \sim V$ plot. The conductivity anisotropy ratio (CAR) is defined here by $\sigma_{\text{line}}/\sigma_{\text{film}}$, where σ_{line} and σ_{film} are the conductivity of the PEDOT:PSS lines and film respectively. Figure 5.5 (b) shows the electric conductivity of the two samples. The CAR can reach $\sigma_{\text{line}}/\sigma_{\text{film}} = 2.05$, which indicates a better conductivity along the PEDOT chains.

5.3 Organic Electrochemical Transistors (OECTs) Based on the Patterned PEDOT:PSS Lines

Organic Electrochemical Transistors (OECTs) have captured numerous attentions during the last decade due to the synthetic tunability, bio-compatibility and easy fabrication. In addition, OECTs can achieve large modulations of current by low voltages as the doping process affects the whole volume of OECTs, compared to the interface of field effect transistors (FETs). OECTs have been used in a wide range of applications such as bioelectronic sensors, circuits requiring high transconductance and memory devices for neuro-systems [124]. Moreover, ion-based synaptic transistors with a proper dopant in the active layer could generate reprogrammable multiple stable conduction states which is promising for the next generation neuromorphic computing.

The typical structure of an OECT is shown below in figure 5.6. The organic film (PEDOT:PSS in this case) is deposited on a SiO_2 substrate with aluminium (Al) electrodes (drain and source). Organic film is immersed in electrolyte (NaCl in this case) and silver (Ag) is also immersed from the top as the gate electrode. The operation of OECTs is based on the doping and de-doping (depletion) of organic materials by the ions from electrolyte, which directly determines the conductivity of organic channel. Choosing Ag as the gate material is because the interfacial voltage drop between Ag and electrolyte is negligible, providing an effective gating across the electrolyte. In comparison, electrical double layer will be formed around the gate if gold (Au) or platinum (Pt) is used.

OECTs are generally operated in two modes. Depletion mode relies on the de-doping effect (become resistive) once a positive gate voltage is applied while accumulation mode is based on the doping process (become conductive) under a negative gate voltage.

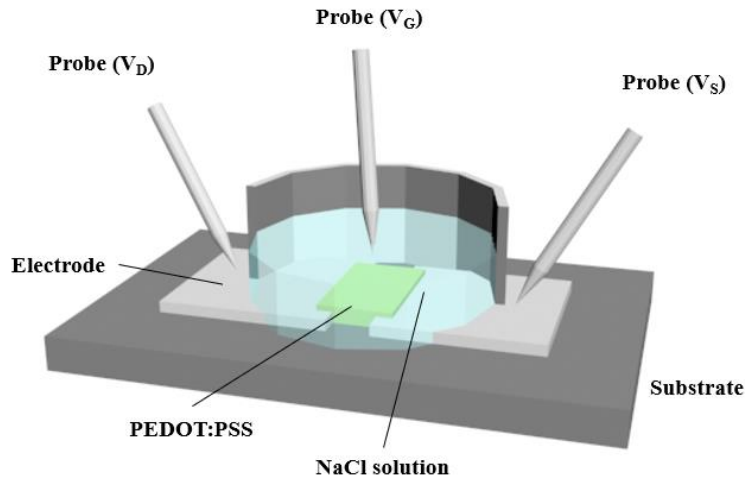


Figure 5.6 Structure of OECT.

However, OECTs have slow response, mainly due to the ionic conduction in the electrolyte [124]. Fast response can be achieved in miniaturized OECTs (in microseconds) as the response time is dependent on the film thickness.

An OECT based on PEDOT:PSS lines and NaCl solution was fabricated and characterized. The channel width and channel length are 2.51mm 0.19mm respectively. The transfer function and output function are shown in figure 5.7 (a) and (b) below:

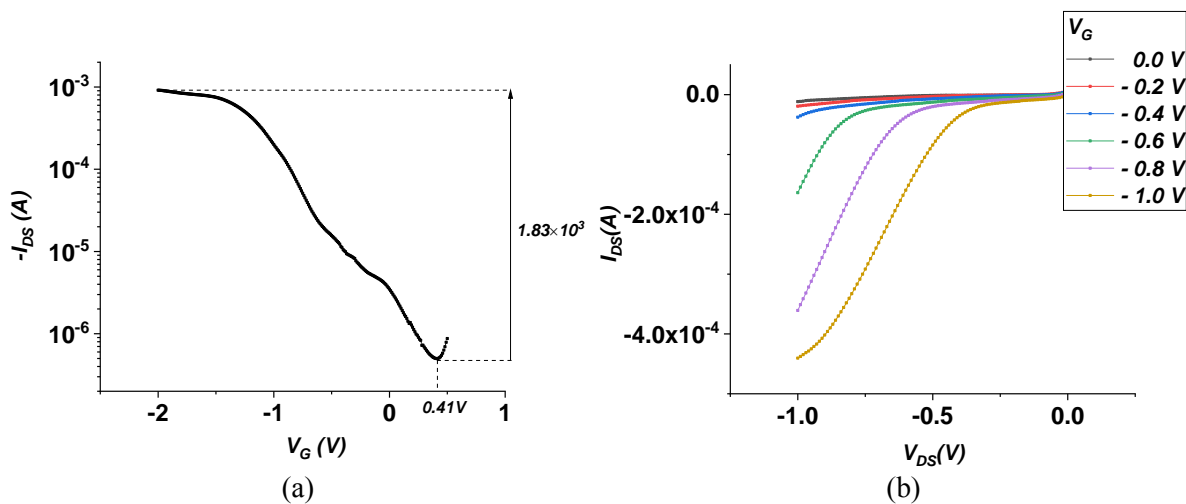


Figure 5.7 The (a) Transfer function and (b) Output function of the OECT based on the patterned PEDOT:PSS lines.

The drain-source voltage was maintained at -0.6V . It is clear that the drain current decreases as the gate voltage increases, indicating that the OEET is working in the depletion mode because Na^+ from electrolyte de-dopes the negatively charged PSS, increasing the resistivity of PEDOT:PSS. It is evident that the turn on voltage is about 0.4V and the current on/off ratio can reach more than 10^3 at -2V , indicating a huge transconductance.

5.4 Sub-Micron OEETs

OEETs with nanoscale channel length and channel width are promising for integrated bio-applications. Moreover, nanoscale OEETs can provide a faster response speed. Mould-guided drying technique provides the potential opportunity for nanostructured OEETs because the dimension can be scaled down by diluting solutions.

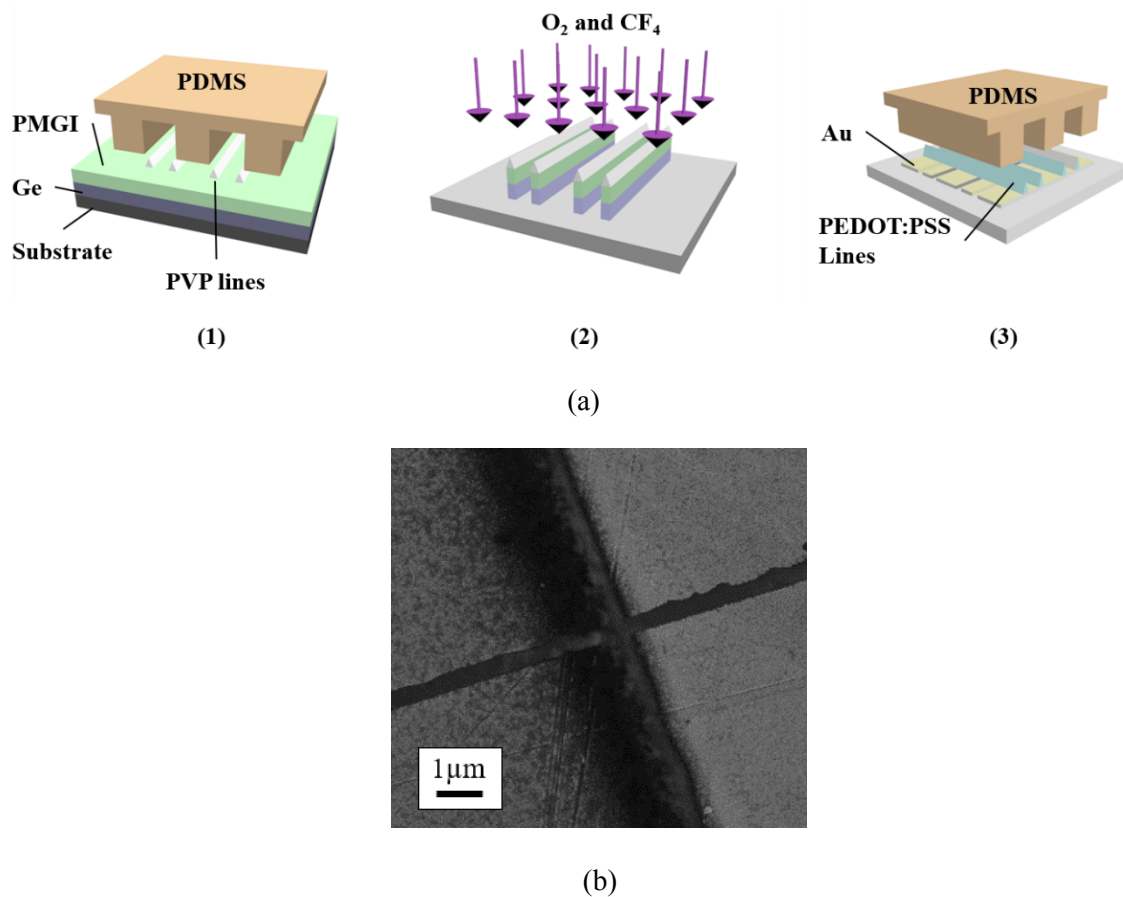


Figure 5.8 (a) The fabrication process of nanostructured OEETs. (b) The nanoscale channel width and channel length by SEM.

The nanostructured OEETs were fabricated by firstly fabricating electrodes with small gaps using a similar process. Silicon with a $300\ \text{nm}$ -thick SiO_2 layer was used as the substrate. A 250nm -thick polydimethylglutarimide (PMGI) layer was spin-coated on the substrate and

baked for 30 min at 200°C, and then a 10nm-thick Ge layer was deposited by thermal evaporation. Poly-4-vinylphenol (PVP) lines were formed on the Ge layer using the same method, as is shown in figure 5.8 (a.1). CF₄ plasma was used to etch through the Ge layer with the patterned PVP lines as an etching mask and this was followed by oxygen plasma to etch through the PMGI using the thin Ge layer as an etching mask (figure 5.8 a.2). Then, Au/Cr (30nm/10nm) films were deposited by thermal evaporation and a lift-off was accomplished in a Microposit Remover (1165) at 60°C. Eventually, PEDOT:PSS lines were created on top of the fabricated Au electrodes and annealed at 140°C for 1 hour in air, as shown in figure 5.8 (a.3).

An OECT was then fabricated by adding 0.1 M NaCl aqueous solution as electrolyte and a silver probe as the gate electrode. A plastic ring was placed above the sample to restrict the electrolyte, and the whole structure of the OECT is identical to the one shown in figure 5.6 in the previous section. Figure 5.8 (b) shows the SEM image of the nanoscale channel length and channel width.

5.4.1 Transistor characteristics

The electrical characteristics of the nanostructured OECT were carried out. The transfer function and output function are shown below in figure 5.9.

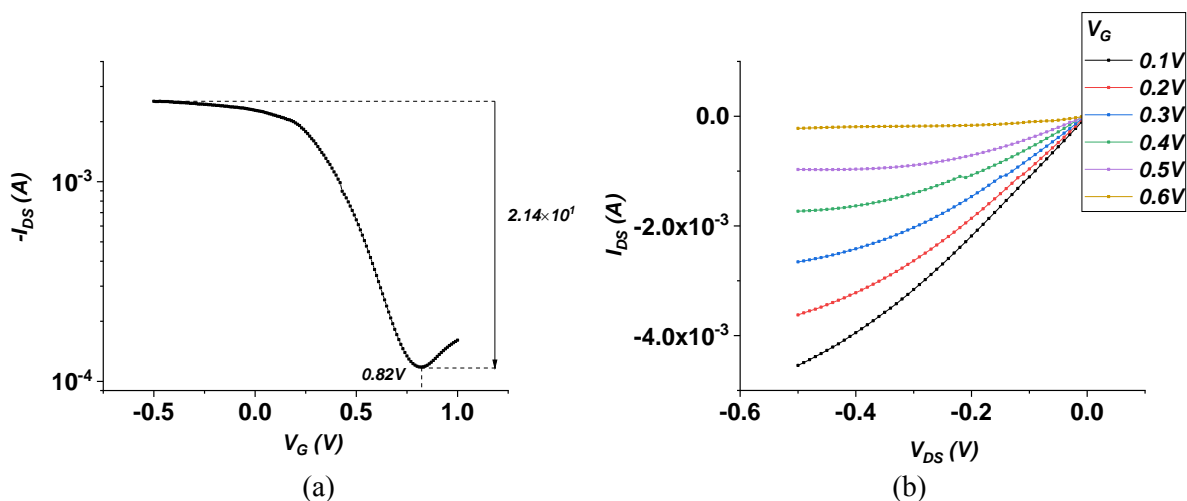


Figure 5.9 The (a) Transfer function and (b) Output function of the nanostructured OECT.

The drain-source voltage was maintained at -0.3V. It is evident that the on/off current ratio is about 21.4 when the device is operated within $\pm 1V$ and the turn-on voltage is 0.82V. The nanostructured OECT device has a good amplifying behavior which is crucial for high-resolution sensing, like bio-recording, where the ion concentration varies within the subcellular domain. Due to the short channel, the high current density was also achieved.

5.4.2 Frequency response

The frequency response of the fabricated PEDOT:PSS wire transistors was also investigated. The frequency response was measured with an oscilloscope on a voltage drop between a resistor connected in series in the drain current loop. Figure 5.10 below shows the frequency response of different input signals. The left and right column indicate the simulated input signal and actual output signal respectively. The device exhibited a good frequency response. Multiple input frequency responses were measured, which widely exist in the signal process of the neuron system and can potentially be applied for logical performance. The multiple inputs were realized by using multiple gates, each powered by a signal generator. Figure 5.10 (a) is the response of square inputs with 1KHz. Figure 5.10 (b)~(d) show the multiple input responses of the transistor (on the right) and the modelled input (on the left). The resulting output spectra are well described by a summation of input signals and can be conveniently decomposed with high accuracy. In addition, a tiny phase change (of less than 0.01π) of the inputs can be responded in the output spectra, as is shown in figure 5.10 (e).

It is evident that the nanostructured OECT has a good frequency response and it is capable of high-frequency applications. In addition, it is also responsive to small phase signals.

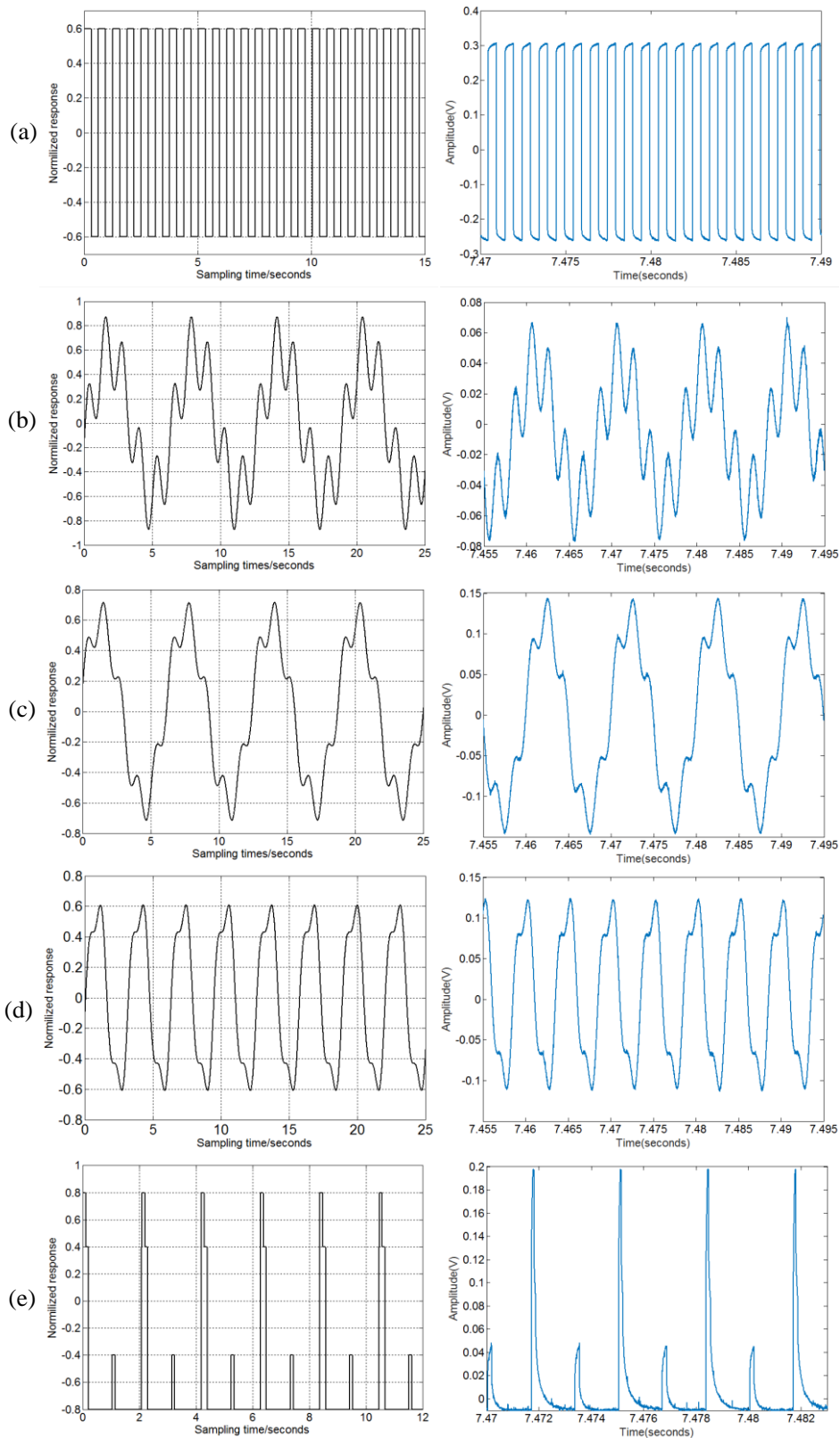


Figure 5.10 The frequency response of (a) Single square signal, $f=1\text{kHz}$. (b) Two sine signals, $f_1=500\text{Hz}$ (600mv), $f_2=100\text{Hz}$ (300mv). (c) Two sine signals, $f_1=500\text{Hz}$ (600mv), $f_2=100\text{Hz}$ (200mv). (d) Two sine signals, $f_1=500\text{Hz}$ (600mv), $f_2=100\text{Hz}$ (100mv). (e) A small phase change ($<0.01 \pi$)

5.4.3. Effect of electrode area

The electrical performance of the OECT is influenced by the area of electrode. The electrical conduction is composed by two paths: PEDOT:PSS and NaCl ions. The conduction of PEDOT:PSS is dependent on the number of PEDOT:PSS lines. The ionic conduction of NaCl is heavily affected by the electrode area (exposed to NaCl solutions) and NaCl concentration. A set of samples with the same number of lines and different electrode area were prepared, and the electrical characteristics was compared. The results are shown in figure 5.11 below.

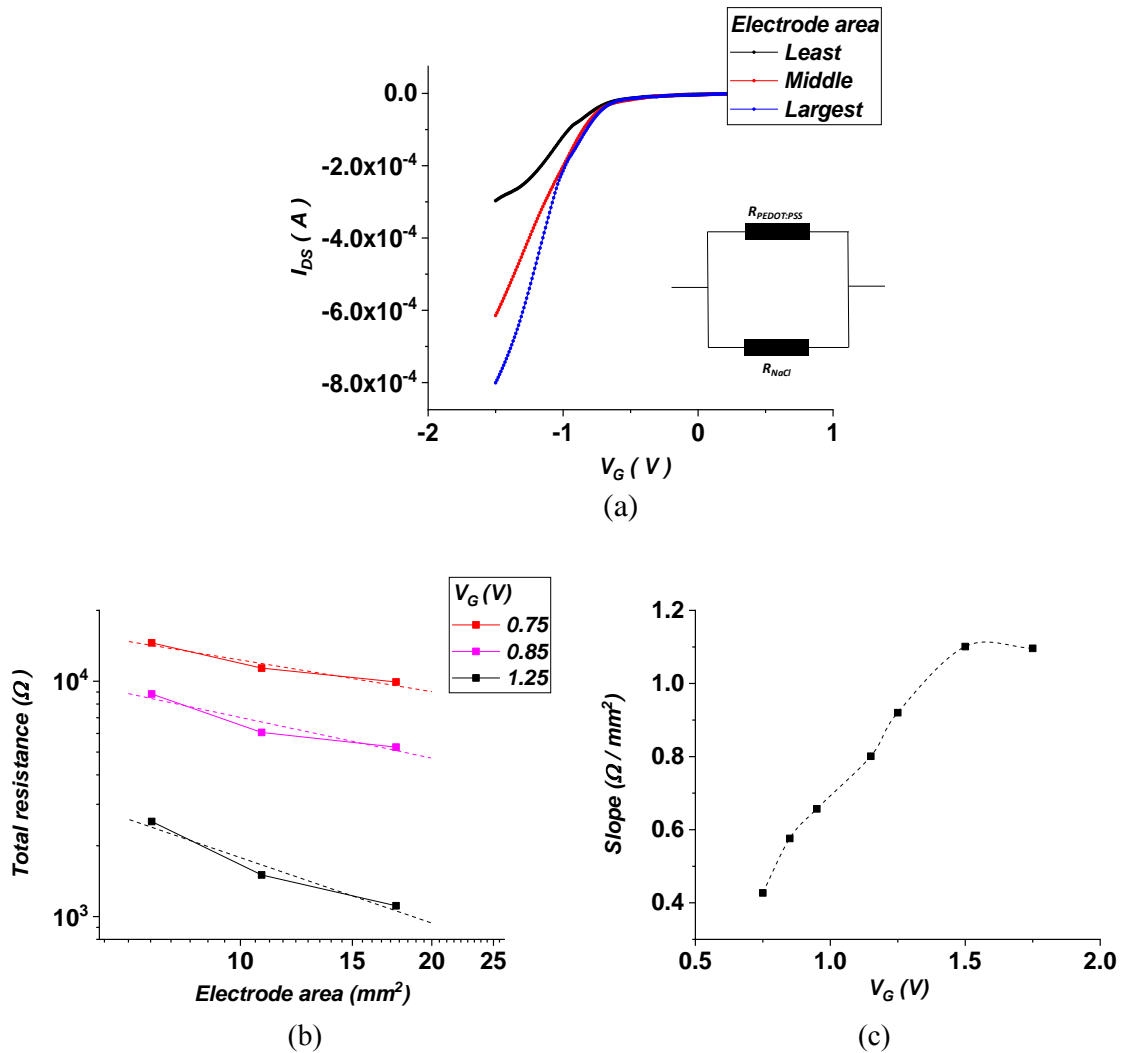


Figure 5.11 (a) The transfer function of OECT with different electrode area. (b) and (c) The influence of electrode area and gate voltages.

Figure 5.11 (a) evidently shows that larger electrode area results in larger drain-source current (I_{DS}). This is because larger exposed electrode area leads to a smaller resistance due to ionic conduction. Accordingly, the I_{DS} increases as area increases. In addition, it is also found that larger electrode area leads to a larger current on/off ratio (I_{on}/I_{off}).

The total resistance at different gate voltages is plotted in figure 5.11 (b). It is shown that the total resistance decreases as the electrode area increases. This is mainly due to the decrease in ionic resistance (R_{NaCl}). In addition, the slope of total resistance against electrode area increases as the gate voltages increases. The relation between the slope in figure 5.11 (b) versus gate voltage is further plotted in figure 5.11 (c), which indicates that higher gate voltage is enhancing the sensitivity of total resistance to the change of electrode area.

Chapter 6 Conclusions and Future Work

6.1 Conclusions

Solution-processed ZnO NPs were thoroughly investigated in terms of the physical properties, post-processing effects and patterning techniques. In addition, applications of ZnO NPs such as optically addressed spatial light modulator (OASLM) and oxygen partial pressure sensor were characterized. Moreover, the patterning technique was also applied to water-based PEDOT:PSS to fabricate nanoscale organic electrochemical transistor (OECT). This thesis has recorded and demonstrated the promising future of solution-processable materials since they possess many advantages such as low requirement for fabrication conditions, economic cost, large scale and possibility for high-resolution patterning etc.

- Chapter 1 was a general review of related topics such as the fundamentals of ZnO and ZnO NPs, fabrication methods for solution-processable materials, fundamentals of ZnO NPs-based OASLM and oxygen partial pressure sensor. OASLM combines the UV sensitivity of ZnO NPs and electrical modulation of liquid crystals (LCs). Oxygen partial pressure sensor utilizes the oxygen adsorption and desorption of ZnO NPs.
- Chapter 2 systematically characterized the physical properties of ZnO NPs such as particle size, electrical conduction, dielectric response and optical response etc. The effect of measuring ambient, annealing temperature and oxygen plasma were also investigated. It was found that the electrical conductivity of ZnO NPs was strongly affected by the oxygen content in the measuring ambient. The conductivity of ZnO NPs could also be changed by oxygen plasma treatment. Moreover, the annealing temperature had a huge influence on trap activation energy and RC time constant.
- Chapter 3 mainly focused on the characterization and optimization of ZnO NP-based OASLMs. Simulations were conducted to illustrate the resolution limit coming from LCs and ZnO NPs in OASLMs. OASLMs were then characterized in terms of dielectric properties and optical responses, from which the best operating voltage was determined in order to have the shortest RC time constant. Then the diffraction efficiency and response time were optimized. The diffraction efficiency was improved by determining the best driving signals (waveform, amplitude and frequency). In order to improve the response time, higher annealing temperature for ZnO NPs was used. In addition, the

introduction of a SiO₂ interface layer and a heterojunction were proved to effectively reduce the fall time of OASLM.

- Chapter 4 summarized ZnO NPs-based oxygen partial pressure sensor. The fabrication and performance of the sensor were discussed. The nano-patterning of ZnO NPs was also achieved by mould-guided drying technique. Moreover, oxygen partial pressure sensor was fabricated based on the patterned ZnO NPs. This is meaningful because this is promising for integrated and miniaturized applications.
- Chapter 5 was focused on another solution-processed material: PEDOT:PSS. The electrical characterization was performed, and it was patterned with the same technique as ZnO NPs. The patterned PEDOT:PSS lines were characterized in terms of electrical and optical anisotropy. Organic electrochemical transistor (OECT) was fabricated with the patterned PEDOT:PSS. Furthermore, OECT with nanoscale channel length and channel width was successfully fabricated. This is particularly interesting since this is a good method to fabricate low-power synaptic transistor, which is a step closer to build the real neural system.

To summarize, solution-processed ZnO NPs were systematically researched in this work regarding their characterization, post processing, patterning, application and optimization etc. In particular, ZnO NPs-based OASLM and oxygen partial pressure sensor were investigated in terms of working principles, device characterization and performance optimization etc. In the meanwhile, solution-based PEDOT:PSS was also studied and its application in OECT was investigated in detail. This work also demonstrated that mould-guided drying technique is a promising method for nano-patterning and large-scale fabrication.

6.2 Future Work

This work has demonstrated the promising future of solution-based ZnO NPs and PEDOT:PSS as inorganic semiconductor and organic conductor. It also opens the door for more research opportunities that are interesting and meaningful.

- ZnO NPs are unique for their large surface-to-volume ratio, which implies that the defects at the surface could be dominant. The defect at the interface could result from the dangling bonds, mismatched lattice and recombined bonds etc. The surface states could be influential to macroscopic properties of ZnO NPs such as low-temperature electrical conductivity, metal-like conductivity, higher recombination rate etc. The

enhanced electrical conductivity at low temperatures (<120K) has been observed in this work (discussed in chapter 2) and this can be further studied along with other techniques. The surface states are most likely deep-level states since they are related to the defects, and the deep-level states can be investigated by deep level transient spectroscopy (DLTS) and photoluminescence (PL). UV-vis spectroscopy is also a possible technique and it has already been found in this work that there are two absorbance peaks at around 300nm and 360nm. The peak at 300nm was not clearly understood and this might be associated with the defect states.

- The electrical properties of PEDOT:PSS thin films are of great significance to the understanding of electronic behavior. The electrical conduction mechanism has been discussed at low voltages whereas the high-voltage conduction mechanism has not been fully understood yet. In particular, the power index α which determines the relationship between $\log(\sigma) \sim 1/T$ is yet to be determined. The dielectric behavior of PEDOT:PSS is also a valuable research topic. The impedance spectroscopy of PEDOT:PSS thin film has been carried out in this work and preliminary analysis showed that there are multiple polarization mechanisms. The investigation of polarization mechanisms is significant to the understanding of structural characteristics and electronic transport in the PEDOT:PSS polymers.
- The pseudo-inductive behavior in the impedance spectroscopy of the heterojunction between PEDOT:PSS and ZnO NPs was observed and it was also noticed that it is dependent on the bias voltage. This behavior was attributed by some researchers to the ionic transportation and redox reactions at the interface. Further research could be carried out to pinpoint the ions species and other materials associated in the chemical reactions. This is meaningful because it helps to understand the behavior of PEDOT:PSS in air and this could be further used for sensing applications.
- The mould-guided drying technique has been proved to be promising to pattern nanoscale ZnO NPs and PEDOT:PSS features. It was also demonstrated that large-area PEDOT:PSS grid is achievable using mould-guided drying technique. And the results showed that two crossed lines are in a good contact. This could be further extended by patterning two types of solution-based semiconductor materials (p-type and n-type) with orthogonal direction, forming a grid composed by PN diodes as LEDs. This is attractive because it offers a low-cost and high-yielding method to fabricate LEDs.

References

- [1] A. Armin and P. Meredith, "Solution-processed semiconductors for next-generation photodetectors," 2017.
- [2] S. J. Kim, S. Yoon, and H. J. Kim, "Review of solution-processed oxide thin-film transistors."
- [3] P. K. Shrestha, Y. T. Chun, and D. Chu, "A high-resolution optically addressed spatial light modulator based on ZnO nanoparticles," *Light Sci. Appl.*, vol. 4, no. 3, pp. e259–e259, 2015.
- [4] W. Cao and H. Chen, "Transparent electrodes for organic optoelectronic devices : a review," 2019.
- [5] D. Mccoul, W. Hu, M. Gao, V. Mehta, and Q. Pei, "Recent Advances in Stretchable and Transparent Electronic Materials," pp. 1–51, 2016.
- [6] A. Janotti and C. G. Van De Walle, "Fundamentals of zinc oxide as a semiconductor," vol. 72, 2009.
- [7] Y. Jin, J. Wang, B. Sun, J. C. Blakesley, and N. C. Greenham, "Solution-processed ultraviolet photodetectors based on colloidal ZnO nanoparticles," *Nano Lett.*, vol. 8, no. 6, pp. 1649–1653, 2008.
- [8] Ü. Ozgur, D. Hofstetter, and H. Morkoç, "ZnO devices and applications: A review of current status and future prospects," *Proc. IEEE*, vol. 98, no. 7, pp. 1255–1268, 2010.
- [9] J. Huang, Z. Yin, and Q. Zheng, "Applications of ZnO in organic and hybrid solar cells," *Energy Environ. Sci.*, vol. 4, no. 10, pp. 3861–3877, 2011.
- [10] I. V. Tudose and M. Sucheai, "ZnO for photocatalytic air purification applications," *IOP Conf. Ser. Mater. Sci. Eng.*, vol. 133, no. 1, 2016.
- [11] H. Yan, R. He, J. Johnson, M. Law, R. J. Saykally, and P. Yang, "Dendritic nanowire ultraviolet laser array," *J. Am. Chem. Soc.*, vol. 125, no. 16, pp. 4728–4729, 2003.
- [12] A. Kolodziejczak-Radzimska and T. Jesionowski, "Zinc oxide-from synthesis to application: A review," *Materials (Basel)*, vol. 7, no. 4, pp. 2833–2881, 2014.
- [13] A. Sirelkhatim *et al.*, "Review on zinc oxide nanoparticles: Antibacterial activity and toxicity mechanism," *Nano-Micro Lett.*, vol. 7, no. 3, pp. 219–242, 2015.
- [14] H. Ma, P. L. Williams, and S. A. Diamond, "Ecotoxicity of manufactured ZnO nanoparticles - A review," *Environ. Pollut.*, vol. 172, pp. 76–85, 2013.
- [15] L. E. Shi, Z. H. Li, W. Zheng, Y. F. Zhao, Y. F. Jin, and Z. X. Tang, "Synthesis, antibacterial

- activity, antibacterial mechanism and food applications of ZnO nanoparticles: A review,” *Food Addit. Contam. - Part A Chem. Anal. Control. Expo. Risk Assess.*, vol. 31, no. 2, pp. 173–186, 2014.
- [16] T. J. W. Gabriel Colon, Brian C. Ward, “Increased osteoblast and decreased Staphylococcus epidermidis functions on nanophase ZnO and TiO₂,” *J Biomed Mater Res A.*, vol. 67, no. 8, pp. 1180–1185, 2017.
- [17] Ü. Özgür *et al.*, “A comprehensive review of ZnO materials and devices,” *J. Appl. Phys.*, vol. 98, no. 4, pp. 1–103, 2005.
- [18] Ü. Morkoc, H.; Özgür, *Zinc Oxide Fundamentals, Materials and Device Technology*. WILEY-VCH Verlag GmbH & Co. KGaA, Weinheim, 2009.
- [19] D. C. Look *et al.*, “Electrical properties of bulk ZnO,” *Solid State Commun.*, vol. 105, no. 6, pp. 399–401, 1998.
- [20] E. M. Kaidashev *et al.*, “High electron mobility of epitaxial ZnO thin films on c-plane sapphire grown by multistep pulsed-laser deposition,” *Appl. Phys. Lett.*, vol. 82, no. 22, pp. 3901–3903, 2003.
- [21] K. Iwata *et al.*, “Improvement of electrical properties in ZnO thin films grown by radical source(RS)-MBE,” *Phys. Status Solidi Appl. Res.*, vol. 180, no. 1, pp. 287–292, 2000.
- [22] J. Wang, R. Chen, L. Xiang, and S. Komarneni, “Synthesis, properties and applications of ZnO nanomaterials with oxygen vacancies: A review,” *Ceram. Int.*, vol. 44, no. 7, pp. 7357–7377, 2018.
- [23] L. Liu *et al.*, “Oxygen vacancies: The origin of n-type conductivity in ZnO,” *Phys. Rev. B*, vol. 93, no. 23, pp. 1–6, 2016.
- [24] A. Janotti and C. G. Van De Walle, “Oxygen vacancies in ZnO,” *Appl. Phys. Lett.*, vol. 87, no. 12, pp. 1–3, 2005.
- [25] C. G. Van De Walle, “Hydrogen as a Cause of Doping in Zinc Oxide,” vol. 85, no. 1, pp. 0–3, 2000.
- [26] C. Zhang, X. Geng, H. Liao, C. J. Li, and M. Debliquy, “Room-temperature nitrogen-dioxide sensors based on ZnO_{1-x} coatings deposited by solution precursor plasma spray,” *Sensors Actuators, B Chem.*, vol. 242, pp. 102–111, 2017.
- [27] N. Han, X. Wu, L. Chai, H. Liu, and Y. Chen, “Counterintuitive sensing mechanism of ZnO nanoparticle based gas sensors,” *Sensors Actuators, B Chem.*, vol. 150, no. 1, pp. 230–238, 2010.
- [28] P. Camarda *et al.*, “Luminescence mechanisms of defective ZnO nanoparticles,” *Phys. Chem.*

Chem. Phys., vol. 18, no. 24, pp. 16237–16244, 2016.

- [29] A. You, M. A. Y. Be, and I. In, “Correlation between photoluminescence and oxygen vacancies in ZnO phosphors,” vol. 403, no. 1, pp. 10–13, 2019.
- [30] A. B. Djurišić and Y. H. Leung, “Optical properties of ZnO nanostructures,” *Small*, vol. 2, no. 8–9, pp. 944–961, 2006.
- [31] Y. Gong, T. Andelman, G. F. Neumark, S. O’Brien, and I. L. Kuskovsky, “Origin of defect-related green emission from ZnO nanoparticles: Effect of surface modification,” *Nanoscale Res. Lett.*, vol. 2, no. 6, pp. 297–302, 2007.
- [32] F. Tuomisto, K. Saarinen, and G. C. Farlow, “Introduction and recovery of point defects in electron-irradiated ZnO,” pp. 1–11, 2005.
- [33] A. B. Djurišić, X. Chen, Y. H. Leung, and A. Man Ching Ng, “ZnO nanostructures: Growth, properties and applications,” *J. Mater. Chem.*, vol. 22, no. 14, pp. 6526–6535, 2012.
- [34] S. Talam, S. R. Karumuri, and N. Gunnam, “Synthesis, Characterization, and Spectroscopic Properties of ZnO Nanoparticles,” *ISRN Nanotechnol.*, vol. 2012, pp. 1–6, 2012.
- [35] J. H. Jun, H. Seong, K. Cho, B. M. Moon, and S. Kim, “Ultraviolet photodetectors based on ZnO nanoparticles,” *Ceram. Int.*, vol. 35, no. 7, pp. 2797–2801, 2009.
- [36] J. Eriksson, V. Khranovskyy, F. Söderlind, P. O. Käll, R. Yakimova, and A. L. Spetz, “ZnO nanoparticles or ZnO films: A comparison of the gas sensing capabilities,” *Sensors Actuators, B Chem.*, vol. 137, no. 1, pp. 94–102, 2009.
- [37] A. Singh, “Synthesis, characterization, electrical and sensing properties of ZnO nanoparticles,” *Adv. Powder Technol.*, vol. 21, no. 6, pp. 609–613, 2010.
- [38] Michelle J. S. Spencer and Irene Yarovsky, “ZnO Nanostructures for Gas Sensing: Interaction of NO₂, NO, O, and N with the ZnO(1010) Surface,” *J. Phys. Chem.*, vol. 120, no. 2, pp. 324–332, 2016.
- [39] S. S. Kumar, P. Venkateswarlu, V. R. Rao, and G. N. Rao, “Synthesis, characterization and optical properties of zinc oxide nanoparticles,” *Int. Nano Lett.*, vol. 3, no. 1, p. 30, 2013.
- [40] G. H. Kim *et al.*, “Effect of indium composition ratio on solution-processed nanocrystalline InGaZnO thin film transistors,” *Appl. Phys. Lett.*, vol. 233501, no. 2009, pp. 10–13, 2012.
- [41] D. H. Lee, Y. J. Chang, G. S. Herman, and C. H. Chang, “A general route to printable high-mobility transparent amorphous oxide semiconductors,” *Adv. Mater.*, vol. 19, no. 6, pp. 843–847, 2007.
- [42] S. J. Kim, S. Yoon, and H. J. Kim, “Review of solution-processed oxide thin-film transistors,”

- Jpn. J. Appl. Phys.*, vol. 53, no. 2 PART 2, 2014.
- [43] N. Sahu, B. Parija, and S. Panigrahi, “Fundamental understanding and modeling of spin coating process: A review,” *Indian J. Phys.*, vol. 83, no. 4, pp. 493–502, 2009.
- [44] C. J. Brinker, A. J. Hurd, P. R. Schunk, G. C. Frye, and C. S. Ashley, “Review of sol-gel thin film formation,” *J. Non. Cryst. Solids*, vol. 147–148, no. C, pp. 424–436, 1992.
- [45] B. S. Ong, C. Li, Y. Li, Y. Wu, and R. Loutfy, “Stable, solution-processed, high-mobility ZnO thin-film transistors,” *J. Am. Chem. Soc.*, vol. 129, no. 10, pp. 2750–2751, 2007.
- [46] C. S. Li, Y. N. Li, Y. L. Wu, B. S. Ong, and R. O. Loutfy, “Fabrication conditions for solution-processed high-mobility ZnO thin-film transistors,” *J. Mater. Chem.*, vol. 19, no. 11, pp. 1626–1634, 2009.
- [47] H. S. Lim, Y. S. Rim, and H. J. Kim, “Photoresist-free fully self-patterned transparent amorphous oxide thin-film transistors obtained by sol-gel process,” *Sci. Rep.*, vol. 4, pp. 1–6, 2014.
- [48] S. Sanctis, R. C. Hoffmann, M. Bruns, and J. J. Schneider, “Direct Photopatterning of Solution-Processed Amorphous Indium Zinc Oxide and Zinc Tin Oxide Semiconductors—A Chimie Douce Molecular Precursor Approach to Thin Film Electronic Oxides,” *Adv. Mater. Interfaces*, vol. 5, no. 15, p. 1800324, 2018.
- [49] R. A. Street *et al.*, “Sol-gel solution-deposited InGaZnO thin film transistors,” *ACS Appl. Mater. Interfaces*, vol. 6, no. 6, pp. 4428–4437, 2014.
- [50] C. Chen *et al.*, “Solution-processed metal oxide arrays using femtosecond laser ablation and annealing for thin-film transistors,” *J. Mater. Chem. C*, vol. 5, no. 36, pp. 9273–9280, 2017.
- [51] Y. Choi, G. H. Kim, W. H. Jeong, H. J. Kim, B. D. Chin, and J. W. Yu, “Characteristics of gravure printed InGaZnO thin films as an active channel layer in thin film transistors,” *Thin Solid Films*, vol. 518, no. 22, pp. 6249–6252, 2010.
- [52] S. Wu, Q. Zhang, Z. Chen, L. Mo, S. Shao, and Z. Cui, “Inkjet printing of oxide thin film transistor arrays with small spacing with polymer-doped metal nitrate aqueous ink,” *J. Mater. Chem. C*, vol. 5, no. 30, pp. 7495–7503, 2017.
- [53] W. J. Scheideler, R. Kumar, A. R. Zeumault, and V. Subramanian, “Low-Temperature-Processed Printed Metal Oxide Transistors Based on Pure Aqueous Inks,” *Adv. Funct. Mater.*, vol. 27, no. 14, 2017.
- [54] S. Li *et al.*, “High-resolution patterning of solution-processable materials via externally engineered pinning of capillary bridges,” *Nat. Commun.*, vol. 9, no. 1, 2018.
- [55] A. M. Weiner, “Femtosecond pulse shaping using spatial light modulators,” *Rev. Sci. Instrum.*,

vol. 71, no. 5, pp. 1929–1960, 2000.

- [56] J. Hahn, H. Kim, Y. Lim, G. Park, and B. Lee, “Wide viewing angle dynamic holographic stereogram with a curved array of spatial light modulators,” *Opt. Express*, vol. 16, no. 16, p. 12372, 2008.
- [57] J. M. Tschopp and P. Astoul, “Dynamic holographic optical tweezers,” *Opt. Commun.*, vol. 207, no. June, pp. 141–143, 2014.
- [58] Z. Kuang *et al.*, “High throughput diffractive multi-beam femtosecond laser processing using a spatial light modulator,” *Appl. Surf. Sci.*, vol. 255, no. 5 PART 1, pp. 2284–2289, 2008.
- [59] Y. Pan, J. Liu, X. Li, and Y. Wang, “A Review of Dynamic Holographic Three-Dimensional Display: Algorithms, Devices, and Systems,” *IEEE Trans. Ind. Informatics*, vol. 12, no. 4, pp. 1599–1610, 2016.
- [60] S. Reichelt *et al.*, “Full-range, complex spatial light modulator for real-time holography,” *Opt. Lett.*, vol. 37, no. 11, p. 1955, 2012.
- [61] B. Robertson *et al.*, “Demonstration of multi-casting in a 1×9 LCOS wavelength selective switch,” *J. Light. Technol.*, vol. 32, no. 3, pp. 402–410, 2014.
- [62] X. Zeng, J. Bai, C. Hou, and G. Yang, “Compact optical correlator based on one phase-only spatial light modulator,” *Opt. Lett.*, vol. 36, no. 8, p. 1383, 2011.
- [63] Z. Y. and D. C. Zichen Zhang, “Fundamentals of phase-only liquid crystal on silicon (LCOS) devices,” *Light Sci. Appl.*, vol. 3, no. 10, pp. 1–10, 2014.
- [64] J. P. F. Lagerwall and G. Scalia, “A new era for liquid crystal research: Applications of liquid crystals in soft matter nano-, bio- and microtechnology,” *Curr. Appl. Phys.*, vol. 12, no. 6, pp. 1387–1412, 2012.
- [65] D. Andrienko, “Introduction to liquid crystals,” *J. Mol. Liq.*, vol. 267, pp. 520–541, 2018.
- [66] H. Iino, T. Usui, and J. I. Hanna, “Liquid crystals for organic thin-film transistors,” *Nat. Commun.*, vol. 6, pp. 1–8, 2015.
- [67] Y. Wan and D. Zhao, “On the controllable soft-templating approach to mesoporous silicates,” *Chem. Rev.*, vol. 107, no. 7, pp. 2821–2860, 2007.
- [68] H. Jiang, C. Li, and X. Huang, “Actuators based on liquid crystalline elastomer materials,” *Nanoscale*, vol. 5, no. 12, pp. 5225–5240, 2013.
- [69] F. Salinas, E. Barros, W. Eisenberg, D. Smith, and S. Viswanathan, “Impact of Nanotechnology on Drug Delivery,” *Nanotechnol. Telecommun.*, vol. 3, no. 1, pp. 23–41, 2010.

- [70] I. Khoo, *Liquid Crystals*, vol. 9, no. 2, 2007.
- [71] L. Wang and G. Moddel, "Resolution limits from charge transport in optically addressed spatial light modulators," *J. Appl. Phys.*, vol. 6923, no. 1995, 2002.
- [72] V. F. Nazvanov and D. I. Kovalenko, "Resolution of optically addressed liquid-crystal spatial light modulators," *Tech. Phys. Lett.*, vol. 24, no. 7, pp. 520–522, 2002.
- [73] P. R. Barbier, "Thin-film photosensor design for liquid crystal spatial light modulators," *Opt. Eng.*, vol. 33, no. 4, p. 1322, 1994.
- [74] G. Moddel, W. Li, L. A. Pagano-Stauffer, R. A. Rice, and M. A. Handschy, "Hydrogenated amorphous-silicon photosensor for optically addressed high-speed spatial light modulator," *IEEE Trans. Electron Devices*, vol. 36, no. 12, pp. 2959–2964, 2002.
- [75] G. Moddel, K. M. Johnson, W. Li, R. A. Rice, L. A. Pagano-Stauffer, and M. A. Handschy, "High-speed binary optically addressed spatial light modulator," *Appl. Phys. Lett.*, vol. 55, no. 6, pp. 537–539, 1989.
- [76] S. Fukushima, T. Kurokawa, and M. Ohno, "Real-time hologram construction and reconstruction using a high-resolution spatial light modulator," *Appl. Phys. Lett.*, vol. 58, no. 8, pp. 787–789, 1991.
- [77] D. V. Wick *et al.*, "Deformed-helix ferroelectric liquid-crystal spatial light modulator that demonstrates high diffraction efficiency and 370-line pairs/mm resolution," *Appl. Opt.*, vol. 38, no. 17, p. 3798, 2008.
- [78] M. Feldman, "Liquid-crystal light valves," *Electron. Lett.*, vol. 6, no. 26, pp. 837-839(2), Dec. 1970.
- [79] P. Aubourg, J. P. Huignard, M. Hareng, and R. A. Mullen, "Liquid crystal light valve using bulk monocrystalline Bi₁₂SiO₂₀ as the photoconductive material," *Appl. Opt.*, vol. 21, no. 20, p. 3706, 2009.
- [80] N. Collings, A. R. Pourzand, F. L. Vladimirov, N. I. Pletneva, and A. N. Chaika, "Pixelated liquid-crystal light valve for neural network application," *Appl. Opt.*, vol. 38, no. 29, p. 6184, 2008.
- [81] M. G. Kirzhner, M. Klebanov, V. Lyubin, N. Collings, and I. Abdulhalim, "Liquid crystal high-resolution optically addressed spatial light modulator using a nanodimensional chalcogenide photosensor," *Opt. Lett.*, vol. 39, no. 7, p. 2048, 2014.
- [82] T. Safrani *et al.*, "Chemically deposited PbS thin film photo-conducting layers for optically addressed spatial light modulators," *J. Mater. Chem. C*, vol. 2, no. 43, pp. 9132–9140, 2014.
- [83] F. Yao, Y. Pei, Y. Zhang, J. Zhang, C. Hou, and X. Sun, "High-resolution photorefractive

gratings in nematic liquid crystals sandwiched with photoconductive polymer film,” *Appl. Phys. B Lasers Opt.*, vol. 92, no. 4, pp. 573–576, 2008.

- [84] J. P. T. Ward, “Oxygen sensors in context,” *Biochim. Biophys. Acta - Bioenerg.*, vol. 1777, no. 1, pp. 1–14, 2008.
- [85] R. Ramamoorthy, P. K. Dutta, and S. A. Akbar, “Oxygen sensors : Materials , methods , designs,” vol. 8, pp. 4271–4282, 2003.
- [86] M. Science, “Solid state gas sensors,” 1997.
- [87] R. Ramamoorthy, P. K. Dutta, and S. A. Akbar, “Oxygen sensors : Materials , methods , designs,” *J. Mater. Sci.*, vol. 38, no. 21, pp. 4271–4282, 2003.
- [88] H. J. Beie and A. Gnörich, “Oxygen gas sensors based on CeO₂ thick and thin films,” *Sensors Actuators B. Chem.*, vol. 4, no. 3–4, pp. 393–399, 1991.
- [89] D. Rosenfeld, P. E. Schmid, V. Demarne, and A. Grisel, “Electrical transport properties of thin-film metal-oxide-metal Nb₂O₅ oxygen sensors,” vol. 37, no. 1996, pp. 83–89, 2000.
- [90] Y. Hu, O. K. Tan, W. Cao, and W. Zhu, “A low temperature nano-structured SrTiO₃ thick film oxygen gas sensor,” *Ceram. Int.*, vol. 30, no. 7, pp. 1819–1822, 2004.
- [91] U. Kirner *et al.*, “Low and high temperature TiO₂ oxygen sensors,” *Sensors Actuators B. Chem.*, vol. 1, no. 1–6, pp. 103–107, 1990.
- [92] F. Chaabouni, M. Abaab, and B. Rezig, “Metrological characteristics of ZNO oxygen sensor at room temperature,” *Sensors Actuators, B Chem.*, vol. 100, no. 1–2, pp. 200–204, 2004.
- [93] A. J. Gimenez, G. Luna-Barcenas, I. C. Sanchez, and J. M. Yanez-Limon, “Paper-based ZnO oxygen sensor,” *IEEE Sens. J.*, vol. 15, no. 2, pp. 1246–1251, 2015.
- [94] S. J. Gentry and T. A. Jones, “The role of catalysis in solid-state gas sensors,” *Sensors and Actuators*, vol. 10, no. 1–2, pp. 141–163, 1986.
- [95] H. Albaris and G. Karuppasamy, “CuO–ZnO p–n junction enhanced oxygen sensing property of polypyrrole nanocomposite at room temperature,” *J. Mater. Sci. Mater. Electron.*, no. 0123456789, 2019.
- [96] Y. Z. Li and X. M. Li, “Oxygen plasma treated epitaxial ZnO thin films for Oxygen plasma treated epitaxial ZnO thin films for Schottky ultraviolet detection,” 2007.
- [97] P. Bindu and S. Thomas, “Estimation of lattice strain in ZnO nanoparticles: X-ray peak profile analysis,” *J. Theor. Appl. Phys.*, vol. 8, no. 4, pp. 123–134, 2014.
- [98] R. Yogamalar, R. Srinivasan, A. Vinu, K. Ariga, and A. C. Bose, “X-ray peak broadening analysis in ZnO nanoparticles,” *Solid State Commun.*, vol. 149, no. 43–44, pp. 1919–1923,

2009.

- [99] F.-C. Chiu, "A Review on Conduction Mechanisms in Dielectric Films," *Adv. Mater. Sci. Eng.*, vol. 2014, pp. 1–18, 2014.
- [100] A. S. Lanje, S. J. Sharma, R. S. Ningthoujam, J. S. Ahn, and R. B. Pode, "Low temperature dielectric studies of zinc oxide (ZnO) nanoparticles prepared by precipitation method," *Adv. Powder Technol.*, vol. 24, no. 1, pp. 331–335, 2013.
- [101] B. D. Viezbicke, S. Patel, B. E. Davis, and D. P. Birnie, "Evaluation of the Tauc method for optical absorption edge determination: ZnO thin films as a model system," *Phys. Status Solidi Basic Res.*, vol. 252, no. 8, pp. 1700–1710, 2015.
- [102] K. Yadav, Y. Dwivedi, and N. Jaggi, "Effect of annealing temperature on the structural and optical properties of ZnSe nanoparticles," *J. Mater. Sci. Mater. Electron.*, vol. 26, no. 4, pp. 2198–2204, 2015.
- [103] N. Verma, S. Bhatia, and R. K. Bedi, "Effect of Annealing Temperature on ZnO Nanoparticles and its Applications for Photocatalytic Degradation of DR- 31 dye," *Int. J. Pure Appl. Phys.*, vol. 13, no. 1, pp. 118–122, 2017.
- [104] M. Goswami, N. C. Adhikary, and S. Bhattacharjee, "Effect of annealing temperatures on the structural and optical properties of zinc oxide nanoparticles prepared by chemical precipitation method," *Optik (Stuttg.)*, vol. 158, pp. 1006–1015, 2018.
- [105] A. K. Zak, M. E. Abrishami, W. H. A. Majid, R. Yousefi, and S. M. Hosseini, "Effects of annealing temperature on some structural and optical properties of ZnO nanoparticles prepared by a modified sol-gel combustion method," *Ceram. Int.*, vol. 37, no. 1, pp. 393–398, 2011.
- [106] R. N. Aljawfi, M. J. Alam, F. Rahman, S. Ahmad, A. Shahee, and S. Kumar, "Impact of annealing on the structural and optical properties of ZnO nanoparticles and tracing the formation of clusters via DFT calculation," *Arab. J. Chem.*, 2018.
- [107] T. M. Hammad, J. K. Salem, and R. G. Harrison, "The influence of annealing temperature on the structure, morphologies and optical properties of ZnO nanoparticles," *Superlattices Microstruct.*, vol. 47, no. 2, pp. 335–340, 2010.
- [108] P. K. Shrestha, Y. T. Chun, and D. Chu, "ORIGINAL ARTICLE A high-resolution optically addressed spatial light modulator based on ZnO nanoparticles," no. October 2014, pp. 1–7, 2015.
- [109] K. Sun *et al.*, "Review on application of PEDOTs and PEDOT:PSS in energy conversion and storage devices," *J. Mater. Sci. Mater. Electron.*, vol. 26, no. 7, pp. 4438–4462, 2015.
- [110] Y. Wen and J. Xu, "Scientific Importance of Water-Processable PEDOT–PSS and Preparation,

Challenge and New Application in Sensors of Its Film Electrode: A Review,” *J. Polym. Sci. Part A Polym. Chem.*, vol. 55, no. 7, pp. 1121–1150, 2017.

- [111] W. Sugimoto, K. Aoyama, T. Kawaguchi, and Y. Murakami, “Kinetics of CH₃OH oxidation on PtRu / C studied by impedance and CO stripping voltammetry,” vol. 576, pp. 215–221, 2005.
- [112] S. K. Roy, M. E. Orazem, B. Tribollet, U. P. R. Cnrs, L. Interfaces, and U. Pierre, “Interpretation of Low-Frequency Inductive Loops in PEM Fuel Cells,” pp. 1378–1388, 2007.
- [113] J. Bisquert and H. Randriamahazaka, “Inductive behaviour by charge-transfer and relaxation in solid-state electrochemistry,” 2005.
- [114] N. Wagner and E. Gülzow, “Change of electrochemical impedance spectra (EIS) with time during CO-poisoning of the Pt-anode in a membrane fuel cell,” vol. 127, pp. 341–347, 2004.
- [115] F. C. Krebs, S. A. Gevorgyan, and J. Alstrup, “A roll-to-roll process to flexible polymer solar cells : model studies , manufacture and operational stability studies,” pp. 5442–5451, 2009.
- [116] T. Mustonen, K. Kordás, S. Saukko, G. Tóth, and J. S. Penttilä, “Inkjet printing of transparent and conductive patterns of single-walled carbon nanotubes and PEDOT-PSS composites,” vol. 4340, no. 11, pp. 4336–4340, 2007.
- [117] S. L. Johnson, H. K. Park, and R. F. H. Jr, “Properties of conductive polymer films deposited by infrared laser ablation,” vol. 253, pp. 6430–6434, 2007.
- [118] B. Charlot, G. Sassine, A. Garraud, B. Sorli, A. Giani, and P. Combette, “Micropatterning PEDOT:PSS layers,” *Microsyst. Technol.*, vol. 19, no. 6, pp. 895–903, 2013.
- [119] Y. Van De Burgt *et al.*, “A non-volatile organic electrochemical device as a low-voltage artificial synapse for neuromorphic computing,” vol. 16, no. April, 2017.
- [120] A. M. Nardes *et al.*, “Microscopic understanding of the anisotropic conductivity of PEDOT:PSS thin films,” *Adv. Mater.*, vol. 19, no. 9, pp. 1196–1200, 2007.
- [121] E. Vitoratos *et al.*, “Thermal degradation mechanisms of PEDOT:PSS,” *Org. Electron. physics, Mater. Appl.*, vol. 10, no. 1, pp. 61–66, 2009.
- [122] A. M. Nardes, M. Kemerink, and R. A. J. Janssen, “Anisotropic hopping conduction in spin-coated PEDOT:PSS thin films,” *Phys. Rev. B - Condens. Matter Mater. Phys.*, vol. 76, no. 8, pp. 1–7, 2007.
- [123] O. P. Dimitriev, D. A. Grinko, Y. V Noskov, N. A. Ogurtsov, and A. A. Pud, “PEDOT : PSS films — Effect of organic solvent additives and annealing on the film conductivity,” vol. 159, pp. 2237–2239, 2009.

- [124] J. Rivnay, S. Inal, A. Salleo, R. M. Owens, M. Berggren, and G. G. Malliaras, “Organic electrochemical transistors,” *Nat. Rev. Mater.*, vol. 3, 2018.